Available online at www.sciencedirect.com
ScienceDirect
Comput. Methods Appl. Mech. Engrg. 316 (2017) 1086–1156
Computer methods in applied mechanics and engineering
www.elsevier.com/locate/cma

Superconvergent patch recovery and a posteriori error estimation technique in adaptive isogeometric analysis

Mukesh Kumar*,[1], Trond Kvamsdal, Kjetil André Johannessen

Department of Mathematical Sciences, Norwegian University of Science and Technology, N-7491 Trondheim, Norway

Available online 21 November 2016

Highlights

- A posteriori error estimation methodology for adaptive isogeometric analysis using LR B-splines is developed.
- Superconvergent patch recovery of gradient field on adaptive meshes is developed.
- Algorithm for computation of true superconvergent points on non-uniform adaptive meshes is provided.
- Numerical tests verify that the developed error estimator are highly efficient and asymptotically exact.

Abstract

In this article, we address adaptive methods for isogeometric analysis based on local refinement guided by recovery based a posteriori error estimates.

Isogeometric analysis was introduced a decade ago and an impressive progress has been made related to many aspects of numerical methods and advanced applications. However, related to adaptive mesh refinement guided by a posteriori error estimators, rather few attempts are pursued besides the use of classical residual based error estimators. In this article, we explore a feature common for Isogeometric analysis (IGA), namely the use of structured tensorial meshes that facilitates superconvergence behavior of the gradient in the Galerkin discretization. By utilizing the concept of structured mesh refinement using LR B-splines, our aim is to facilitate superconvergence behavior for locally refined meshes as well. Superconvergence behavior matches well with the use of recovery based a posteriori estimator in the Superconvergent Patch Recovery (SPR) procedure. However, to our knowledge so far, the SPR procedure has not been exploited in the IGA community.

We start out by addressing the existence of derivative superconvergent points in the computed finite element solution based on B-splines and LR B-splines for an elliptic model problem (1D and 2D Poisson). Then, we present some recovery procedures for improving the derivatives (or gradient) of the isogeometric finite element solution where the SPR procedure will be the main focus. In particular, we show that our SPR procedure for the improvement of derivatives fulfills the desired consistency criteria. At the end, we develop a posteriori error estimator where the improved gradient obtained from the proposed recovery procedures is used.

Numerical results are presented to illustrate the efficiency of using SPR procedure for the improvement of derivatives (or gradient) of computed solution in isogeometric analysis. Then the proposed a posteriori error estimator based adaptive refinement

* Corresponding author.
E-mail addresses: kumarm@cofc.edu (M. Kumar), Trond.Kvamsdal@math.ntnu.no (T. Kvamsdal), Kjetil.Andre.Johannessen@math.ntnu.no (K.A. Johannessen).
[1] Present address: Department of Mathematics, College of Charleston, Charleston, SC 29424, USA.

http://dx.doi.org/10.1016/j.cma.2016.11.014

methodology is tested to solve smooth and non-smooth elliptic benchmark problems. The focus is put on whether optimal convergence rates are obtained in the computed solution or not, as well as the effectivity index of the proposed error estimators.

Keywords: Isogeometric analysis; LR B-splines; NURBS; A posteriori error estimator; Adaptivity; Superconvergence

1. Introduction

Reliability and efficiency are two major challenges in simulation based engineering. These two challenges may be addressed by error estimation combined with adaptive refinements. A lot of research has been performed on error estimation and adaptive mesh refinement over the years. However, adaptive methods are not yet an industrial tool, partly because the need for a link to traditional Computer Aided Design (CAD)-systems makes this difficult in industrial practice. Here, the use of an isogeometric analysis framework introduced by Professor Thomas J.R. Hughes (The University of Texas at Austin) and co-workers [1] may facilitates more widespread adoption of this technology in industry, as adaptive mesh refinement does not require any further communication with the CAD system.

Isogeometric analysis (IGA) has been introduced in [1] as an innovative numerical methodology for the discretization of Partial Differential Equations (PDEs). The main idea was to improve the interoperability between CAD and PDE solvers. To achieve this, authors in [1] proposed to use CAD mathematical primitives, i.e., splines and NURBS, also to represent PDE unknowns. The smoothness of splines is useful in improving the accuracy per degree of freedom and solving higher order PDEs via direct approximations. Isogeometric methods have been used and tested on a variety of problems of engineering interests, see [1,2] and references therein. The development on the mathematical front started with h-approximation properties of NURBS in [3], further studies for hpk-refinements in [4] and for anisotropic approximation in [5]. The recently published article in Acta Numerica [6] is definitely an advancement in this direction.

Non-uniform rational B-splines (NURBS) are the dominant geometric representation format for CAD. The construction of NURBS are based on a tensor product structure and, as a consequence, knot insertion (which is the means for h-refinement) has a global impact on the mesh. To remedy this a local refinement can be achieved by breaking the global tensor product structure of multivariate splines and NURBS. In the current literature there are three different ways to achieve local refinement: T-splines, LR splines and hierarchical splines. In this article, we will focus on LR-splines, introduced by Dokken et al. [7]. Johannessen et al. [8] developed adaptive local refinement techniques for isogeometric finite elements based on LR B-splines. LR B-splines have been investigated and utilized together with a newly developed a posteriori error estimate by Kumar et al. [9]. Furthermore, LR B-splines have been studied in [10], extended to facilitate divergence conforming discretization for Stokes problem [11], and applied to adaptive simulation of porous media flow [12]. A comparison of LR B-splines towards hierarchical splines may be found in [13]. An algorithm for Bézier decomposition of LR B-splines may be found in Stahl et al. [14] that enables an accurate, efficient and practical post-processing pipeline for visualization of adaptive isogeometric analysis results. Readers interested in T-splines and hierarchical splines are referred to the following references: T-splines were initially introduced in [15] and their use in isogeometric analysis was first investigated in [16,17] and later a special class of analysis suitable T-spline is developed in [18]; hierarchical splines have been first introduced in [19] and studied within the isogeometric analysis in the papers [20,21] and others. Recently, there has been much progress on the topic of the generalization of splines construction which allows local refinement, but an automatic reliable and efficient adaptive refinement procedure is still one of the key issues in isogeometric analysis. To achieve a fully automatic refinement procedure to solve PDEs problem in adaptive isogeometric analysis an *a posteriori error estimate* is required. This is the subject of the current work.

1.1. A posteriori error estimations: An overview

Since 1970s several strategies have been developed to estimate the discretization error of Finite Element (FE) solutions. The first a posteriori error estimates were introduced by Babuška and Rheinboldt in 1978, see [22,23]. Since then many different error estimation techniques have been introduced. The existing techniques to obtain energy estimates may be classified into two main categories:

- *Residual based estimates*: The approximate FE solution does not satisfy the governing partial differential equation. This lack of fulfillment is called the residual and the error can be estimated by solving local problems where the load functions are given by the local residuals.
- *Recovery-based estimates*: These estimates employ a projection technique in order to recover a post-processed quantity (usually the stresses) from the FE solution. The error is then estimated by taking the difference between the recovered solution and the FE solution.

The first category of estimates mimics the optimal bounds used to prove the convergence of finite element discretization schemes. For example, an explicit residual based estimate is very easy to implement but it includes interpolation constants that are problem dependent and difficult to obtain in general. This makes them less popular among the engineers. On the other hand, for the implicit residual based approach a finite element problem with a very fine discretization is solved over each of the local subdomains (either individual elements [24,25], patches of elements [22] or subdomains consisting of an element and its neighborhood elements [26]). Depending on how the local problem is linked to the global FE solution different properties of the estimates can be obtained. For instance, the equilibrated element approach, the flux free approach, and the constitute relation error yield estimates that give an upper bound on the error, while error estimates based on local problems with Dirichlet boundary conditions gives the lower bound on the error [27]. A more detailed discussion about this class of estimates can be found in [28,24,29].

The second category consists of deriving simple smoothing technique that yields a solution field that converges faster than the FE solution. A very popular prototype for such approaches is the Zienkiewicz–Zhu estimate (so called ZZ estimate). Initial reference to such estimates can be found in [30], and further development with Superconvergent Patch Recovery (SPR) in [31,32]. The success of this approach in the engineering community relies on an intuitive mechanical definition and a certain ease of implementation compared to other class of available error estimates, without sacrificing the numerical effectivity.

Many contributions have also been devoted to obtain a guaranteed upper bound on the error, that some residual based technique offers, while retaining the simple implementation of the ZZ-estimates framework. The key idea was that when the recovered stress field is statically admissible then the ZZ-estimate coincides with the constitutive relation error and bounds the energy error from above. Different methodologies following this approach have been presented in [33–35] to obtain practical computable upper bounds for the error in energy norm using SPR. These smoothing techniques are not limited to classical finite element methods, and have been extended to enriched approximations in [36,37] and to smoothed finite elements (SFEM) in [38].

The use of a posteriori error estimators in isogeometric analysis is still in its infancy. To the best of our knowledge only these work has been done in this direction, see [39,40,17,41–44,21,45–47]. The authors in [17] used the idea of hierarchical bases with bubble functions approach of Bank and Smith [48] to design a posteriori error estimator for T-splines, which was also used in [39,21]. But their performance was less satisfactory due to the needed saturation assumption as noted on page 41 of [41]. Another simple idea of explicit residual based error estimator has been explored in [40,41,44–47]. They require the computation of constants in Clement-type interpolation operators. Such constants are mesh (element) dependent and often incomputable for general element shapes. A global constant can overestimates the local constants, and thus the exact error. A functional-type a posteriori error estimate for isogeometric discretization is presented in [42]. This type of error estimate was introduced in [49,50] on functional grounds. They are applicable for any conforming and non-conforming discretizations and are known to provide a guaranteed and computable error bounds. But the hindrance in their popularity is due to high cost of computations which are based on solving a global minimization problem (Majorant minimization problem) in H(div) spaces. In [42], authors made an attempt to reduce the cost of computations for tensorial spline spaces but the same idea of cost reduction needs further study in adaptive isogeometric analysis. To the best of the authors knowledge, in the above mentioned work on the use of a posteriori error estimators in isogeometric analysis, the role of error estimator has been limited to either just as an indicator to perform adaptive refinement steps or the error estimation computation performance is presented only on tensorial meshes. Recently, the present authors developed two simple a posteriori error estimators for adaptive isogeometric analysis in [9], and for the first time a complete study about the performance of error estimators in adaptive isogeometric is presented.

The idea is based on a Serendipity pairing of two discrete approximation spaces defined on the same mesh, where one of the spaces is a k-refinement of the other, i.e. has one order higher polynomial degree as well as one order higher continuity. The use of k-refinement is a unique feature within isogeometric analysis and enables a higher

order accurate isogeometric finite element approximation by means of marginally increasing the number of degrees of freedom.

In this article we explore another approach to design a posteriori error estimate in the setting of Zienkiewicz–Zhu [30] where the improved gradient from recovery procedure is used instead of exact gradient of the exact solution. The recovery based estimators are very popular in engineering community because of their simple implementation and as they also provide good effectivity indices. In an extensive study on the quality of different a posteriori error estimates belonging to first two categories above (residual based vs. recovery based), Babuška and co-workers concludes in [51–53] that the Superconvergent Patch Recovery (SPR) technique developed by Zienkiewicz and Zhu [31,32] is the most robust estimator for the class of smooth solutions approximated on patch-wise uniform grids of linear or quadratic elements. In this article, we first develop the SPR procedure to improve the derivatives (or gradient) of the isogeometric finite element solution. Then using the idea of Zienkiewicz–Zhu [30] we propose a recovery based a posteriori error estimation technique and verify its effectiveness for B-splines, NURBS, and LR-spline elements in isogeometric analysis.

We also address the problem of existence of derivative superconvergence points in the context of B-splines and LR B-splines based Galerkin discretization. The superconvergence in the classical finite element method (FEM) is a well known phenomenon, where the order of convergence of the finite element error, at certain special points within an element, is higher than the order of convergence of the maximum of the finite element error over that element. These special points are called natural superconvergence points. This phenomena was first address in [54], and the term superconvergence was first used in [55]. Superconvergence has been extensively studied since late 1970s a few references are [56–68], and several books have written on superconvergence in the finite element method, e.g., [24,69–73]. A systematic *computer based approach* was introduced in [58] for the analysis of superconvergence in the context of the finite element method. It was shown that the existence of natural superconvergence points was equivalent to the existence of roots of a system of polynomial equations. Moreover, the superconvergence points are obtained from these roots, which (the roots) are computed numerically. In special situations, the system of equations can be written explicitly and roots can be computed analytically, as shown in [67,68]. Using this idea a simple procedure to compute the superconvergence points for spline based uniform discretization is proposed in [74]. In this article we follow the main theme of *computer based approach* of [58], i.e., we involve on each patch computation of local Neumann projection and solving local Newton problems to obtain the location of derivative superconvergence points. We remark here that our results presented in Tables 2–3 confirm the location of superconvergence points on uniform meshes presented by Wahlbin in Table 1 in [74]. We hope that the work presented in this article will initiate more activities on superconvergence in isogeometric analysis and their applications for engineering interests.

1.2. Upper error bounds vs. Accurate error estimates

In this section we compare the performance of two simple error estimates; an explicit residual based error estimate used in [40,41,44–47] *vs*. SPR based ZZ-estimate developed in this article. The main focus will be on the approximation of true error and quality of estimates measure in terms of effectivity index θ, which can be defined by the ratio of estimated error by exact isogeometric FE error.

Let η_{Res} be an explicit residual based error estimate similar to what has been used in [40,41,44–47], which can be obtained from the Galerkin formulations (20) and (22) of the model problem (17)-(19) after following the standard procedure from [24], and is given by

$$\|\nabla u - \nabla u_h\|_{L^2(\Omega)} \leq C\eta_{Res}, \quad \text{with } \eta_{Res} = \left(\sum_{\forall K\in\mathcal{M}} \eta^2_{Res,K}\right)^{1/2}, \tag{1}$$

where

$$\eta_{Res,K} = h_K^2\|r\|^2_{L^2(K)} + \frac{1}{2}h_K\|R\|^2_{L^2(\partial K)}.$$

Here u is the analytical solution of the model problem, u_h is the corresponding finite element solution, f is the loading, $r = f + \Delta u_h$ defined the interior residual and R defined the boundary residual $R|_\gamma = g - \frac{\partial u_h}{\partial n}$ for $\gamma \in \partial K \cap \partial\Gamma_N$ and the jump term $R|_\gamma = -\frac{1}{2}\left[\frac{\partial u_h}{\partial n}\right]$ for $\gamma \in \partial K$, and h_K is the diameter of element $K \in \mathcal{M}$. The contribution of

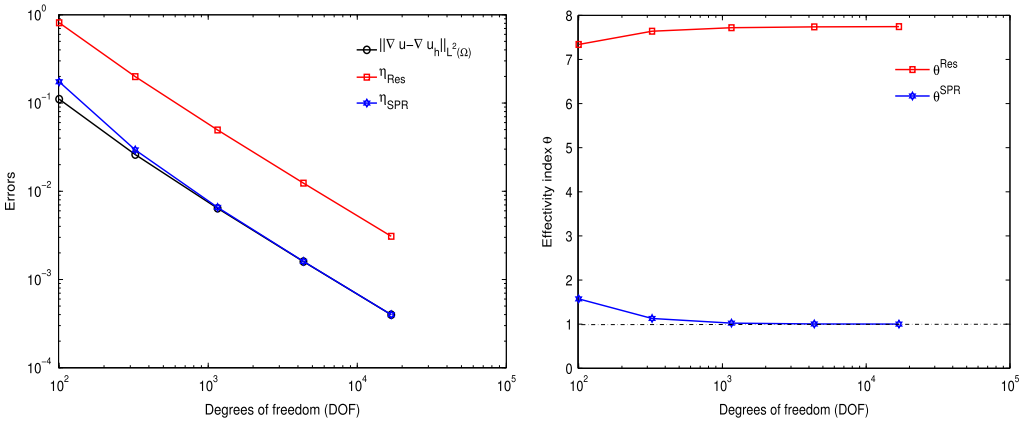

(a) Errors. (b) Effectivity index θ.

Fig. 1. Sinus problem: Comparison of errors and effectivity index between *residual based error estimate* (η_{Res}) and the proposed *SPR based error estimate* (η_{SPR}) for isogeometric FE using quadratic B-splines with uniform h-refinement.

element jump discontinuity term becomes zero for smooth spline approximation spaces, which generally have at least C^1-continuity across the element boundaries. The error constant C is generally not known and as a result the bound on the inequality (1) become very conservative. Here we consider η_{Res} from (1) as the classical explicit residual based estimator, cf. [40,41,44–47]. We follow here the common practice in the FEM and IGA community to set the constant $C = 1$, see e.g. [40,41,44–47], but acknowledges that this is not an optimal choice.

Now we define $\eta_{SPR} := \|\nabla u_h^{SPR} - \nabla u_h\|_{L^2(\Omega)}$ the Superconvergent Patch Recovery (SPR) based error estimate developed in the present article, where ∇u_h^{SPR} is the recovered gradient of the computed FE solution ∇u_h using the SPR procedure of Section 4.2. In Fig. 1 we show the comparison between the exact error $\|\nabla u - \nabla u_h\|_{L^2(\Omega)}$, the estimated errors η_{Res}, η_{SPR}, and the effectivity index θ obtained for **Sinus problem** defined in Example 1 of Section 7. We have here used quadratic isogeometric finite elements and uniform h-refinements. The comparison of exact and estimated errors for the **L-shaped domain** problem with singularity at the corner $(0, 0)$ defined by Example 8 of Section 7 for both error estimates are shown in Fig. 2. Here the adaptively refined meshes are obtained by using LR B-splines. Both examples show the accurate estimation of the error in case of SPR procedure in comparison to the upper bound on the error achieved by the explicit residual based error estimator. Also the SPR based error estimator shows h-asymptotic exactness behavior, i.e. when the mesh is refined the estimated error converges to the exact error and provides a very accurate approximation of it. The main aim of the present article is just to address the development of an accurate and efficient error estimator for adaptive isogeometric analysis.

1.3. Outline of the article

The article is organized as follows; In Section 2, the definitions of B-splines, NURBS and LR B-splines which is necessary to built an approximation spaces in isogeometric analysis is briefly introduced. In Section 3, an elliptic model problem and its isogeometric FE approximation together with a priori error estimates is introduced. We close the section after developing the idea of a recovery based a posterior error estimation and its asymptotic exactness. In Section 4, different gradient recovery procedures are developed to improve the derivatives (or gradient) of isogeometric FE solutions. The SPR procedure will be the main focus in this section. In Section 5, the local behavior of spline based Galerkin discretization is analyzed. The section start with the motivational study of natural superconvergence for one dimensional elliptic problem based on elliptic Ritz projection. Later a more general idea of local Neumann elliptic projection is established, which is suitable for multi-dimensional problems, and based on this we compute the location of true derivative superconvergence points for our model elliptic problems, e.g., Poisson and Laplace equations. In Section 6, we verify that the SPR procedure of the present article satisfies the Abstract Recovery Operator definition (or conditions) of Ainsworth and Craig [75]. These conditions together with superconvergence property of isogeometric FE solution can be used to show the superconvergence results for the SPR procedure. Numerical experiments are performed in Section 7 for three main classes of mesh refinements investigating the

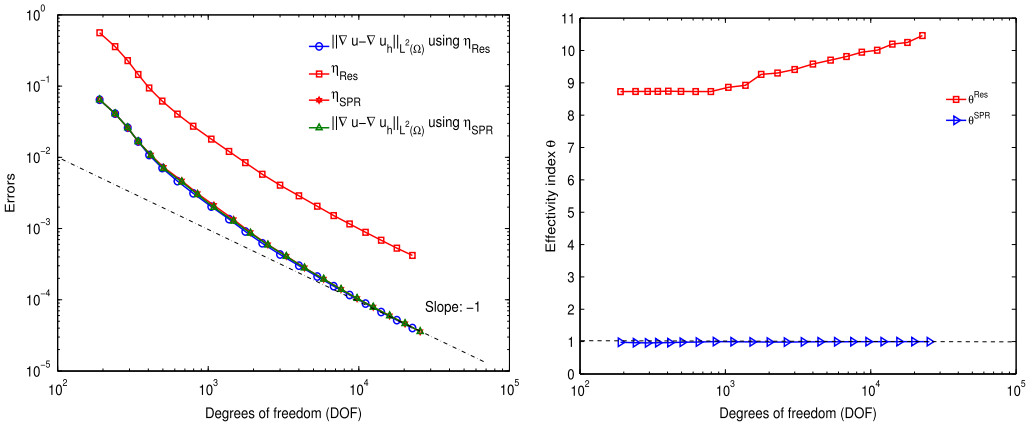

(a) Errors. (b) Effectivity index θ.

Fig. 2. L-shaped domain problem: Comparison of errors and effectivity index between *residual based error estimate* (η_{Res}) and the proposed *SPR based error estimate* (η_{SPR}) for isogeometric FE using quadratic LR B-splines with adaptive h-refinement.

proposed techniques for superconvergent recovery on: (1) Uniform h-refinement, (2) Adaptive refined meshes, and (3) Adaptive refined meshes using a posteriori error estimates. We end this article with concluding remarks and perspectives based on our findings in Section 8.

2. Approximation spaces in isogeometric analysis

In order to introduce the notation and to provide an overview, we recall the definition and some aspects of isogeometric analysis using B-splines, NURBS and LR B-splines basis functions and their geometry mappings.

2.1. B-splines and NURBS

Given two positive integers p and n, we introduce the (ordered) knot vector

$$\Xi := [\xi_1, \xi_2, \ldots, \xi_{n+p+1}] \text{ with } \xi_i \leq \xi_{i+1}\ \forall i, \tag{2}$$

where p is the degree of the B-spline and n is the number of basis functions (and control points) necessary to describe it. Here we allow repetition of knots, that is, $\xi_i \leq \xi_{i+1}\ \forall i$. The maximum multiplicity we allow is $p+1$. In the following we will only work with open knot vectors, which means that first and last knots in Ξ have multiplicity $p+1$. Given a knot vector Ξ, univariate B-spline basis functions $B_{i,p}(\xi)$, $i = 1, \ldots, n$, are defined recursively by the well known Cox–de Boor recursion formula:

$$B_{i,0}(\xi) = \begin{cases} 1 & \text{if } \xi_i \leq \xi < \xi_{i+1}, \\ 0 & \text{otherwise.} \end{cases} \tag{3}$$

$$B_{i,p}(\xi) = \frac{\xi - \xi_i}{\xi_{i+p} - \xi_i} B_{i,p-1}(\xi) + \frac{\xi_{i+p+1} - \xi}{\xi_{i+p+1} - \xi_{i+1}} B_{i+1,p-1}(\xi) \text{ if } \xi_i \leq \xi < \xi_{i+1}, \tag{4}$$

where in (4), we adopt the convention $0/0 = 0$.

Let $M_{i,p}$ and $N_{j,q}$ with $i = 1, \ldots, n$ and $j = 1, \ldots, m$, be the B-spline basis functions of degree p and q defined by open knot vector $\Xi = [\xi_1, \xi_2 \ldots, \xi_{n+p+1}]$ and $\Psi = [\psi_1, \psi_2, \ldots, \psi_{m+q+1}]$, respectively. Then by means of tensor products, a multi-dimensional B-splines can be constructed as $B_{i,j}^{p,q}(\xi, \psi) = M_{i,p}(\xi) \cdot N_{j,q}(\psi)$. In general, a rational B-spline in $\mathbb{R}^d$ is the projection onto d-dimensional physical space of a polynomial B-spline defined in $(d-1)$-dimensional homogeneous co-ordinate space. Let $C_{ij} \in \mathbb{R}^2$ be the control points and $w_{ij} = (C_{ij}^w)_3$ are the positive weights given by projective control points $C_{ij}^w \in \mathbb{R}^3$. Then NURBS basis on two dimensional parametric

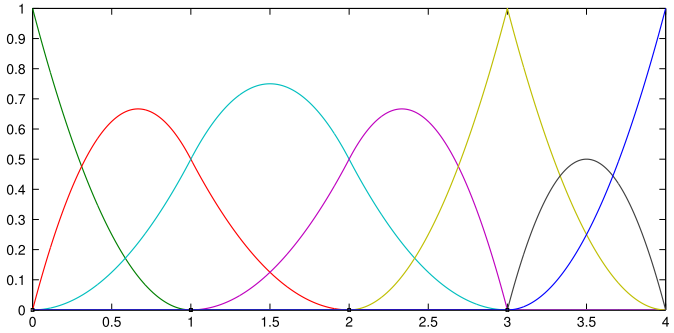

Fig. 3. All quadratic basis functions generated by the knot $\Xi = [0, 0, 0, 1, 2, 3, 3, 4, 4, 4]$. Each individual basis function $B_{i,2}$ (represented by different colors) can be described using a local knot vector Ξ_i of length 4 described in (6). (For interpretation of the references to color in this figure legend, the reader is referred to the web version of this article.)

space $\hat{\Omega} = [0, 1]^2$ are defined as

$$R_{i,j}(\xi, \psi) = \frac{M_{i,p}(\xi) N_{j,q}(\psi) w_{ij}}{\sum_{\hat{i}=1}^{n} \sum_{\hat{j}=1}^{m} M_{\hat{i},p}(\xi) N_{\hat{j},q}(\psi) w_{\hat{i}\hat{j}}}. \tag{5}$$

Observe that the continuity and support of NURBS basis function are the same as for B-splines. Furthermore, B-splines can be seen as a special case of NURBS with all weights being equal to one.

2.2. Local h-refinement using LR B-splines

In the following, we present a class of Locally Refined (LR) B-splines. For a more detailed presentation of LR B-splines, including an overview of corresponding refinement algorithm that results in a proper LR B-spline space to perform structured adaptive refinement in this article, we refer to our previous work in [8].

Local knot vectors

We have seen that a univariate spline basis function is constructed using a recursive formula of (3) and (4) with the global knot vector Ξ. However the support of a B-spline function $B_{i,p}$ is contained in $[\xi_i, \xi_{i+p+1}]$ and the knots $[\xi_i, \xi_{i+1} \ldots, \xi_{i+p+1}]$ only contribute to the definition of $B_{i,p}$. Thus we do not need the global knot vector Ξ to define $B_{i,p}$, we consider a *local knot vector*

$$\Xi_i = \{\xi_{i+j}\}_{j=0}^{p+1}, \quad \text{for } i = 1, \ldots, n, \tag{6}$$

and use it in conjunction with (3) and (4) to define $B_{i,p}$. We have illustrated the basis functions given by $\Xi = [0, 0, 0, 1, 2, 3, 3, 4, 4, 4]$ in Fig. 3.

The concept of local knot vectors is important for LR B-splines as they are used as the building blocks. Now we recall the concept of knot insertion, that will be the focus of our investigation on LR B-splines, see also [8]. As we are considering the same degree basis in multivariate case so we drop the degree subscript p from the notation $B_{i,p}$.

Knot insertion

For local h-refinement, we again turn to existing spline theory. Tensor product B-splines form a subset of the LR B-splines and they obey some of the same core refinement ideas. From the tensor product B-spline theory we know that one might insert extra knots to enrich the basis without changing the geometric description. This comes from the fact that we have the available relation between B-splines in the old coarse spline space and in the new enriched spline space. For instance if we want to insert the knot $\hat{\xi}$ into the knot vector Ξ between the knots ξ_{i-1} and ξ_i, then the relation is defined by

$$B_{\Xi}(\xi) = \alpha_1 B_{\Xi_1}(\xi) + \alpha_2 B_{\Xi_2}(\xi), \tag{7}$$

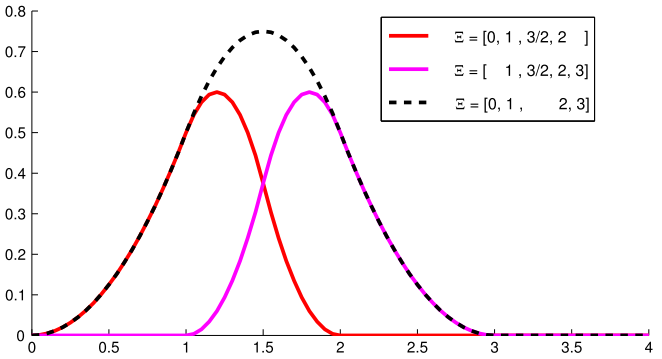

Fig. 4. Splitting a B-spline function *via* inserting the knot $\xi = \frac{3}{2}$ in $\Xi = [0, 1, 2, 3]$.

where

$$\alpha_1 = \begin{cases} 1, & \xi_{p+1} \le \hat{\xi} \le \xi_{p+2}, \\ \dfrac{\hat{\xi} - \xi_1}{\xi_{p+1} - \xi_1}, & \xi_1 \le \hat{\xi} \le \xi_{p+1}, \end{cases} \tag{8}$$

$$\alpha_2 = \begin{cases} \dfrac{\xi_{p+2} - \hat{\xi}}{\xi_{p+2} - \xi_2}, & \xi_2 \le \hat{\xi} \le \xi_{p+2}, \\ 1, & \xi_1 \le \hat{\xi} \le \xi_2, \end{cases} \tag{9}$$

and the knot vectors are $\Xi_1 = [\xi_1, \xi_2, \dots \xi_{i-1}, \hat{\xi}, \xi_i, \dots \xi_{p+1}]$ and $\Xi_2 = [\xi_2, \dots \xi_{i-1}, \hat{\xi}, \xi_i, \dots \xi_{p+1}, \xi_{p+2}]$. Let us look at an example using this technique. Say we want to insert $\hat{\xi} = \frac{3}{2}$ into the B-spline $\Xi = [0, 1, 2, 3]$. This would give us $\alpha_1 = \alpha_2 = \frac{3}{4}$ and the three functions are plotted in Fig. 4.

To refine the bivariate B-spline basis function $B_{\Xi,\Psi}(\xi, \psi) = B_\Xi(\xi) \cdot B_\Psi(\psi)$ we consider the refinement of the basis function in one parametric direction at a time. By using the splitting algorithm in (7) when splitting in ξ-direction, we obtain

$$\begin{aligned} B_{\Xi,\Psi}(\xi, \psi) &= B_\Xi(\xi) \cdot B_\Psi(\psi) \\ &= (\alpha_1 B_{\Xi_1}(\xi) + \alpha_2 B_{\Xi_2}(\xi)) \cdot B_\Psi(\psi) \\ &= \alpha_1 B_{\Xi_1,\Psi}(\xi, \psi) + \alpha_2 B_{\Xi_2,\Psi}(\xi, \psi). \end{aligned}$$

Now we define a weighted B-spline $B^\gamma_{\Xi,\Psi}(\xi, \psi) := \gamma B_{\Xi,\Psi}(\xi, \psi)$, with the weight factor $\gamma \in (0, 1]$. This is to ensure that LR B-splines maintain the partition of unity property, and it is noted that the weight factor γ is different from the rational weight w which is common in NURB representation. Refining a bivariate weighted B-splines becomes

$$B^\gamma_{\Xi,\Psi}(\xi, \psi) = \gamma B_{\Xi,\Psi}(\xi, \psi) \tag{10}$$

$$= \gamma\alpha_1 B_{\Xi_1,\Psi}(\xi, \psi) + \gamma\alpha_2 B_{\Xi_2,\Psi}(\xi, \psi) \tag{11}$$

$$= B^{\gamma_1}_{\Xi_1,\Psi}(\xi, \psi) + B^{\gamma_2}_{\Xi_2,\Psi}(\xi, \psi), \tag{12}$$

where $B^{\gamma_1}_{\Xi_1,\Psi}$ and $B^{\gamma_2}_{\Xi_2,\Psi}$ are new weighted B-spline basis functions with weights $\gamma_1 = \gamma\alpha_1$ and $\gamma_2 = \gamma\alpha_2$, respectively.

Local refinement algorithm

We now have the main ingredients to formulate the LR B-spline refinement rules. This will be done by keeping track of the mesh $\mathcal{M}_\ell$ at level ℓ and the corresponding spline space $\mathcal{S}_\ell$. For each B-spline basis $B^{\gamma_k}_{\Xi_k,\Psi_k}$, where k is a single running global index, we store the following:

- Ξ_k, Ψ_k-local knot vectors in the each parametric direction.
- γ_k-scaling weights and C_k-control points.

Through the refinement we aim at keeping the partition of unity and leaving the geometric mapping unchanged, i.e., $\sum_{\forall k} B^{\gamma}_{\Xi_k,\Psi_k}(\xi,\psi) = 1$ and $\mathbf{F}(\xi,\psi) = \sum_{\forall k} B^{\gamma}_{\Xi_k,\Psi_k}(\xi,\psi) C_k$ at all levels of refinements.

Assuming a meshline $\mathcal{E}$ is inserted, the refinement process is characterized by two steps.

- **Step 1:** Split a B-spline whose support is completely traversed by the *new* meshline—update the weights and control points.
- **Step 2:** For all new B-splines, check if their support is completely traversed by any *existing* meshline.

On the basis of the above characterization is fulfilled at each refinement level, **Algorithm 1** is proposed in [8] to construct the LR B-spline space. The "update control points and weights" step consists of that a parent basis function B_i is split into two newly created B-spline functions B_1 and B_2, see (10). If B_1 is not present in LR B-spline list then we add it to the list and set its weight and control points equal to its parent function, i.e., $\gamma_1^{new} = \alpha_1\gamma_i$ and $C_1^{new} = C_i$. While if the newly created function is already exits in our spline space then we just update its control points and weight such as $C_1^{new} := (C_1\gamma_1 + C_i\gamma_i\alpha_1)/(\gamma_1 + \gamma_i\alpha_1)$ and $\gamma_1^{new} := \gamma_1 + \gamma_i\alpha_1$. Finally we remove the old basis functions from the spline space.

Algorithm 1 Local refinement algorithm

```
Input parameters: Spline space (S), LR mesh(M), Meshline (E)
for every B-spline B_i ∈ S do
if E traverse support of B_i then
    refine B_i according to Eq. (10)
    Update control points C and weights γ
end if
end for
update S to S_new and M to M_new
for every existing B_i ∈ S_new do
for every edges E_i ∈ M_new do
if E_i traverse support of B_i then
    refine B_i according to Eq. (10)
    Update control points C and weights γ
    (These steps may enlarge S_new space further)
end if
end for
end for
```

We now define an LR spline as an application of the above refinement algorithm.

Definition 2.1 (*LR Spline*)**.** An LR spline $\mathcal{L}$ consist of $(\mathcal{M},\mathcal{S})$, where $\mathcal{M}$ is an LR mesh and $\mathcal{S}$ is a set of LR B-splines defined on $\mathcal{M}$, and

- At each refinement level, $\mathcal{M}_{\ell+1} := \mathcal{M}_\ell \cup \mathcal{E}_\ell$, where $\mathcal{E}_\ell$ is a new meshline extension.
- $\mathcal{S}_\ell := \{B_{\Xi_k,\Psi_k}(\xi,\psi)\}_{k=1}^{m}$ is a set of all LR B-splines on $\mathcal{M}_\ell$ as a results of **Algorithm** 1.

In [8], authors has illustrated two main isotropic h-refinement strategies as shown in Fig. 5. A *full span* refinement strategy split an element with a knotline insertion which transverses through the support of every B-splines on the marked elements. The idea of refining elements is a legacy from the finite element method where every inserted vertex would correspond to an additional degree of freedom. With LR B-splines this is not the case as the required length of the inserted meshlines may vary from element to element. Another way of refining LR B-splines is identifying the *B-spline* which needs to be refined as opposed to which elements does, a *structured mesh* refinement strategy based on this approach is shown in Fig. 5(b).

LR spline space properties

Consider an LR spline $(\mathcal{M},\mathcal{S})$ defined above in Definition 2.1. Then the following holds true

- $\sum_{\forall k} B^{\gamma}_{\Xi_k,\Psi_k}(\xi,\psi) = 1$, i.e., LR B-splines form a partition of unity.
- $(\mathcal{M}_\ell,\mathcal{S}_\ell) \subset (\mathcal{M}_{\ell+1},\mathcal{S}_{\ell+1})$, i.e., the LR spline is nested.

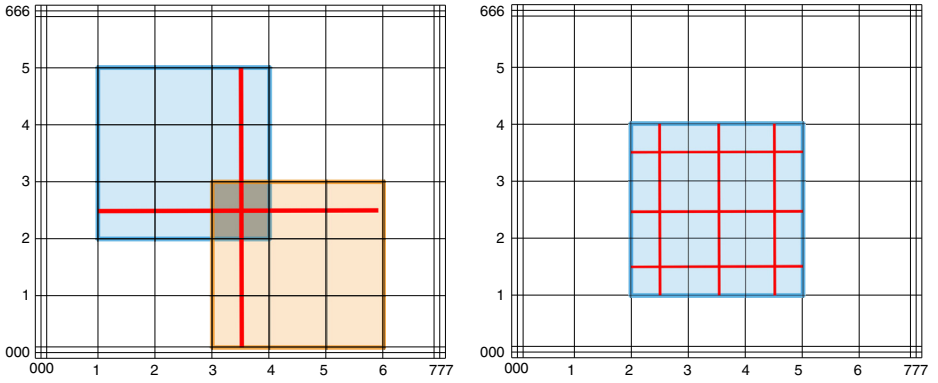

(a) Full span—split all functions on one element, here only two out of all the nine functions within the support on one element is depicted.

(b) Structured Mesh—split all knot spans on one B-spline basis, notice that no bad aspect ratio elements are created.

Fig. 5. The ideas behind the different refinement strategies illustrated on a quadratic tensor product mesh. Note the fundamental difference in 5(a) is refining an element, while 5(b) is refining a B-spline basis.

- If two meshline insertion sequences $\mathcal{E}$ and $\tilde{\mathcal{E}}$ result in LR spline meshes $\mathcal{M}$ and $\tilde{\mathcal{M}}$ which are equal then the spline spaces $\mathcal{S}$ and $\tilde{\mathcal{S}}$ result on these LR meshes will be equal. This shows the construction of LR B-splines during the refinement is order independent.
- $\mathcal{S} := \{B_{\Xi_k,\Psi_k}\}_{k=1}^{m}$ does not in general form a linear independent set.

As it has been pointed out it is not guaranteed that an arbitrary LR mesh is producing a linear independent set of functions, however there are several ways to ensure that the set of functions is linearly independent, see [7,8]. In this article, we focus on the structured mesh refinement strategy 5(b) which provides structured adaptive meshes using LR B-splines.

2.3. Geometry mappings

A single patch domain Ω is a NURBS region associated with the control points C_{ij}, and introduce the geometrical map $\mathbf{F} : \hat{\Omega} \to \bar{\Omega}$ by

$$\mathbf{F}(\xi,\psi) = \sum_{i=1}^{n}\sum_{j=1}^{m} C_{ij} R_{i,j}(\xi,\psi). \tag{13}$$

The above equation gives a B-spline region in a special case when all weights equal to one. Following the isoparametric approach, the space of NURBS(or B-splines) vector fields on the patch Ω is defined by the span of the push-forward of their respective basis function, e.g., in case of NURBS

$$V_h = \text{span}\{R_{i,j} \circ \mathbf{F}^{-1}, \ \text{ with } \ i = 1,\ldots,n; \ \ j = 1,\ldots,m\}. \tag{14}$$

For LR B-splines, these will instead be defined over a single running global index k using the local knot vectors Ξ_k and Ψ_k (defined by a subsequences of global knot vectors Ξ and Ψ, respectively) by

$$\mathbf{F}(\xi,\psi) = \sum_{k=1}^{N_{dim}} \gamma_k C_k B_{\Xi_k,\Psi_k}(\xi,\psi), \tag{15}$$

where $B_{\Xi_k,\Psi_k}(\xi,\psi) = B_{\Xi_k}(\xi)\cdot B_{\Psi_k}(\psi)$ and γ_k is a weighting factor needed to obtained partition of unity, as discussed in Section 2.2. The isoparametric approach gives the space of LR B-splines vector fields on Ω by

$$V_h = \text{span}\{B_{\Xi_k,\Psi_k}(\xi,\psi) \circ \mathbf{F}^{-1}, \ \text{ with } \ k = 1,\ldots,N_{dim}\}. \tag{16}$$

3. Error estimation

The model problem is Poisson's equation on an open bounded two dimensional domain $\Omega \in \mathbb{R}^2$ with Lipschitz boundary $\Gamma = \Gamma_D \cup \Gamma_N$, where Γ_D and Γ_N are the Dirichlet and Neumann boundaries, respectively. The *strong* form of the boundary value problem: Find $u : \bar{\Omega} \to \mathbb{R}$ such that

$$-\Delta u = f \ \text{ on } \ \Omega; \tag{17}$$

$$u = 0 \ \text{ on } \ \Gamma_D; \tag{18}$$

$$\mathbf{n} \cdot \nabla u = g \ \text{ on } \ \Gamma_N \tag{19}$$

where u is the analytical solution and the data are assumed to be sufficiently smooth, that is, $f \in L^2(\Omega),\ g \in L^2(\Gamma_N)$ and $\mathbf{n}$ is the unit outward normal vector to Γ.

The variational formulation of the boundary value problem: find $u \in V$ such that

$$a(u, v) = \ell(v) \ \ \forall\, v \in V, \tag{20}$$

where the trial and test space V is the usual Sobolev space of functions from $H^1(\Omega)$ whose trace vanishes on the Dirichlet part of the boundary, and is defined by $V := \{v \in H^1(\Omega) \ : \ v = 0 \text{ on } \Gamma_D\}$, $a(u, v)$ is assumed to be a V-coercive bilinear form on $V \times V$ and the linear functional $l(v)$ is an element of the dual space V', defined by, respectively

$$a(u, v) = \int_\Omega \nabla u \cdot \nabla v d\Omega \quad \text{and} \quad \ell(v) = \int_\Omega f v d\Omega + \int_{\Gamma_N} g v ds. \tag{21}$$

The Galerkin finite element approximation to this variational problem is given as follows: Given a finite-dimensional subspace $V_h \subset V$ and $\ell \in V'$, find $u_h \in V_h$ such that

$$a(u_h, v_h) = \ell(v_h) \ \ \forall\, v_h \in V_h. \tag{22}$$

In an isogeometric setting, the discrete space V_h formed with NURBS (or B-splines) and LR B-splines are defined by (14) and (16), respectively. Let u_h be the discrete solution given by

$$u_h = \sum_{A=1}^{N_{dim}} c_A R_A \tag{23}$$

with the corresponding basis function R_A and the unknown control variables c_A.

For the discretization error $e(\mathbf{x}) = u(\mathbf{x}) - u_h(\mathbf{x})$, the error in L^2 norm is defined by

$$\|e\|_{L^2(\Omega)} := \|u - u_h\|_{L^2(\Omega)} = \left(\int_\Omega (u - u_h)^2 d\Omega \right)^{1/2} \tag{24}$$

and the error in the energy norm is defined by

$$\|e\|_E = \sqrt{a(e, e)} = |e|_{H_0^1(\Omega)} = \left(\int_\Omega (\nabla u - \nabla u_h)^T \cdot (\nabla u - \nabla u_h) d\Omega \right)^{1/2}. \tag{25}$$

3.1. A priori error estimation

In classical Finite Element Analysis (FEA), the fundamental error estimate for the elliptic boundary value problem takes the form

$$\|u - u_h\|_m \leq C h^\beta \|u\|_r \tag{26}$$

where u is the exact solution and u_h is the FEA solution, $\|\cdot\|_k$ is the norm corresponding to the Sobolev space $H^k(\Omega)$, h is a characteristic length scale related to the size of the element in the mesh and $\beta = \min(p + 1 - m, r - m)$ where

p is the polynomial degree of the basis, and C is a constant that neither depends on u nor h. The parameter r describes the regularity of the exact solution u and $2m$ is the order of the differential operator of the corresponding PDE.

A priori error estimate results analogous to (26) for NURBS based isogeometric Galerkin discretization can be given as follows:

Theorem 3.1. *Let $u \in H^r(\Omega)$ be the exact solution of the elliptic boundary value problem and $u_h \in V_h$ be the approximate solution obtained with the NURBS based isogeometric discretization of (22). Then, the following a priori error estimate holds for $0 \leq m \leq r \leq p+1$:*

$$\|u - u_h\|_m \leq C_{shape} h^{\beta} \|u\|_r, \quad \text{where } \beta = \min(p+1-m, r-m). \tag{27}$$

For the technical details we encourage the reader to consult the original articles [76,5]. For the uniform h-refinement, it is interesting to see from (26) and (27) that the isogeometric solution obtained using C^{p-1} NURBS of degree p can converge at same rate as a FEA polynomial of degree p while remaining more efficient in terms of degrees of freedom.

3.2. A posteriori error estimation

The standard a priori error estimate for the exact error given in above section tells us about the rate of convergence which we can anticipate, but is of limited use if we wish to find a numerical estimate of the accuracy. One way in which we might get a realistic estimate or a bound upon the discretization error is to use the computed solution u_h itself in estimating $\|e\|_E$. The idea of using u_h to estimate the error is called *a posteriori error estimation* and some variety of methods to use it have been seen in literature, see [24] and [29] for detailed survey on this topic.

The criterion of what constitutes a good method of using u_h is quantified by the condition of asymptotic exactness of the resulting a posteriori error estimator, introduced by Babuška and Rheinboldt [77].

Definition 3.1 (*Asymptotic Exactness*)**.** Let η be an a posteriori error estimator, then if under reasonable regularity assumptions on u and the data of the problem, and the family of meshes $\mathcal{M}_h$, we get

$$\|e\|_E \approx \{1 + O(h^{\gamma})\}\eta \quad \text{as} \quad h \to 0, \tag{28}$$

where $\gamma > 0$ is independent of h and the constant in the $O(h^{\gamma})$ term depends upon the data of the problem only, then we say that η is an asymptotically exact a posteriori error estimator.

This article is motivated from an error estimate technique developed by Zienkiewicz and Zhu [30] in classical FE methods, where the Superconvergent Patch Recovery [31,32] has proved to be effective and economical both in evaluating errors and driving adaptive mesh refinement. We first design and analyze the Superconvergent Patch Recovery procedure to improve the gradient field $\sigma_h^* := \nabla u_h^*$ for B-splines/NURBS based isogeometric FE methods. Then the improved gradient field ∇u_h^* is used instead of the exact solution ∇u in (25), in theme of Zienkiewicz and Zhu [30], to compute the estimated error by

$$\eta = \|\nabla u_h^* - \nabla u_h\|_{L^2(\Omega)} = \left(\int_{\Omega} (\nabla u_h^* - \nabla u_h)^T \cdot (\nabla u_h^* - \nabla u_h) d\Omega \right)^{1/2}. \tag{29}$$

The quality of the error estimate $\eta = \|\nabla u_h^* - \nabla u_h\|_{L^2(\Omega)}$ is measured by its effectivity index which is given by the ratio of the estimated error to the exact error, i.e.,

$$\theta = \frac{\eta}{\|e\|_E} = \frac{\|\nabla u_h^* - \nabla u_h\|_{L^2(\Omega)}}{\|\nabla u - \nabla u_h\|_{L^2(\Omega)}}. \tag{30}$$

In context of Definition 3.1, the error estimator is said to be asymptotically exact if θ approaches unity as h approaches 0. Notice that the reliability of the estimator is dependent on the quality of the recovered quantity ∇u_h^* obtained through the recovery procedure. The following result from [32] demonstrates how an asymptotically exact error estimator can be achieved.

Theorem 3.2. *Suppose* $\|e^*\|_E = \|\nabla u - \nabla u_h^*\|_{L^2(\Omega)}$ *is the error in the recovered solution, then the error estimator* η *is asymptotically exact if*

$$\frac{\|e^*\|_E}{\|e\|_E} \to 0 \qquad as \qquad \|e\|_E \to 0. \tag{31}$$

Thus, the condition of asymptotic exactness of the error estimator can be achieved if $\|e^*\|_E$ converges at higher rate than $\|e\|_E$. It follows that if $\|e^*\|_E$ is superconvergent, i.e., $\|e^*\|_E = O(h^{p+\alpha})$ with $\alpha > 0$, in comparison to the discretization error $\|e\|_E = O(h^p)$, then asymptotic exactness is assured and we also get

$$1 - O(h^\alpha) \leq \theta \leq 1 + O(h^\alpha). \tag{32}$$

The recovery procedure developed in this article is claimed to be superconvergent of order 1 in case of uniform refinements and of some order $\alpha \in (0, 1]$ for *structured* LR meshes obtained *via* adaptive h-refinement algorithm of LR B-splines as described in Section 2. We have shown numerical results to illustrate the superconvergence behavior of the developed recovery procedures in Section 7.

Remark 3.1. It should be noted that while the higher rate of convergence $\|e^*\|_E = O(h^{p+\alpha})$ with $\alpha > 0$ is needed to show asymptotic exactness, the error estimator will always be practically applicable providing the recovered values are more accurate (though not necessary superconvergent) than those obtained from the computed solution. If for instance **consistently** we have

$$\frac{\|e^*\|_E}{\|e\|_E} \equiv \delta \leq 0.2 \tag{33}$$

then the effectivity index θ will be within the range of [0.8, 1.2].

4. Gradient recovery techniques: Postprocessing

In this section we present different recovery procedures which can be used to improve the computed gradient $\boldsymbol{\sigma}_h := \nabla u_h$, where u_h is the computed FE solution from NURBS (or B-splines, LR B-splines) based isogeometric analysis. An improved gradient $\boldsymbol{\sigma}^* = \nabla u^*$ is obtained in two different ways: (i) global projection over the domain Ω, (ii) local smoothing of the gradient components over small patches of elements. We first describe two global recovery procedures denoted as Continuous L^2 projection (CL2P) and Discrete least square fitting (DLSF), respectively, where the computed gradient components of the solution is projected onto the same NURBS (or B-splines, LR B-splines) space that was used for the computation of u_h in FE approximation (22). Then we extend the original Superconvergent Patch Recovery (SPR) procedure of [31] from FEA to isogeometric analysis. The main idea of SPR was based on the existence of some points with high accuracy, i.e., derivative superconvergent points within each element. The existence and location of such superconvergent points in isogeometric analysis is not known in literature. Thus we decide to use the term sampling points of high accuracy instead of *true* derivative superconvergent points for the SPR procedure described in this section. In Section 5 we will discuss the existence and location of true derivative superconvergent points for one and two dimensional elliptic model problem and finally the computation based on these points is shown in Section 7.

4.1. Global recovery procedures

It is possible to obtain a more accurate gradient of u_h by a *projection* or *variational recovery process*. These approaches are originally due to Oden and Brauchli [78] and Hinton and Campbell [79] and have been used to construct the error estimate in FE stresses [30]. We seek the improved gradient field

$$\boldsymbol{\sigma}^* = \mathbf{R}\hat{\boldsymbol{c}}_\sigma \tag{34}$$

where $\mathbf{R}$ is the matrix corresponding to the functions used in representation of primary solution field and $\hat{\boldsymbol{c}}_\sigma$ is the unknown global vector of *new* control variables.

4.1.1. Continuous L^2-projection (CL2P)

The improved gradient field $\boldsymbol{\sigma}^*$ defined by (34) is obtained by global L^2-projection, where the unknown control variables $\hat{\boldsymbol{c}}_\sigma$ are now determined by forcing a least square fit of $\boldsymbol{\sigma}^*$ to the computed gradient $\boldsymbol{\sigma}_h$. That is, the functional

$$\mathcal{J}(\hat{\boldsymbol{c}}_\sigma) = \int_\Omega (\boldsymbol{\sigma}^* - \boldsymbol{\sigma}_h)^T \cdot (\boldsymbol{\sigma}^* - \boldsymbol{\sigma}_h) d\Omega \tag{35}$$

is minimized with respect to $\hat{\boldsymbol{c}}_\sigma$. The minimization of (35) is carried out by letting

$$\frac{\partial \mathcal{J}}{\partial \hat{\boldsymbol{c}}_\sigma} = 2 \int_\Omega \left(\frac{\partial \boldsymbol{\sigma}^*}{\partial \hat{\boldsymbol{c}}_\sigma} \right)^T \cdot (\boldsymbol{\sigma}^* - \boldsymbol{\sigma}_h) d\Omega = \mathbf{0},$$

with

$$\int_\Omega \mathbf{R}^T \mathbf{R} d\Omega \hat{\boldsymbol{c}}_\sigma = \int_\Omega \mathbf{R}^T \boldsymbol{\sigma}_h d\Omega \quad \text{or} \quad \mathbf{A}\hat{\boldsymbol{c}}_\sigma = \mathbf{B}_\sigma, \tag{36}$$

where

$$\mathbf{A} = \int_\Omega \mathbf{R}^T \mathbf{R} d\Omega \quad \text{and} \quad \mathbf{B}_\sigma = \int_\Omega \mathbf{R}^T \boldsymbol{\sigma}_h d\Omega.$$

The above process is called global L^2 projection because $\boldsymbol{\sigma}^*$ is a field that is obtained by projecting the computed gradient components $\boldsymbol{\sigma}_h$ onto the same function space as used for the computed solution u_h.

The size of global smoothing matrix $\mathbf{A}$ depends on the number of control variables and it has the sparsity pattern as defined by the support of basis functions. In fact, it is similar to the mass matrix used in problems of dynamics. We use here the full Gauss-quadrature points to solve the system (36) and the cost involved in it has therefore the same growth rate as the original equation system for solving u_h.

4.1.2. Discrete least square fitting (DLSF)

The improved gradient field $\boldsymbol{\sigma}^*$ defined by (34) is obtained by global discrete least square fitting, where the unknown control variable $\hat{\boldsymbol{c}}_\sigma$ are now determined by ensuring a least square fit of (34) to the set of derivative superconvergent points or at least high accuracy sampling points existing in each knot element of the considered single patch domain. That is, we minimize

$$\mathcal{H}(\hat{\boldsymbol{c}}_\sigma) = \sum_{k=1}^{N_{total}} \left(\boldsymbol{\sigma}^*(\mathbf{x}_k) - \boldsymbol{\sigma}_h(\mathbf{x}_k) \right)^2, \tag{37}$$

where $\boldsymbol{\sigma}_h$ is the computed gradient and N_{total} is the total number of the optimal sampling points in each patch of the computational domain. By substituting from (34) into (37) it follows

$$\mathcal{H}(\hat{\boldsymbol{c}}_\sigma) = \sum_{k=1}^{N_{total}} \left(\mathbf{R}_k^T \hat{\boldsymbol{c}}_\sigma - \boldsymbol{\sigma}_h(\mathbf{x}_k) \right)^2. \tag{38}$$

The minimization of (38) is carried out by letting

$$\frac{\partial \mathcal{H}}{\partial \hat{\boldsymbol{c}}_\sigma} = 0 \quad \Rightarrow \quad \mathbf{M}\hat{\boldsymbol{c}}_\sigma = \mathbf{F}_\sigma, \tag{39}$$

with

$$\mathbf{M} = \sum_{k=1}^{N_{total}} \mathbf{R}_k^T \mathbf{R}_k, \quad \text{and} \quad \mathbf{F}_\sigma = \sum_{i=1}^{N_{total}} \mathbf{R}_k^T \boldsymbol{\sigma}_h(\mathbf{x}_k).$$

The above process is called discrete least square fitting of the computed gradient components $\boldsymbol{\sigma}_h$ onto the same function space as used for the solution u_h. Now having the new control variables of the improved gradient $\boldsymbol{\sigma}^*$, the related surface can be constructed and the same FE implementation routine can be used for the computation of smooth

gradient values and the error quantities. We define this procedure for a single patch domain. The procedure for computational domain constructed of several multi-patch domains can be defined for each patch separately.

It should be noted that the DLSF procedure proposed in this article will be valid only for C^{p-1} spline or NURBS elements in isogeometric analysis, while in classical C^0-Lagrange finite elements the present DLSF procedure cannot be defined because the total number of optimal sampling points N_{total} needed to perform least square fitting (where either the reduced integration points or Barlow points are chosen) will be less than the total degrees of freedom N_{dim}. However, one can always define a local/global discrete least fitting procedure which will be valid provided it has enough sampling points, in that case the full $(p+1)\times(p+1)$ Gauss quadrature points has to be considered in each element, and such types of smoothing procedures are presented in [79].

4.2. Superconvergent patch recovery (SPR)

The original idea of SPR [31] was to improve the gradient value of the computed FE solution at nodal points. To improve the component of the gradient at a node, an *element patch* is defined that usually consists of all elements to which the node is connected. Now, a polynomial function is defined globally consisting of the monomials used for the basis function of the element at stake. The coefficients of the polynomial are defined such that the polynomial matches the component of the gradient as much as possible at the reduced integration (or the derivative superconvergence) points within the patch (in a least squares sense). Finally, an improved gradient in the node is obtained by evaluating this polynomial. This is done for all gradient components separately.

The SPR procedure in this article has three main steps; (i) Patch recovery procedure, (ii) Element patch configuration, and (iii) Global recovered field representation. In the first step we consider a local least square fitting procedure similar to the original SPR procedure of [31]. The patch element configuration here will differ from the element patch in classical FEM. We form an element patch with respect to the support of each basis function of the solution space as the basis function in isogeometric analysis are not interpolatory in nature. We consider the conjoining of polynomial expansion to get the global representation of the recovered field in the solution space where a weighting argument based on partition of unity of basis functions is used.

4.2.1. Patch recovery procedure

We explain a local smoothing procedure for the improved gradient component

$$\sigma^*_\alpha = \mathbf{P}(\mathbf{x})\mathbf{a}_\alpha \tag{40}$$

where $\mathbf{P}$ is a matrix of monomials, at least of same degree as the solution space, in the Cartesian co-ordinates $\mathbf{x}$ on the patch of elements, and $\mathbf{a}_\alpha$ is the vector of unknown coefficients with $\alpha = x, y$. The coefficients $\mathbf{a}_\alpha$ are then determined from a least square fit of the field σ^*_α to the values of computed σ^h_α at chosen sampling points $\{\mathbf{x}_i\}_i^{n^{elp}_{sp}}$ (for which two choices of PSCP and CSCP are discussed in Sections 5–7) within each element patch, i.e., we minimize the following

$$\mathcal{F}(\mathbf{a}_\alpha) = \sum_{i=1}^{n^{el}_{sp}} (\sigma^*_{\alpha,i} - \sigma^h_{\alpha,i})^T (\sigma^*_{\alpha,i} - \sigma^h_{\alpha,i}). \tag{41}$$

The stationary condition for $\mathcal{F}(\mathbf{a}_\alpha)$ becomes

$$\frac{\partial \mathcal{F}}{\partial \mathbf{a}_\alpha} = 0 \;\Rightarrow\; \mathbf{D}\mathbf{a}_\alpha = \mathbf{G} \;\Rightarrow\; \mathbf{a}_\alpha = \mathbf{D}^{-1}\mathbf{G}, \tag{42}$$

where

$$\mathbf{D} = \sum_{i=1}^{n^{elp}_{sp}} \mathbf{P}_i^T(\mathbf{x}_i)\mathbf{P}_i(\mathbf{x}_i) \quad \text{and} \quad \mathbf{G} = \sum_{i=1}^{n^{elp}_{sp}} \mathbf{P}_i^T(\mathbf{x}_i)\sigma^h_{\alpha,i}.$$

4.2.2. Patch configurations

The patch configuration in isogeometric analysis is motivated from its definition in classical FEM. In FEM, the patch is a collection of elements surrounding a nodal point [31]. Here, we consider a patch with respect to each basis

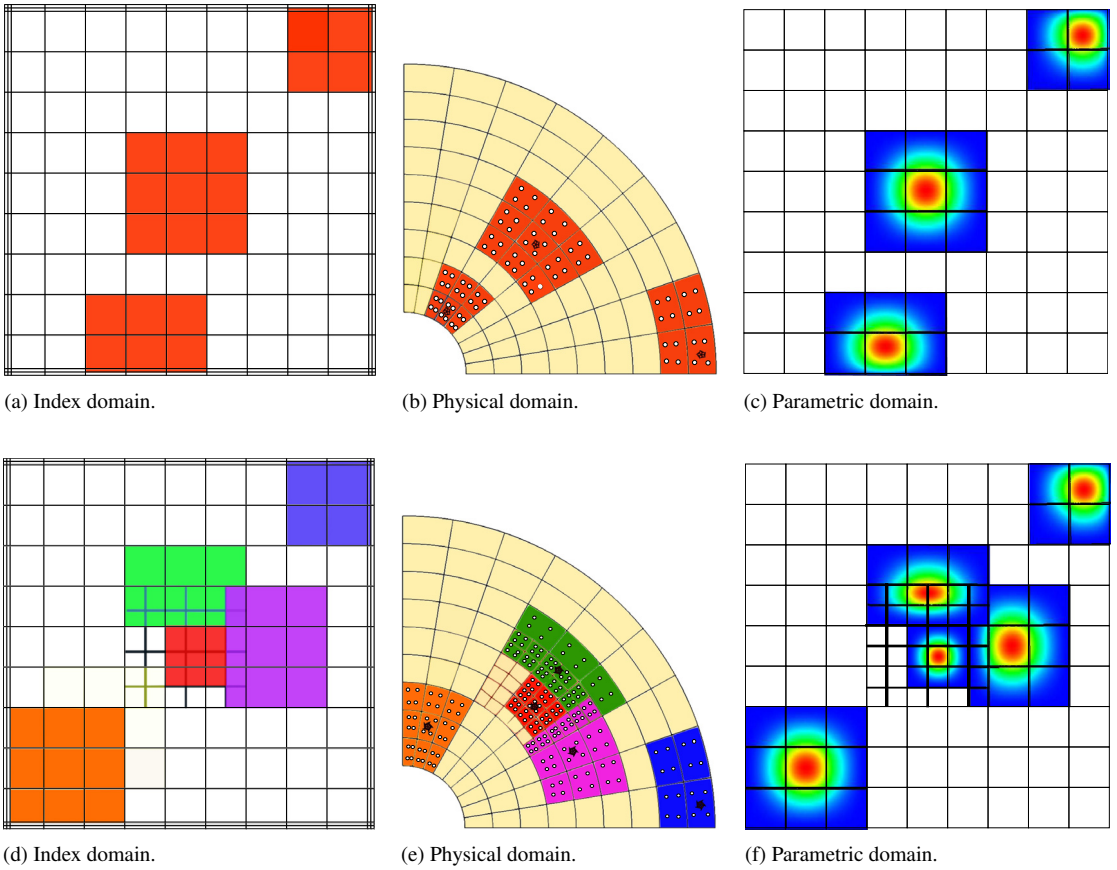

(a) Index domain. (b) Physical domain. (c) Parametric domain.

(d) Index domain. (e) Physical domain. (f) Parametric domain.

Fig. 6. Regular element patches: The element patch formation with respect to the support of quadratic B-Spline/NURBS basis function *first* row represents regular patch for tensor product case, *second* row represents regular patches on general LR mesh (or unstructured mesh), in index domain, physical domain and parametric domain, respectively (from left to right).

function, and it is the collection of elements within the support of that basis function. The general element patch formation with the support of quadratic B-splines/NURBS/LR B-splines is shown in Fig. 6. Similar to FEM, here we also have the concept of boundary element patches as shown in Fig. 7 (first row), which does not contain sufficient number of elements for the local discrete least square fitting procedure. These special cases can be handled with the concept of extending the domain of element patches or by considering the regular patch to do the recovery procedure for that boundary basis function. Herein we choose the approach of using the regular element patch to recover the value for the boundary basis function. The different cases along the boundary are shown in Fig. 7.

4.2.3. Global recovered gradient field

In the SPR-procedure, a linear system is formed on a local patch of elements and then solved for the unknown $\mathbf{a}_\alpha$ in (42). The recovered gradient within the patch of elements is computed by evaluating (40) at the desired location. When the SPR is used for the error estimation, we are interested in recovered values at the element-interior points (i.e., full integration points) to compute the error in certain norms. Since the specific element belongs to more than one patch, the patch recovery does not provide a unique gradient value at such points. In order to construct a global recovered gradient field, Blacker and Belytschko [80] proposed to conjoin the polynomial expansions, $\sigma^* = \mathbf{Pa}$ for all the patches containing the actual element using the basis as a weighting function. Adopting the same approach here, we propose to recover the gradient field at any point $\mathbf{x}$ through

$$\sigma^*(\mathbf{x}) = \sum_{\forall A} \sigma_A^* R_A(\mathbf{x}) \tag{43}$$

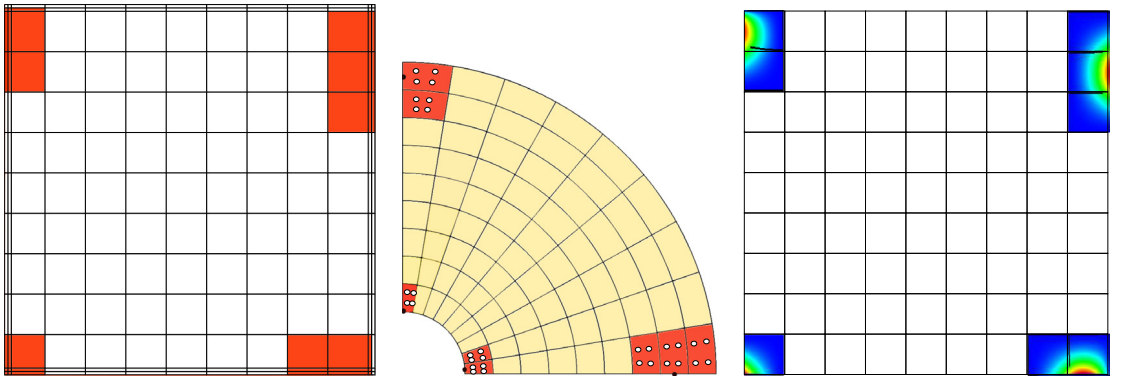

(a) Index domain. (b) Physical domain. (c) Parametric domain.

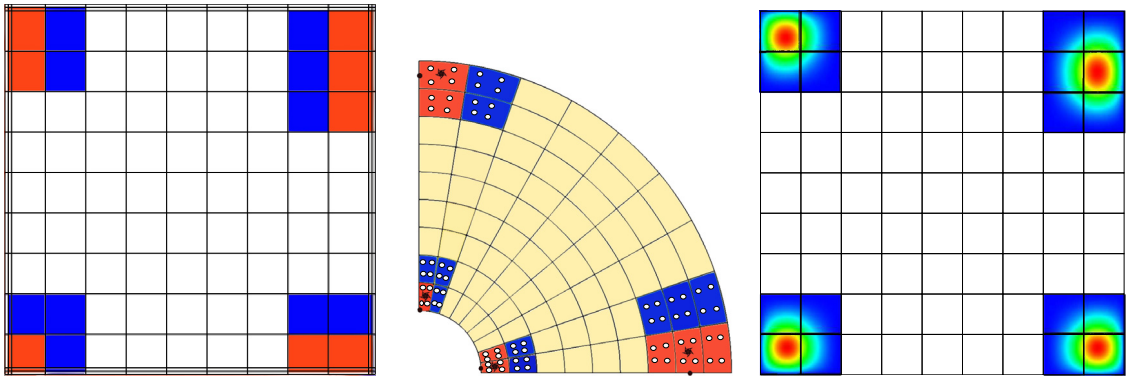

(d) Index domain. (e) Physical domain. (f) Parametric domain.

Fig. 7. Boundary element patches: The element patch formation with respect to the support of quadratic B-Spline/NURBS basis function *first* row represents general boundary patch and *second* row represents extended patch along the boundary of the domain, in index domain, physical domain and parametric domain, respectively (from left to right).

where R_A is the solution basis function and $\sigma_A^*(\mathbf{x})$ is a local recovered gradient field in the form (40) corresponding to the element patch formed with respect to the support of basis function R_A. The partition of unity property is used to assign the proper weighting functions in (43) and the conjoining procedure becomes local and efficient.

5. Local behavior of spline based Galerkin discretization

In this section we first present a motivational study for the existence of natural superconvergence points in spline based Galerkin discretization for one dimensional elliptic model problem. In this context we follow arguments given by Wahlbin in [72], Chapter 1. Later we present a general approach based on local Neumann projection to compute superconvergence points for the computed FE solution using B-splines and LR B-splines for one and two-dimensional model problems.

5.1. Motivational study for the existence of superconvergence points

We consider the following elliptic model problem on the domain $\Omega = (0, 1)$,

$$-\frac{d^2u}{dx^2} = f(x), \quad \text{with} \quad u(0) = u(1) = 0. \tag{44}$$

The weak formulation of (44) is to find $u \in H_0^1(\Omega)$ such that

$$a(u, v) \equiv \int_\Omega \left(\frac{du}{dx}\right)\left(\frac{dv}{dx}\right) dx = \int_\Omega f v dx, \quad \forall\, v \in H_0^1(\Omega). \tag{45}$$

Let $\Omega_h = \{x_i\}_{i=0}^{N}, 0 = x_0 < x_1 < \cdots < x_N = 1$ be the discretized mesh of the domain $\bar{\Omega}$ such that $\Omega_i = (x_i, x_{i+1}), \bar{\Omega} = \cup_{i=0}^{N-1} \bar{\Omega}_i$. Let $\mathcal{S}^p_{\Omega_h,0}$ be the spline space of degree of p with smoothness $0 \leq \mu \leq p-1$ on Ω_h defined by

$$\mathcal{S}^p_{\Omega_h,0} \equiv \{v(x) : v \in C^{\mu}(\Omega) \cap C^0(\overline{\Omega}),\ v|_{\Omega_i} \in \mathbb{P}_p(\Omega_i), v(0) = v(1) = 0\},$$

where $\mathbb{P}_p(\Omega_i)$ denotes the polynomials of degree p on each Ω_i and $\mathcal{S}^p_{\Omega_h,0} \subseteq H^1_0(\Omega)$, since $\mu \geq 0$.

The FE spline based approximation is given as follows: Find $u_h \in \mathcal{S}^p_{\Omega_h,0}$ such that

$$a(u_h, v) = (f, v), \quad \forall\, v \in \mathcal{S}^p_{\Omega_h,0}. \tag{46}$$

Now we define an approximation $\tilde{u}_h$ to u which is the Ritz projection (or elliptic projection for present case) defined as:

Definition 5.1 (*Ritz Projection*)**.** Find $\tilde{u}_h \in \mathcal{S}^p_{\Omega_h,0}$ such that

$$\left(\frac{d}{dx}(u - \tilde{u}_h), \frac{dv}{dx}\right) = 0, \quad \forall\, v \in \mathcal{S}^p_{\Omega_h,0}. \tag{47}$$

Let $\mathcal{S}^{p-1}_{\Omega_h}$ be the spline space of degree $p-1$ with smoothness $\mu - 1$. Now we construct $B_{i,p-1} \in \mathcal{S}^{p-1}_{\Omega_h}$ B-spline basis functions defined over the support $\bar{\mathcal{J}}_i$, where $B_{i,p-1}(x) > 0$ in $\mathcal{J}_i = (x_i, x_{i+k_d})$ with $k_d = [\frac{p}{p-\mu}]^+$ denoting the smallest integer $\geq \frac{p}{p-\mu}$.

Define $\Phi_i(x)$ such that

$$\Phi_i(x) = \int_0^x B_{i,p-1}(y)ds - x\int_0^1 B_{i,p-1}(y)ds$$

which belongs to $\mathcal{S}^p_{\Omega_h,0}$. Then

$$\int_{\mathcal{J}_i} \frac{d}{dx}(u - \tilde{u}_h)B_{i,p-1} = \left(\frac{d}{dx}(u - \tilde{u}_h), \left(\frac{d\Phi_i}{dx} + \int_0^1 B_{i,p-1}\right)\right) = \left(\frac{d}{dx}(u - \tilde{u}_h), \frac{d\Phi_i}{dx}\right) = 0. \tag{48}$$

Since $B_{i,p-1} > 0$ on $\mathcal{J}_i$, then from the above relation (48) we obtain there exists the existence of a point $\hat{\eta}_i \in \mathcal{J}_i$ such that

$$\frac{d}{dx}(u - \tilde{u}_h)(\hat{\eta}_i) = 0. \tag{49}$$

We conclude this result in form of the following theorem, see Theorem 1.4.1 of Wahlbin [72].

Theorem 5.1. *Let $k_d = [\frac{p}{p-\mu}]^+$, and let $\mathcal{J}_i = (x_i, x_{i+k_d})$, for any $i = 0, 1, \ldots, N - k_d$. There exists a point $\hat{\eta}_i \in \mathcal{J}_i$ such that $\frac{d}{dx}(u - \tilde{u}_h)(\hat{\eta}_i) = 0$.*

Similar to the above result for the existence of zeros in the derivative error, a corresponding result for the displacement error is as follows:

Theorem 5.2. *Let $k_u = [\frac{p-1}{p-2-\max(-1,\mu-2)}]^+$ for $p \geq 2$, and let $\mathcal{J}_i = (x_i, x_{i+k_u})$, for any $i = 0, 1, \ldots, N - k_u$. There exists a point $\hat{\xi}_i \in \mathcal{J}_i$ such that $(u - \tilde{u}_h)(\hat{\xi}_i) = 0$.*

Proof. See Theorem 1.4.2 of Wahlbin [72]. □

Eqs. (45)–(47) and the uniqueness of Ritz projection give that $u_h = \tilde{u}_h$. Thus the above two results hold for the FE spline based approximation u_h itself. It should be noted that these results do not give us any information about the exact location of the superconvergence points but they tell us about the existence of such points for spline based Galerkin discretization.

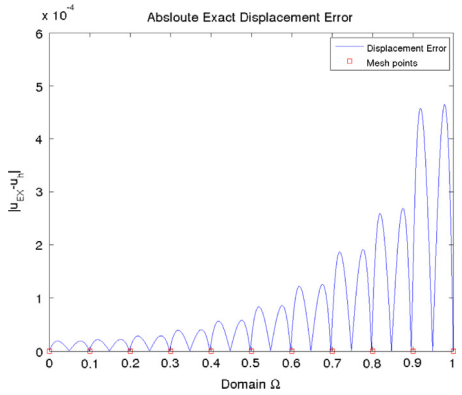

(a) C^1 quadratic B-spline.

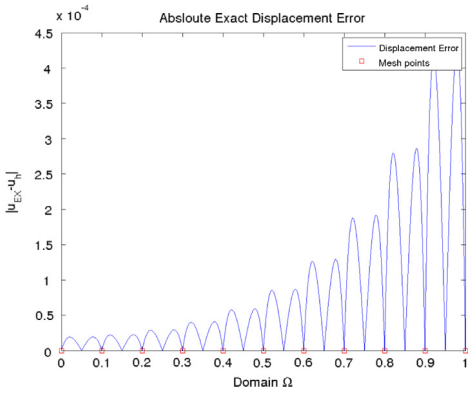

(b) C^0 quadratic Lagrange.

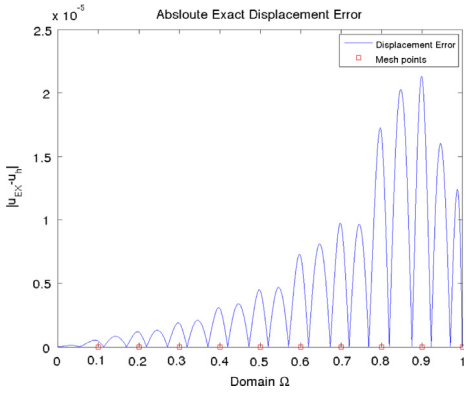

(c) C^2 cubic B-spline.

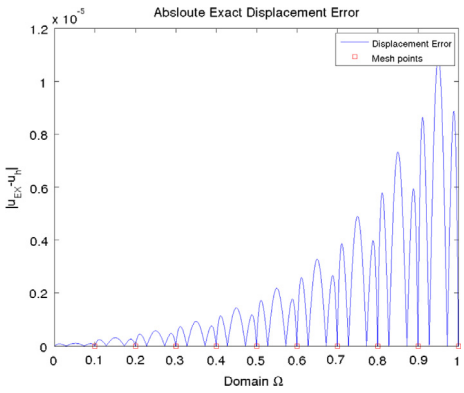

(d) C^0 cubic Lagrange.

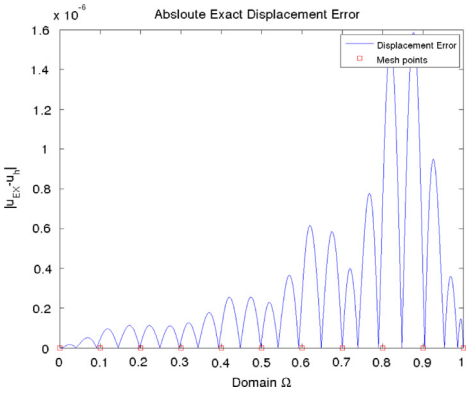

(e) C^3 quartic B-spline.

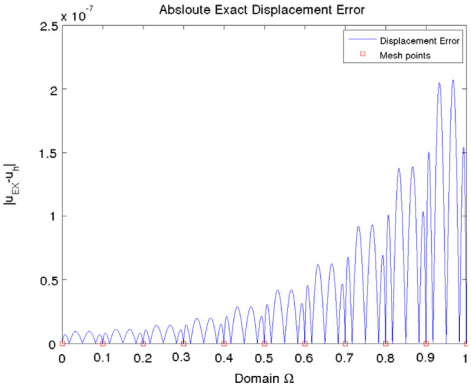

(f) C^0 quartic Lagrange.

Fig. 8. Absolute solution error in Galerkin FE spline discretization using C^{p-1} smooth splines and C^0 Lagrange spaces for degree $p = 2, 3, 4, 5$ with uniform mesh width $h = 1/10$.

Now we consider a numerical example for the problem (44) with a given exact solution $u = x^2 - \frac{\sinh 4x}{\sinh 4}$. Let u_h be the spline based FE approximation obtained by (46). In Figs. 8 and 9, we present the graph of the absolute value of the exact solution error $(u - u_h)(x)$ for $x \in \Omega$ and the derivative error $\frac{d}{dx}(u - u_h)(x)$ for $x \in \Omega$, respectively. It is interesting to note that the absolute solution error and the derivative error have zeros at several points in the domain

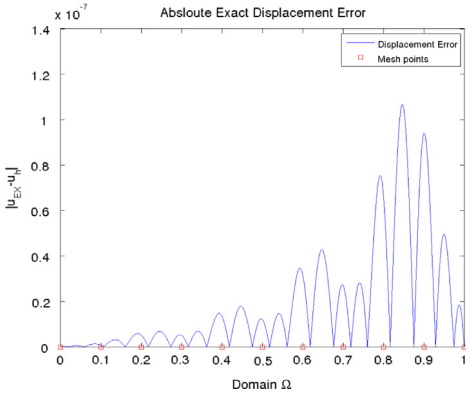

(g) C^4 quintic B-spline.

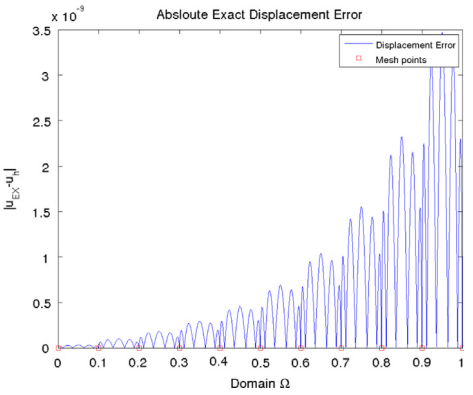

(h) C^0 quintic Lagrange.

Fig. 8. (*continued*)

Table 1
Summary of the superconvergence results for the asymptotic h-Galerkin formulation, see page 21 in Wahlbin [72].

$\mathcal{S}^{\mu,p}_{\Omega_h}$- Spline space	Mesh restriction	Function values	First derivative
$\mu = 0,\ p \geq 1$	Complete general meshes	(i) $O(h^{2p})$ at meshpoints (ii) $O(h^{p+2})$ at zeros of $L'_p(x)$	$O(h^{p+1})$ at zeros of $L_p(x)$
$\mu = 1,\ p$: Even	Meshes uniform in $C_1 h \ln 1/h$ neighborhood of point (similarly away from $\partial\Omega$)	$O(h^{p+2})$ at mesh- and midpoints and at zeros of $L'_p(x)$	$O(h^{p+1})$ at zeros of $L_p(x)$
$\mu = 1,\ p$: Odd	Same restriction as in case $\mu = 1,\ p$: Even	$O(h^{p+2})$ at $p-1$ zeros of $Q(x) = L_{p-1}(x) - \frac{L'_{p-1}(1)}{L'_{p+1}(1)} L_{p+1}(x)$	$O(h^{p+1})$ at mesh- and midpoints, also at $p-3$ zeros of $Q'(x)$
$\mu = 2,\ p = 3$	Same restriction as in case $\mu = 1,\ p$: Even	$O(h^{p+2})$ at two points, zeros of $Q(x) = L_{p-1}(x) - \frac{L'_{p-1}(1)}{L'_{p+1}(1)} L_{p+1}(x)$	$O(h^{p+1})$ mesh and midpoints
$\mu \geq 1,\ p$: Odd	General meshes, symmetry about the point in $C_1 h \ln 1/h$ neighborhood of point (similarly away from $\partial\Omega$)	Not known	$O(h^{p+1})$ at mesh points
$\mu \geq 1,\ p$: Even	Same restriction as $\mu \geq 1,\ p$: Odd	$O(h^{p+2})$ at mesh points	Not known

$\Omega = (0, 1)$ for C^{p-1} spline spaces. For the sake of comparison we also present the case of classical C^0 Lagrange elements as shown in the right column of Figs. 8–9. We notice that the absolute solution error and the derivative error for the Lagrange basis functions also have zeros at several points in the domain $\Omega = (0, 1)$, but the pattern behaves differently than C^{p-1} cases.

In Chapter 1 of Wahlbin [72], the Element Orthogonality Analysis (EOA) approach is presented, i.e., given certain restriction on the mesh distribution (e.g., local symmetry), to compute the location of natural superconvergence points. Table 1 summarizes the superconvergence results for asymptotic h-Galerkin formulation (as $h \to 0$ the superconvergent points for the solution and derivative error converge to the given values in Table 1), see also page 21 of Wahlbin [72]. Here $L_p(x)$ denotes the Legendre polynomial of degree p and $L'_p(x)$ is its first derivative. For the uniform mesh distribution the location of these points can be confirmed from the numerical results shown in Figs. 8 and 9.

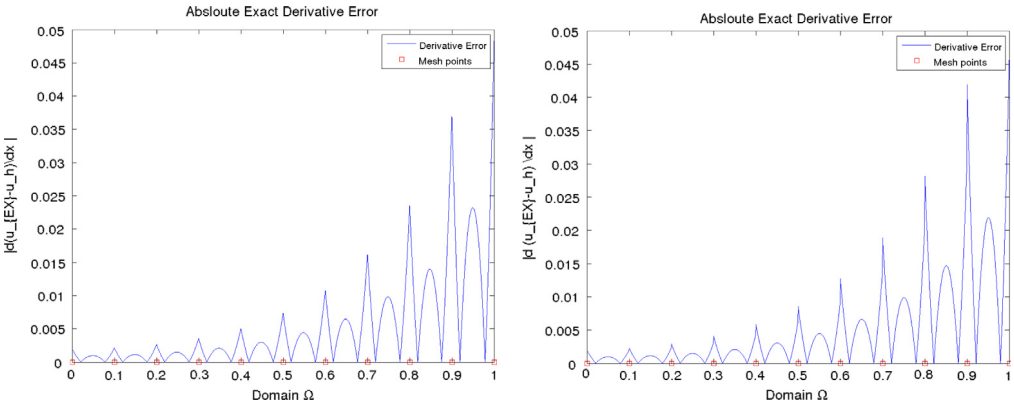

(a) C^1 quadratic B-spline.

(b) C^0 quadratic Lagrange.

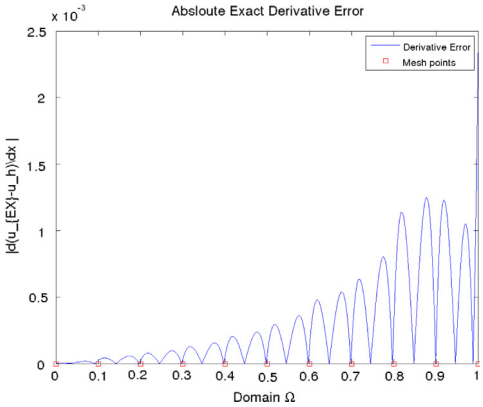

(c) C^2 cubic B-spline.

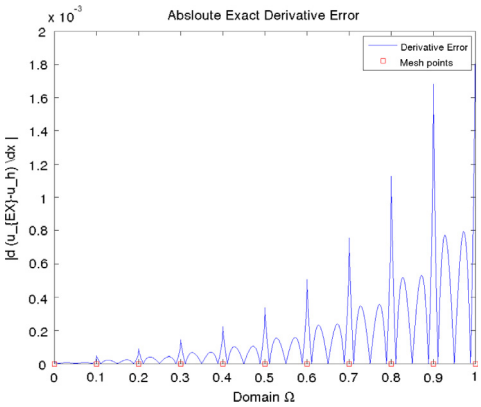

(d) C^0 cubic Lagrange.

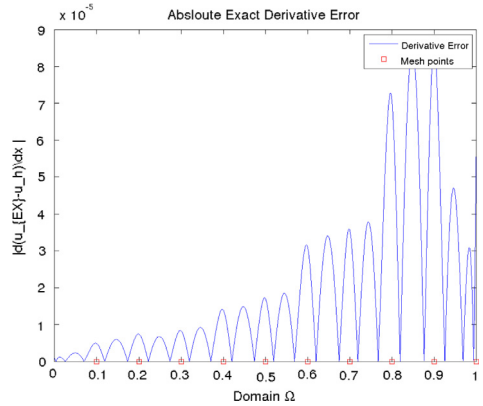

(e) C^3 quartic B-spline.

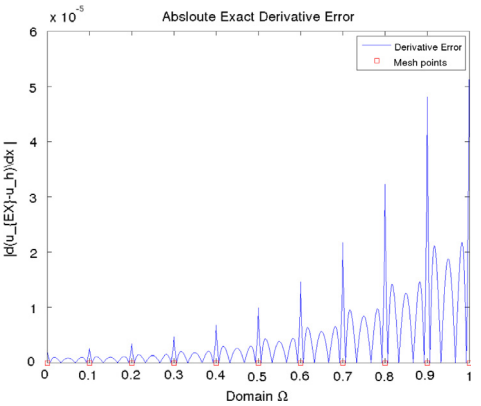

(f) C^0 quartic Lagrange.

Fig. 9. Absolute derivative error in Galerkin FE spline discretization using C^{p-1} smooth splines and C^0 Lagrange spaces for degree $p = 2, 3, 4, 5$ with uniform mesh width $h = 1/10$.

5.2. *Computer based proof of existence of superconvergence points*

Now we present a general approach for analyzing the local behavior of spline based Galerkin discretization. This approach is motivated from setting of computer based proof of existence of superconvergence points of Babuška et al. [69,57,58] and can be used to analyze the superconvergence behavior of isogeometric Galerkin discretization.

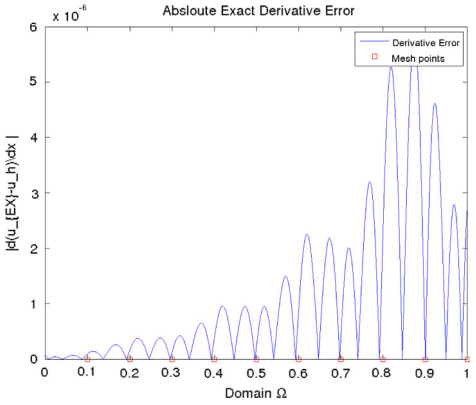

(g) C^4 quintic B-spline.

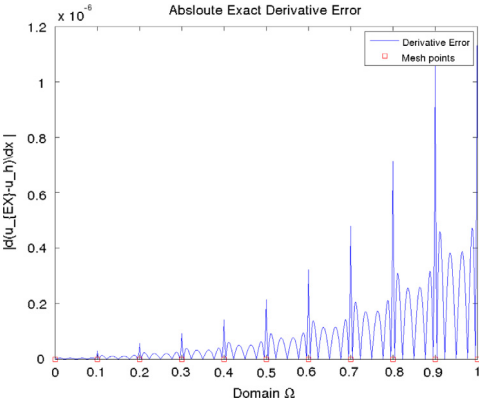

(h) C^0 quintic Lagrange.

Fig. 9. (*continued*)

To be consistent with the earlier work on superconvergence by Babuška and his co-workers, we present the results of this section in similar way as described for classical finite elements in [69]. Here we first explain the basic idea of how to discover and compute the superconvergence points in simple one dimensional setting for function spaces satisfies assumptions as described below. Then we present the idea in two dimensional setting for tensor product spline spaces and LR B-splines, which are the current objects for isogeometric analysis taken in this article. Some numerical tests are performed to illustrate the methodology for computing these superconvergence points.

5.2.1. Computation of superconvergence points for one-dimensional spline spaces

Denote an interval (or subdomain) of size H centered at the point $\bar{x}$ by

$$K(\bar{x}, H) := \left(\bar{x} - \frac{1}{2}H, \bar{x} + \frac{1}{2}H\right). \tag{50}$$

We consider the case of interior mesh elements and assume that:

Assumption 1. Define $K(\bar{x}, H_0)$ and $K(\bar{x}, H_1)$ be two mesh intervals with $H_1 < H_0 \leq H$ coincide exactly with a patch of elements, defined by

$$K(\bar{x}, H_i) := \cup_{j=n_i}^{m_i} \Omega_{h,j}, \quad \forall\ i = 0, 1, \tag{51}$$

where n_i and m_i denotes the indices of the first and last element from the mesh discretization Ω_h which belong to $K(\bar{x}, H_i)$.

Assumption 2. Let the exact solution u satisfy

$$\left\| \frac{d^{p+2}u}{dx^{p+2}} \right\|_{L^\infty(K(\bar{x},H))} \leq \mathcal{C}_1 < \infty \tag{52}$$

and

$$0 < \mathcal{C}_2 \leq \left| \frac{d^{p+1}u(\bar{x})}{dx^{p+1}} \right|. \tag{53}$$

Assumption 3 (*Pollution Under Control*)**.** The meshes Ω_h are such that the error $E = u - u_h$ satisfies

$$\|E\|_{L^2(K(\bar{x},H))} \leq \mathcal{C}h^\beta\sqrt{H} \quad \text{or} \quad \|E\|_{L^\infty(K(\bar{x},H))} \leq \mathcal{C}h^\beta, \tag{54}$$

with

$$\beta \geq (p+1) - \ell, \ \ 0 < \ell < 1, \tag{55}$$

and $\mathcal{C}$ depends on $\mathcal{C}_1$.

In Assumption 1, we consider the sub-domains as $K(\bar{x}, H_1) \subset\subset K(\bar{x}, H) \subset\subset \Omega$, where the distance between the domain boundaries is given by $d = dist(K(\bar{x}, H_1), \partial K(\bar{x}, H))$ with $d \geq c_0 h$. The value of constant $c_0 \geq (p+1)$ depends on the degree of spline spaces to ensure that the domain $K(\bar{x}, H)$ contains at least $p+1$ layer of elements surrounding the domain of interest $K(\bar{x}, H_1)$. Assumption 3 is a general characterization of the case of negligible pollution which applies for general meshes in higher dimensions, as well as in simple one dimensional setting.

We now prove a series of lemmas which lead us to the final result of this section. For this, let $u^{\bar{x},(p+1)}$ be the $(p+1)^{\text{th}}$ degree Taylor series expansion of u centered at $\bar{x}$, defined by,

$$u^{\bar{x},(p+1)} := \sum_{k=0}^{p+1} \frac{1}{k!} \frac{d^k u}{dx^k}(\bar{x})(x-\bar{x})^k. \tag{56}$$

Lemma 5.1. *Let u satisfy Assumption 2, and let $u^{\bar{x},(p+1)}$ be the $(p+1)^{\text{th}}$ degree Taylor series expansion of u centered at $\bar{x}$ defined by (56). Then we have*

$$\left\| \frac{d^r}{dx^r}(u - u^{\bar{x},(p+1)}) \right\|_{L^\infty(K(\bar{x},H_i))} \leq \mathcal{C} H_i^{p+2-r} \tag{57}$$

for $0 \leq r \leq p+2$ with the constant depending on $\mathcal{C}_1$ and p.

Proof. The proof of this lemma can be easily obtained after using integral form of reminder of Taylor expansion with Assumption 2. See also proof of Lemma 4.7.2 from Babuška and Strouboulis [69]. □

Define $\mathcal{S}^p_{\Omega_h}(K(\bar{x}, H))$ the restriction of the spline space $\mathcal{S}^p_{\Omega_h}$ in the patch of elements which belong to $K(\bar{x}, H)$ as

$$\mathcal{S}^p_{\Omega_h}(K(\bar{x}, H)) := \left\{ v \in C^{p-1}(K(\bar{x}, H)) \mid \exists\, w \in \mathcal{S}^p_{\Omega_h} \ : \ v \equiv w|_{K(\bar{x},H)} \right\}. \tag{58}$$

Let $U^{\bar{x},H}_{\mathcal{S}^p_{\Omega_h}}$ be the Neumann projection of $u^{\bar{x},(p+1)}$ into the spline space $\mathcal{S}^p_{\Omega_h}(K(\bar{x}, H))$ which is defined as follows:

Definition 5.2 (*Local Neumann Projection in 1D*)**.** Find $U^{\bar{x},H}_{\mathcal{S}^p_{\Omega_h}} \in \mathcal{S}^p_{\Omega_h}(K(\bar{x}, H))$ such that

$$\mathcal{A}_{K(\bar{x},H)}(u^{\bar{x},(p+1)} - U^{\bar{x},H}_{\mathcal{S}^p_{\Omega_h}}, v) = 0 \quad \forall \ v \in \mathcal{S}^p_{\Omega_h}(K(\bar{x}, H)), \tag{59}$$

with

$$\int_{K(\bar{x},H)} (u^{\bar{x},(p+1)} - U^{\bar{x},H}_{\mathcal{S}^p_{\Omega_h}}) = 0, \tag{60}$$

where the bilinear form is defined by $\mathcal{A}_{K(\bar{x},H)}(u, v) = \int_{K(\bar{x},H)} \frac{du}{dx}\frac{dv}{dx}$.

Note that $U^{\bar{x},H}_{\mathcal{S}^p_{\Omega_h}}$ exists and is uniquely determined from (59) to (60). The above defined local Neumann projection is very important in the analysis of the error distribution such as determining the contribution of local and global errors as well as locating the superconvergence points. Neumann projection based idea also has a general significance as it can be simply extended to higher dimension cases.

Let $Q^{\bar{x},p+1}_{EX}$ be the last term of Taylor expansion defined in (56), we have

$$Q^{\bar{x},p+1}_{EX} = \frac{1}{(p+1)!} \frac{d^{(p+1)}}{dx^{(p+1)}}(u)(\bar{x})(x-\bar{x})^{(p+1)} \tag{61}$$

and let $Q^{\bar{x},H}_{\mathcal{S}^p_{\Omega_h}} \in \mathcal{S}^p_{\Omega_h}(K(\bar{x}, H))$ be its Neumann $\mathcal{A}$-projection defined by (59)–(60).

Lemma 5.2. *Under Assumption 2, we have*

$$\left\| \frac{d}{dx}(u^{\bar{x},(p+1)} - U^{\bar{x},H}_{\mathcal{S}^p_{\Omega_h}}) \right\|_{L^2(K(\bar{x},H))} = \left\| \frac{d}{dx}(Q^{\bar{x},(p+1)}_{EX} - Q^{\bar{x},H}_{\mathcal{S}^p_{\Omega_h}}) \right\|_{L^2(K(\bar{x},H))} \leq \mathcal{C} h^p \sqrt{H} \tag{62}$$

and

$$\left\|(u^{\bar{x},(p+1)} - U^{\bar{x},H}_{\mathcal{S}^p_{\Omega_h}})\right\|_{L^2(K(\bar{x},H))} = \left\|(Q^{\bar{x},(p+1)}_{EX} - Q^{\bar{x},H}_{\mathcal{S}^p_{\Omega_h}})\right\|_{L^2(K(\bar{x},H))} \leq Ch^{p+1}\sqrt{H}. \tag{63}$$

Proof. Note that $u^{\bar{x},p} \in \mathbb{P}_p \subseteq \mathcal{S}^p_{\Omega_h}$, we get

$$u^{\bar{x},(p+1)} - U^{\bar{x},H}_{\mathcal{S}^p_{\Omega_h}} \equiv Q^{\bar{x},(p+1)}_{EX} - Q^{\bar{x},H}_{\mathcal{S}^p_{\Omega_h}}. \tag{64}$$

By the construction of the Neumann projection in (59)–(60), we obtain that $U^{\bar{x},H}_{\mathcal{S}^p_{\Omega_h}}$ satisfies the orthogonality condition

$$\int_{K(\bar{x},H)} \left(\frac{d}{dx}(u^{\bar{x},(p+1)} - U^{\bar{x},H}_{\mathcal{S}^p_{\Omega_h}})\right)\left(\frac{dv}{dx}\right) = 0 \quad \forall\, v \in \mathcal{S}^p_{\Omega_h}(K(\bar{x},H)). \tag{65}$$

It follows that $\frac{d}{dx}(U^{\bar{x},H}_{\mathcal{S}^p_{\Omega_h}})$ is the best approximation of $\frac{d}{dx}(u^{\bar{x},(p+1)})$ from $\mathcal{S}^{p-1}_{\Omega_h}(K(\bar{x},H))$ in the L^2-norm, and hence

$$\begin{aligned}\left\|\frac{d}{dx}(u^{\bar{x},(p+1)} - U^{\bar{x},H}_{\mathcal{S}^p_{\Omega_h}})\right\|_{L^2(K(\bar{x},H))} &\leq Ch^p \left\|\frac{d^{p+1}}{dx^{p+1}}(u^{\bar{x},(p+1)})\right\|_{L^2(K(\bar{x},H))} \\ &\leq Ch^p\sqrt{H}\left\|\frac{d^{p+1}}{dx^{p+1}}(u^{\bar{x},(p+1)})\right\|_{L^\infty(K(\bar{x},H))}.\end{aligned} \tag{66}$$

Thus, it follows from Assumption 2 that we obtain the result given in (62).

Now after employing the standard Aubin and Nitsche trick we have

$$\left\|(u^{\bar{x},(p+1)} - U^{\bar{x},H}_{\mathcal{S}^p_{\Omega_h}})\right\|_{L^2(K(\bar{x},H))} \leq Ch\left\|\frac{d}{dx}(u^{\bar{x},(p+1)} - U^{\bar{x},H}_{\mathcal{S}^p_{\Omega_h}})\right\|_{L^2(K(\bar{x},H))} \tag{67}$$

On combining the results from (62) and (67) we obtain the required result (63). □

Next we aim to establish a relationship between the discretization error $u - u_h$ and the error in the Neumann projection of its asymptotic expansion, i.e., $u^{\bar{x},(p+1)} - U^{\bar{x},H}_{\mathcal{S}^p_{\Omega_h}}$ on some interior elements patch $K(\bar{x},H_1)$, with $H_1 < H$ as defined in Assumption 1.

Assume that we have a spline FE approximation $u_h \in \mathcal{S}^p_{\Omega_h}(K(\bar{x},H))$ to u which is sufficiently smooth in $K(\bar{x},H)$, cf. Assumption 2, such that

$$\left(\frac{d}{dx}(u-u_h), \frac{dv}{dx}\right) = 0, \quad \forall v \in \mathcal{S}^{p,comp}_{\Omega_h}(K(\bar{x},H)), \tag{68}$$

where $\mathcal{S}^{p,comp}_{\Omega_h}(K(\bar{x},H))$ denotes the restriction of the basis functions in $\mathcal{S}^p_{\Omega_h}$ with *compact support* in the interior of $K(\bar{x},H)$.

Further, we can write

$$u - u_h = u^{\bar{x},(p+1)} - U^{\bar{x},H}_{\mathcal{S}^p_{\Omega_h}} + \left((u - u^{\bar{x},(p+1)}) - (u_h - U^{\bar{x},H}_{\mathcal{S}^p_{\Omega_h}})\right). \tag{69}$$

On differentiating (69), we get

$$\frac{d}{dx}(u-u_h) = \frac{d}{dx}(u^{\bar{x},(p+1)} - U^{\bar{x},H}_{\mathcal{S}^p_{\Omega_h}}) + \left(\frac{d}{dx}((u - u^{\bar{x},(p+1)}) - (u_h - U^{\bar{x},H}_{\mathcal{S}^p_{\Omega_h}}))\right). \tag{70}$$

Now on the interval $K(\bar{x},H_1)$, where $H_1 < H_0 \leq H$, we write

$$\frac{d}{dx}(u-u_h)(x) = \underbrace{\frac{d}{dx}(u^{\bar{x},(p+1)} - U^{\bar{x},H}_{\mathcal{S}^p_{\Omega_h}})(x)}_{(I)} + \underbrace{\frac{d}{dx}((u - u^{\bar{x},(p+1)}) - (u_h - U^{\bar{x},H}_{\mathcal{S}^p_{\Omega_h}}))(x)}_{(II)}, \quad \text{for } x \in K(\bar{x},H_1). \tag{71}$$

To obtain the bound on the (II)-term of (71), we notice that from (59) and (68) we have

$$\left(\frac{d}{dx}((u-u^{\bar{x},(p+1)})-(u_h-U^{\bar{x},H}_{\mathcal{S}^p_{\Omega_h}})),\frac{dv}{dx}\right)=0,\quad \forall v\in\mathcal{S}^{p,comp}_{\Omega_h}(K(\bar{x},H)). \tag{72}$$

For the problem stated in (72), we now apply the interior error estimate result from Theorem 1.2 of Schatz and Wahlbin [81]. Here we consider this result as a proposition by assuming that all the assumptions of Theorem 1.2 of [81] will be satisfied and that the result also holds for the spline spaces. Thus we obtain

$$\begin{aligned}\|(u-u^{\bar{x},(p+1)})-(u_h-U^{\bar{x},H}_{\mathcal{S}^p_{\Omega_h}})\|_{W^1_\infty(K(\bar{x},H_1))}&\le C\min_{v\in\mathcal{S}^p_{\Omega_h}(K(\bar{x},H))}(\|(u-u^{\bar{x},(p+1)})-v\|_{W^1_\infty(K(\bar{x},H))}\\&+H^{-1}\|(u-u^{\bar{x},(p+1)})-v\|_{L_\infty(S(\bar{x},H))})+CH^{-3/2}\|(u-u^{\bar{x},(p+1)})-(u_h-U^{\bar{x},H}_{\mathcal{S}^p_{\Omega_h}})\|_{L^2(K(\bar{x},H))}.\end{aligned} \tag{73}$$

Using for v the spline quasi-interpolant of $u-u^{\bar{x},(p+1)}$ into $\mathcal{S}^p_{\Omega_h}(K(\bar{x},H))$ (Theorem 6.18, [82]), and Lemma 5.1, we get

$$\|(u-u^{\bar{x},(p+1)})-v\|_{W^1_\infty(K(\bar{x},H))}\le Ch^p\|u-u^{\bar{x},(p+1)}\|_{W^{p+1}_\infty(K(\bar{x},H))}\le Ch^pH. \tag{74}$$

Similarly, we get

$$H^{-1}\|(u-u^{\bar{x},(p+1)})-v\|_{L_\infty(K(\bar{x},H))}\le Ch^{p+1}\le Ch^pH. \tag{75}$$

Using (74) and (75) in (73), we get

$$\begin{aligned}\|(u-u^{\bar{x},(p+1)})-(u_h-U^{\bar{x},H}_{\mathcal{S}^p_{\Omega_h}})\|_{W^1_\infty(K(\bar{x},H_1))}&\le Ch^pH\\&+CH^{-3/2}\|(u-u^{\bar{x},(p+1)})-(u_h-U^{\bar{x},H}_{\mathcal{S}^p_{\Omega_h}})\|_{L^2(K(\bar{x},H))}.\end{aligned} \tag{76}$$

After using Assumption 3 with the results of Lemma 5.2, we obtain

$$\begin{aligned}&H^{-3/2}\|(u-u^{\bar{x},(p+1)})-(u_h-U^{\bar{x},H}_{\mathcal{S}^p_{\Omega_h}})\|_{L^2(K(\bar{x},H))}\\&\le H^{-3/2}\left(\|(u-u_h)\|_{L^2(K(\bar{x},H))}+\|u^{\bar{x},(p+1)}-U^{\bar{x},H}_{\mathcal{S}^p_{\Omega_h}}\|_{L^2(K(\bar{x},H))}\right)\\&\le CH^{-1}h^{p+1-\ell}.\end{aligned} \tag{77}$$

On combining (76) and (77), we obtain

$$\|(u-u^{\bar{x},(p+1)})-(u_h-U^{\bar{x},H}_{\mathcal{S}^p_{\Omega_h}})\|_{W^1_\infty(K(\bar{x},H_1))}\le C(h^pH+h^{p+1-\ell}H^{-1}), \tag{78}$$

which gives

$$\left\|\frac{d}{dx}\left((u-u^{\bar{x},(p+1)})-(u_h-U^{\bar{x},H}_{\mathcal{S}^p_{\Omega_h}})\right)\right\|_{L^\infty(K(\bar{x},H_1))}\le C(h^pH+h^{p+1-\ell}H^{-1}). \tag{79}$$

Now by defining $H=Ch^\delta$ we get

$$\begin{aligned}\left\|\frac{d}{dx}\left((u-u^{\bar{x},(p+1)})-(u_h-U^{\bar{x},H}_{\mathcal{S}^p_{\Omega_h}})\right)\right\|_{L^\infty(K(\bar{x},H_1))}&\le C(h^{p+\delta}+h^{p+1-\ell-\delta})\\&\le Ch^{p+\min\{\delta,1-\ell-\delta\}}.\end{aligned} \tag{80}$$

Letting $\vartheta=\min\{\delta,1-\ell-\delta\}$, where $\vartheta>0$ provided $\ell+\delta<1$, this gives

$$\left\|\frac{d}{dx}\left((u-u^{\bar{x},(p+1)})-(u_h-U^{\bar{x},H}_{\mathcal{S}^p_{\Omega_h}})\right)\right\|_{L^\infty(K(\bar{x},H_1))}\le Ch^{p+\vartheta}. \tag{81}$$

Now suppose we can find a point $\hat{\eta}_i \in K(\bar{x}, H_1)$ such that

$$\frac{d}{dx}(u^{\bar{x},(p+1)} - U^{\bar{x},H}_{\mathcal{S}^p_{\Omega_h}})(\hat{\eta}_i) = 0.$$

Then from (71) and (81) we obtain the exact derivative error at point $\hat{\eta}_i$ will be of order $O(h^{p+\vartheta})$, i.e., derivative superconvergence of order ϑ.

Remark 5.1. Note that $u^{\bar{x},p} \in \mathbb{P}_p \subseteq \mathcal{S}^p_{\Omega_h}$ gives

$$u^{\bar{x},(p+1)} - U^{\bar{x},H}_{\mathcal{S}^p_{\Omega_h}} \equiv Q^{\bar{x},(p+1)}_{EX} - Q^{\bar{x},H}_{\mathcal{S}^p_{\Omega_h}}. \tag{82}$$

Thus to get the derivative superconvergence points from the results (71) and (81), we need to find the zeros of

$$\frac{d}{dx}(Q^{\bar{x},(p+1)}_{EX} - Q^{\bar{x},H}_{\mathcal{S}^p_{\Omega_h}})(\hat{\eta}_i) = 0, \text{ for } \hat{\eta}_i \in K(\bar{x}, H_1), \text{ where } H_1 < H_0 \leq H. \tag{83}$$

Further, the definition of $Q^{\bar{x},(p+1)}_{EX}$ in (61) reduces the problem (83) to find the zero for a single monomial $M(x) = (x - \bar{x})^{(p+1)}$ for the spline approximation space $\mathcal{S}^p_{\Omega_h}$ of degree p.

Remark 5.2. In (73), we used the interior error estimate results from Theorem 1.2 of Schatz and Wahlbin [81], by assuming that all the assumptions of Theorem 1.2 of [81] will be satisfied and the results became true for the spline element case here. The interior error estimate in (73) shows that the error in an interior domain $K(\bar{x}, H_1)$ can be estimated with the best order of accuracy that is possible locally for the subspaces used plus the error in a weaker norm over a slightly larger domain which measures the effects from outside of the domain $K(\bar{x}, H_1)$. The constant C in (73) depends on the constants in the set of axioms satisfied by the approximation subspaces over the domain $K(\bar{x}, H)$. For more details about the set of assumptions need to satisfy by spline elements here and the interior estimate (73), see [81].

Now we present two cases to show how to compute the derivative superconvergence points using the idea developed in this section. We consider the one-dimensional Poisson problem with Dirichlet boundary condition on the domain $\Omega = (0, 1)$ with the exact solution $u(x) = \sin(\pi x/2)$.

Example with uniform mesh distribution

We denote u_h the FE spline based approximation of u in $\mathcal{S}^p_{\Omega_h}$, i.e., B-splines of degree p on uniform mesh with $h = 1/8$. In Fig. 10(a), we present the graph of $\frac{d}{dx}(u - u_h)(x)$ for $x \in \bar{\Omega}$. It is interesting to note that $\frac{d}{dx}(u - u_h)(x)$ is zero at several points in the domain Ω. It is clear from the result (83) within Remark 5.1 that the superconvergence points for $\frac{d}{dx}(u - u_h)$ in the interior domain $K(\bar{x}, H_1) = (x_j, x_{j+1}) \subset\subset \Omega$ are the roots of $\frac{d}{dx}(W - W_h)$ in $K(\bar{x}, H_1)$, where W_h is the Neumann projection of monomial $W = (x - \bar{x})^3$, with $\bar{x} = (x_j + x_{j+1})/2$ on B-spline subspace $\mathcal{S}^p_{\Omega_h}(K(\bar{x}, H))$ of $\mathcal{S}^p_{\Omega_h}$ as defined by (59)–(60). In Fig. 10(b), we present the graph of $|\frac{d}{dx}(u - u_h)(x)|$ and $|\frac{d}{dx}(W - W_h)(x)|$ for $x \in (3/8, 4/8)$ using quadratic B-spline space on uniform mesh $h = 1/8$. In this case we have considered $K(\bar{x}, H)$ the larger domain to compute the Neumann projection with $\bar{x} = 9/16$ and $H = 7/16$. We also show the derivative superconvergence points x_i^*s (red circle) where the derivative error $|\frac{d}{dx}(u - u_h)(x_i^*)|$, $i = 1, 2$ is much smaller than the $\max_{\forall x} |\frac{d}{dx}(u - u_h)|$ for $x \in (3/8, 4/8)$ (one interval view) in Fig. 10(c). From this case the computation shows that the two Gauss–Legendre points will be the true derivative superconvergence points on that element. Using this procedure, we compute the superconvergent points for the solution and derivative for B-splines with polynomial degree $p = 1, \ldots, 8$ and summarized our results in Tables 2 and 3, respectively. Our results presented in Tables 2–3 also confirm the location of superconvergence points on uniform meshes presented in Table 1 of [5].

Example with non-uniform mesh distribution

Now to distinguish with the earlier case we consider a non-uniform mesh Ω_h and compute the superconvergence points on a larger interior domain than a single interval. We consider to compute the derivative superconvergence points for $\frac{d}{dx}(u - u_h)$ on a larger interior domain $K(\bar{x}, H_1) = (x_{j-2}, x_{j+1}) \subset\subset \Omega$ via finding the zeros of $\frac{d}{dx}(W - W_h)$ in (x_{j-2}, x_{j+1}), where W_h is the Neumann projection of monomial $W = (x - \bar{x})^3$, with $\bar{x} = (x_{j-2} + x_{j+1})/2$ on

Table 2
Computed solution superconvergent points for spline based Galerkin approximation of degree p on interval $[-1,\ 1]$.

$p=1$	$p=2$	$p=3$	$p=4$	$p=5$	$p=6$	$p=7$	$p=8$
-1	-1	-0.5193296223592281	-1	-0.5049185675126533	-1	-0.503221894597504	-1
1	0	0.5193296223592281	0	0.5049185675126533	0	0.503221894597504	0
	1		1		1		1

Table 3
Computed derivative superconvergent points for spline based Galerkin approximation of degree p on interval $[-1,\ 1]$.

$p=1$	$p=2$	$p=3$	$p=4$	$p=5$	$p=6$	$p=7$	$p=8$
0	-0.5773502691896257	-1	-0.5193296223592281	-1	-0.5049185675126533	-1	-0.503221894597504
	0.5773502691896257	0	0.5193296223592281	0	0.5049185675126533	0	0.503221894597504
		1		1		1	

spline subspace $\mathcal{S}^p_{\Omega_h}(K(\bar{x}, H))$ of $\mathcal{S}^p_{\Omega_h}$ as defined by (59)–(60). Here the domain Ω is discretized with non-uniform mesh with spacing $h_1 = 1/16$ at the left half and spacing $h_2 = 1/8$ in right half of the domain. In Fig. 11, we present the graph of $\frac{d}{dx}(u - u_h)(x)$ for $x \in \Omega$ and $|\frac{d}{dx}(W - W_h)(x)|$ for $x \in (6/16, 5/8)$ using quadratic B-spline space on given non-uniform mesh. In this case we have considered $K(\bar{x}, H)$ the larger domain to compute the Neumann projection with $\bar{x} = 1/2$ and $H = 7/16$. We also show the derivative superconvergence points x_i^*s (red circle) where the exact derivative error $|\frac{d}{dx}(u-u_h)(x_i^*)|,\ i = 1, 2$ is much smaller than the $\max_{\forall x} |\frac{d}{dx}(u-u_h)|$ for $x \in (7/16, 1/2)$ (one interval view) in Fig. 11(c). This case shows that the local mesh topology will play a role in exact location of these derivative superconvergent points for spline spaces, where the points for the middle element in Fig. 11(c) are now shifted from their known location of 2-Gauss Legendre points for uniform mesh partition case.

Extension up to the boundary

The results of this section were based on the assumption that $K(\bar{x}, H)$ is an interior patch of elements. We now generalize them for patches $K(\bar{x}, H)$ which extend up to the boundary, see also [52,69]. We consider the case of left boundary of the domain and assume that all the Assumptions 1–3 hold for $\bar{x} = x_L$ the left boundary point of the domain Ω. We then have

$$\frac{d}{dx}(u - u_h)(x) = \frac{d}{dx}(u^{\bar{x},(p+1)} - U^{\bar{x},H}_{\mathcal{S}^p_{\Omega_h}})(x) + \phi^{x_L,h} + Ch^{p+\vartheta}, \tag{84}$$

where $\phi^{x_L,h} \in \mathcal{S}^p_{\Omega_h}(K(x_L, H))$ such that $u_h + \phi^{x_L,h}$ satisfies the boundary conditions at $x = x_L$, and

$$\mathcal{A}_{K(x_L,H)}(\phi^{x_L,h}, v_h) = 0, \quad \forall\ v_h \in \mathcal{S}^p_{\Omega_h}(K(x_L, H)) \tag{85}$$

and

$$\lim_{x\to H} \frac{d}{dx}(\phi^{x_L,h}(x)) = 0. \tag{86}$$

It is clear that $\phi^{x_L,h}$ is the boundary layer correction and (86) as the decay condition. In some special cases: (i) homogeneous Dirichlet boundary condition, $u(x_L) = 0$, $\phi^{x_L,h}$ must satisfy the Dirichlet boundary condition

$$\phi^{L,h}(x_L) = -(u^{x_L,(p+1)} - U^{x_L,H}_{\mathcal{S}^p_{\Omega_h}})(x_L). \tag{87}$$

(ii) homogeneous Neumann boundary condition, $\frac{du}{dx}(x_L) = 0$, $\phi^{x_L,h}$ must satisfy

$$\mathcal{A}_{K(x_L,H)}(\phi^{x_L,h}, \phi_0^h) = -\mathcal{A}_{K(x_L,H)}(u^{x_L,(p+1)} - U^{x_L,H}_{\mathcal{S}^p_{\Omega_h}}, \phi_0^h) = 0, \tag{88}$$

where ϕ_0^h is the basis function for the node x_0^h. The right hand side vanish identically because of the definition of Neumann projection.

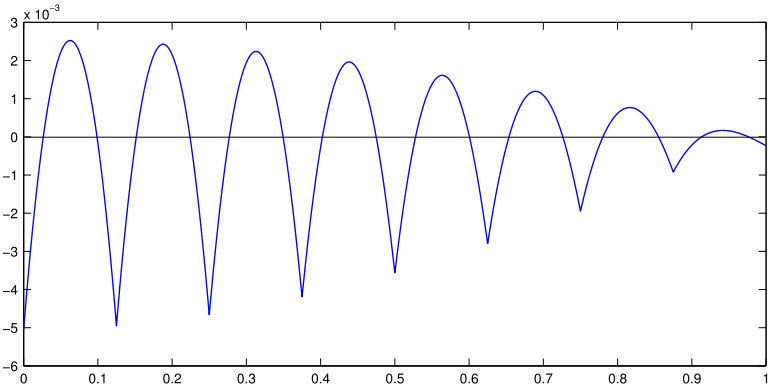

(a) $\frac{d}{dx}(u-u_h)(x)$ for $x \in \Omega = (0,1)$.

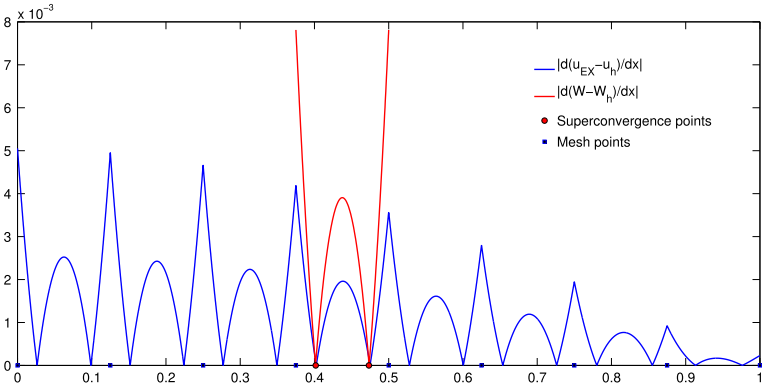

(b) $|\frac{d}{dx}(u-u_h)(x)|$ for $x \in (0,1)$ and $|\frac{d}{dx}(W-W_h)(x)|$ on $x \in (3/8, 4/8)$.

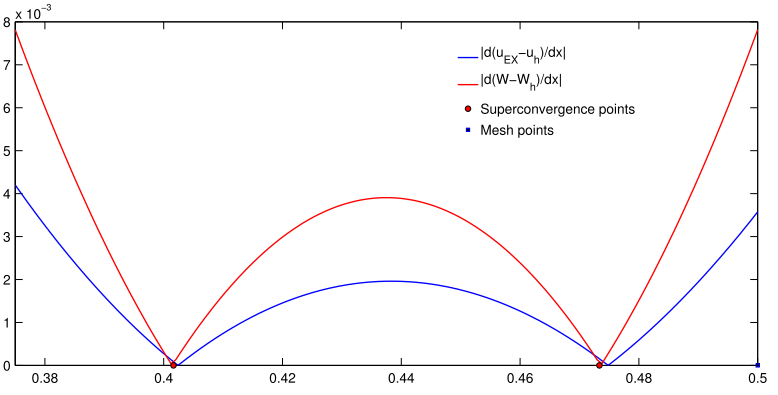

(c) On $\Omega_4 = (3/8, 4/8)$.

Fig. 10. Exact solution on uniform mesh: (a) Graph of $\frac{d}{dx}(u-u_h)(x)$ for $x \in (0,1)$ using quadratic B-spline space on uniform mesh $h = 1/8$ (b) Graph of $|\frac{d}{dx}(u-u_h)(x)|$ for $x \in (0,1)$ and $|\frac{d}{dx}(W-W_h)(x)|$ for $x \in (3/8, 4/8)$ using quadratic B-spline space on uniform mesh $h = 1/8$ (c) the element view $(3/8, 4/8)$.

In both the above cases, we have

$$\phi^{x_L,h} \equiv constant. \tag{89}$$

Hence there is no boundary layer correction term in case of the one-dimensional model problem.

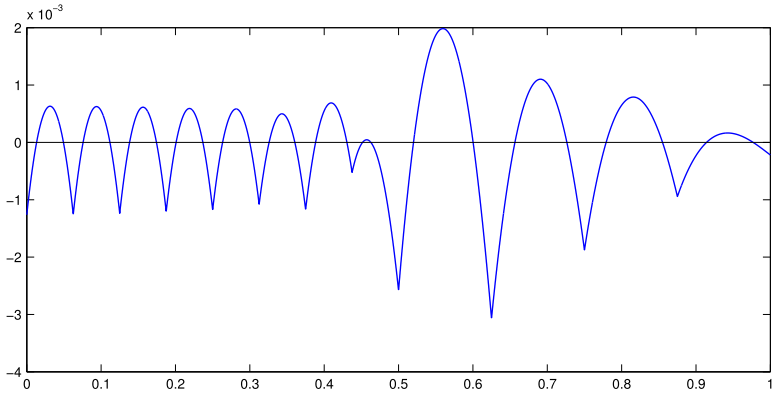

(a) $\frac{d}{dx}(u-u_h)(x)$ for $x \in \Omega = (0,1)$.

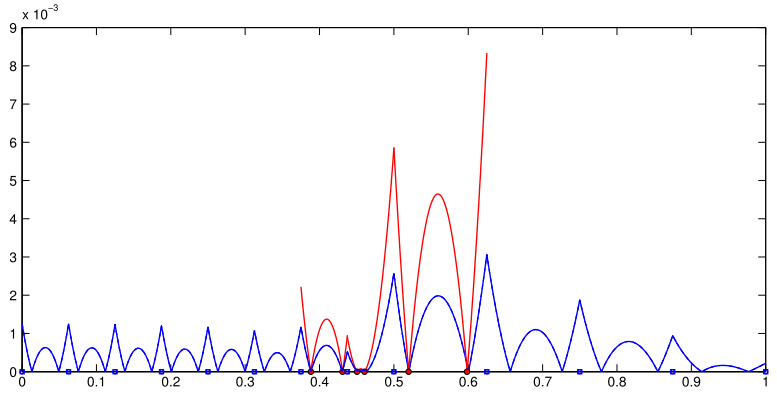

(b) $|\frac{d}{dx}(u-u_h)(x)|$ (blue color) and $|\frac{d}{dx}(W-W_h)(x)|$ on $x \in \Omega_{sub} \equiv \Omega_7 \cup \Omega_8 \cup \Omega_9 = (6/16, 5/8)$ (red color).

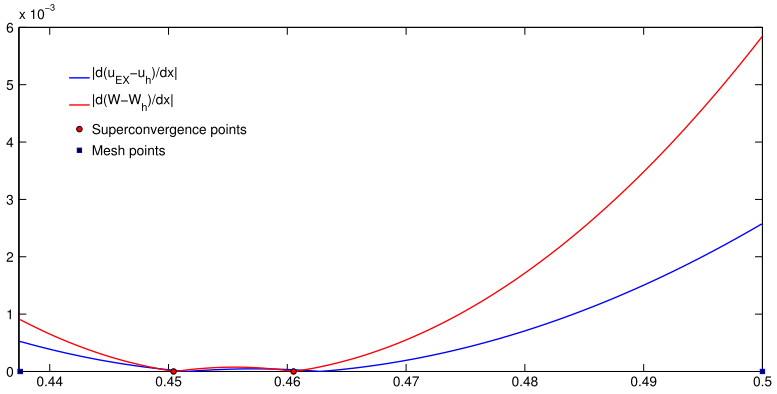

(c) On $\Omega_8 = (7/16, 1/2)$.

Fig. 11. Exact solution on non-uniform mesh: (a) Graph of $\frac{d}{dx}(u-u_h)(x)$ for $x \in (0,1)$ using quadratic B-spline space on non-uniform mesh (b) Graph of $|\frac{d}{dx}(u-u_h)(x)|$ for $x \in (0,1)$ and $|\frac{d}{dx}(W-W_h)(x)|$ for $x \in (6/16, 5/8)$ using quadratic B-spline space on non-uniform mesh (c) the element view $x \in (7/16, 1/2)$. (For interpretation of the references to color in this figure legend, the reader is referred to the web version of this article.)

Remark 5.3. As we have seen above, in the considered model problem $\phi^{x_L,h}$ is constant, and the superconvergence points for the interior elements are valid up to the boundary. However this is not the case, in general, for higher dimensions.

5.2.2. Computation of superconvergence points for tensor product spline spaces

Now we describe the methodology for two dimensional spline spaces. We will make the following assumptions. Denote the subdomain of size H centered at the point $\bar{\mathbf{x}}$ by

$$K(\bar{\mathbf{x}}, H) := \left(\bar{x}_1 - \frac{1}{2}H, \bar{x}_1 + \frac{1}{2}H\right) \times \left(\bar{x}_2 - \frac{1}{2}H, \bar{x}_2 + \frac{1}{2}H\right). \tag{90}$$

We consider the case of interior mesh elements and assume that:

Assumption I. Define $K(\bar{\mathbf{x}}, H_0)$ and $K(\bar{\mathbf{x}}, H_1)$ be two subdomains with $H_1 < H_0 \leq H$ coincide exactly with a patch of elements, namely

$$K(\bar{\mathbf{x}}, H_i) := \cup_{(k_i,l_i)\in I} \Delta_{h,(k_i,l_i)}, \quad \forall\ i = 0, 1, \tag{91}$$

where I is a set of indices which enumerates the cells which belongs in $K(\bar{\mathbf{x}}, H_i)$. Here we assume that H converges to zero with a slower rate than h, namely

$$\mathcal{C}_1 h^\delta \leq H \leq \mathcal{C}_2 h^\delta, \quad 0 < \delta < 1. \tag{92}$$

Assumption II. Let the exact solution u satisfy

$$\max_{0\leq i,j\leq p+2, i+j=p+2} \left\| \frac{\partial^{p+2} u}{\partial x_1^i \partial x_2^j} \right\|_{L^\infty(K(\bar{\mathbf{x}},H))} \leq \mathcal{C} < \infty \tag{93}$$

and

$$0 < \mathcal{C}_0 \leq \sum_{0\leq i,j\leq p+1, i+j=p+1} \left| \frac{\partial^{p+1} u}{\partial x_1^i \partial x_2^j}(\bar{\mathbf{x}}) \right|. \tag{94}$$

Assumption III (*Pollution Under Control*)**.** The meshes Ω_h are such that the error $E = u - u_h$ satisfies

$$\|E\|_{L^2(K(\bar{\mathbf{x}},H))} \leq \mathcal{C} h^\beta \sqrt{H} \quad \text{or} \quad \|E\|_{L^\infty(K(\bar{\mathbf{x}},H))} \leq \mathcal{C} h^\beta \tag{95}$$

with

$$\beta \geq (p+1) - \ell, \ \ 0 < \ell < 1. \tag{96}$$

Let us now describe the two dimensional analogue of the approach presented in 1D case. We will employ the $(p+1)^{\text{th}}$ degree Taylor series expansion of u at $\bar{\mathbf{x}}$, namely,

$$u = u^{\bar{\mathbf{x}},p} + Q_{EX}^{\bar{\mathbf{x}},(p+1)} + R_{EX}^{\bar{\mathbf{x}},(p+1)} \tag{97}$$

where

$$Q_{EX}^{\bar{\mathbf{x}},k} := \sum_{0\leq i,j\leq k, i+j=k} \frac{1}{i!j!} \frac{\partial^k u}{\partial x_1^i \partial x_2^j}(\bar{\mathbf{x}})(x_1 - \bar{x}_1)^i (x_2 - \bar{x}_2)^j \tag{98}$$

and

$$u^{\bar{\mathbf{x}},p} := \sum_{k=0}^{p} Q_{EX}^{\bar{\mathbf{x}},k} \tag{99}$$

and $R_{EX}^{\bar{\mathbf{x}},(p+1)}$ is the remainder. We will also let

$$Q_{(i,j)}^{\bar{\mathbf{x}},(p+1)} := (x_1 - \bar{x}_1)^i (x_2 - \bar{x}_2)^j, \quad \text{where } 0 \leq i, j \leq p+1, i+j = p+1. \tag{100}$$

Neumann Projection in 2D: Define $\mathcal{S}^p_{\Omega_h}(K(\bar{\mathbf{x}}, H))$ the restriction of the spline space $\mathcal{S}^p_{\Omega_h}$ in the patch of elements which belong to $K(\bar{\mathbf{x}}, H)$ as

$$\mathcal{S}^p_{\Omega_h}(K(\bar{x}, H)) := \left\{ v \in C^{p-1,p-1}(K(\bar{\mathbf{x}}, H)) \mid \exists\, w \in \mathcal{S}^p_{\Omega_h} \ : \ v \equiv w|_{K(\bar{\mathbf{x}}, H)} \right\}. \tag{101}$$

Let $U^{\bar{\mathbf{x}},H}_{\mathcal{S}^p_{\Omega_h}}$ be the Neumann projection of $u^{\bar{\mathbf{x}},(p+1)}$ into the spline space $\mathcal{S}^p_{\Omega_h}(K(\bar{\mathbf{x}}, H))$ as the solution of following discrete problem: find $U^{\bar{\mathbf{x}},H}_{\mathcal{S}^p_{\Omega_h}} \in \mathcal{S}^p_{\Omega_h}(K(\bar{\mathbf{x}}, H))$ such that

$$\mathcal{A}_{S(\bar{\mathbf{x}},H)}((u^{\bar{\mathbf{x}},(p+1)} - U^{\bar{\mathbf{x}},H}_{\mathcal{S}^p_{\Omega_h}}), v) = 0 \quad \forall \ v \in \mathcal{S}^p_{\Omega_h}(K(\bar{\mathbf{x}}, H)), \tag{102}$$

with

$$\int_{K(\bar{\mathbf{x}},H)} (u^{\bar{\mathbf{x}},(p+1)} - U^{\bar{\mathbf{x}},H}_{\mathcal{S}^p_{\Omega_h}}) = 0, \tag{103}$$

where the bilinear form is defined by $\mathcal{A}_{K(\bar{\mathbf{x}},H)}(u, v) = \int_{K(\bar{\mathbf{x}},H)} \nabla u \cdot \nabla v \, d\Omega$. Note that $U^{\bar{x},H}_{\mathcal{S}^p_{\Omega_h}}$ exists, and is uniquely determined from (102) to (103).

Now assume that we have a basic FE approximation $u_h \in \mathcal{S}^p_{\Omega_h}(K(\bar{\mathbf{x}}, H))$ to the function u which is sufficiently smooth in $K(\bar{\mathbf{x}}, H)$, cf. Assumption II, such that

$$(\nabla(u - u_h), \nabla v) = 0, \quad \forall v \in \mathcal{S}^{p,comp}_{\Omega_h}(K(\bar{\mathbf{x}}, H)), \tag{104}$$

where $\mathcal{S}^{p,comp}_{\Omega_h}(K(\bar{\mathbf{x}}, H))$ denotes the restrictions of the functions in $\mathcal{S}^p_{\Omega_h}$ with *compact support* in the interior of $K(\bar{\mathbf{x}}, H)$.

Analogous to the 1D case, we can write

$$u - u_h = u^{\bar{\mathbf{x}},(p+1)} - U^{\bar{\mathbf{x}},H}_{\mathcal{S}^p_{\Omega_h}} + \left((u - u^{\bar{\mathbf{x}},(p+1)}) - (u_h - U^{\bar{\mathbf{x}},H}_{\mathcal{S}^p_{\Omega_h}}) \right). \tag{105}$$

On differentiating (105), we get

$$\frac{\partial}{\partial x_i}(u - u_h) = \frac{\partial}{\partial x_i}(u^{\bar{\mathbf{x}},(p+1)} - U^{\bar{\mathbf{x}},H}_{\mathcal{S}^p_{\Omega_h}}) + \frac{\partial}{\partial x_i}\left((u - u^{\bar{\mathbf{x}},(p+1)}) - (u_h - U^{\bar{\mathbf{x}},H}_{\mathcal{S}^p_{\Omega_h}}) \right), \text{for } i = 1, 2. \tag{106}$$

Now using (102), (103) and (104) with the similar arguments of 1D analysis, we can obtain an analogue results in 2D which is stated as follows:

Theorem 5.3. *Under Assumptions I–III, for all $\delta \in (0, 1)$ such that $C_1 h^\delta \le H \le C_2 h^\delta$, and*

$$\max_{i=1,2} \left\| \frac{\partial}{\partial x_i}(u - u_h) - \frac{\partial}{\partial x_i}(u^{\bar{\mathbf{x}},(p+1)} - U^{\bar{\mathbf{x}},H}_{\mathcal{S}^p_{\Omega_h}}) \right\|_{L^\infty(K(\bar{\mathbf{x}},\gamma H))} \le C h^{p+\nu} \tag{107}$$

where $K(\bar{\mathbf{x}}, \gamma H)$ is an interior subdomain with $0 < \gamma < 1$

Proof. The proof follows analogous steps as in 1D case. □

The above result can also be written as, for each components $i = 1, 2$;

$$\frac{\partial}{\partial x_i}(u - u_h)(\eta) = \frac{\partial}{\partial x_i}(u^{\bar{\mathbf{x}},(p+1)} - U^{\bar{\mathbf{x}},H}_{\mathcal{S}^p_{\Omega_h}})(\eta) + R_i(\eta), \quad \text{for } \eta \in K(\bar{\mathbf{x}}, \gamma H) \tag{108}$$

where $\|R_i(x)\|_{L^\infty(K(\bar{\mathbf{x}},\gamma H))} \le C h^{p+\nu}$.

For nonhomogeneous case e.g. Poisson equation

Note that $u^{\bar{\mathbf{x}},(p)} \in \mathbb{P}_p \subseteq \mathcal{S}^p_{\Omega_h}$, i.e., the FE approximation is able to reproduce exactly all polynomial of degree p, which is true in case of (bi-p) tensor product space with quadrilaterals, this gives

$$u^{\bar{\mathbf{x}},(p+1)} - U^{\bar{\mathbf{x}},H}_{\mathcal{S}^p_{\Omega_h}} \equiv Q^{\bar{\mathbf{x}},(p+1)}_{EX} - Q^{\bar{x},H}_{\mathcal{S}^p_{\Omega_h}}. \tag{109}$$

Thus to get the derivative superconvergence points from the results (108), we need to find the **common** zeros of

$$\frac{\partial}{\partial x_i}(Q_{EX}^{\bar{x},(p+1)} - Q_{\mathcal{S}_{\Omega_h}^p}^{\bar{x},H})(\eta) = 0, \quad \forall\, \eta \in K(\bar{x}, \gamma H), 0 < \gamma < 1, \text{ for } i = 1, 2. \tag{110}$$

Further, for the tensor product spline approximation space $\mathcal{S}_{\Omega_h}^p$ in 2D, the definition of $Q_{EX}^{\bar{x},(p+1)}$ in (98) reduces the problem (110) to find the zeros only for the case of two monomials

$$Q_1(\mathbf{x}) = (x_1 - \bar{x}_1)^{(p+1)} \quad \text{and} \quad Q_2(\mathbf{x}) = (x_2 - \bar{x}_2)^{(p+1)}.$$

For homogeneous case e.g. the Laplace equation

The number of monomials to find the zeros in (108) is further reduced for the case of the Laplace equation, in this case $f = 0$, where it is known a priori that u satisfies the isotropic Laplacian $\Delta u = 0$. In this case we have,

$$Q_{EX}^{\bar{\mathbf{x}},(p+1)} = \frac{1}{(p+1)!}\frac{\partial^{p+1}}{\partial x_1^{p+1}}(u)(\bar{\mathbf{x}})Q_{1,hom}^{\bar{\mathbf{x}},(p+1)} + B(u)(\bar{\mathbf{x}})Q_{2,hom}^{\bar{\mathbf{x}},(p+1)} \tag{111}$$

where

$$B(u)(\bar{\mathbf{x}}) = \begin{cases} \dfrac{1}{(p+1)!}\dfrac{\partial^{p+1}u}{\partial x_1^p \partial x_2}(\bar{\mathbf{x}}), & \text{if } p \text{ is even} \\ (-1)^{(p-1)/2}\dfrac{1}{(p+1)!}\dfrac{\partial^{p+1}u}{\partial x_2^{p+1}}(\bar{\mathbf{x}}), & \text{if } p \text{ is odd} \end{cases} \tag{112}$$

and

$$Q_{1,hom}^{\bar{\mathbf{x}},(p+1)}(x_1, x_2) = \text{Re}\,((z - \bar{z})^k), \quad Q_{2,hom}^{\bar{\mathbf{x}},(p+1)}(x_1, x_2) = \text{Im}\,((z - \bar{z})^k)$$

are the harmonic monomials of degree $(p+1)$ centered at $\bar{\mathbf{x}}$, where $z = x_1 + ix_2$ and $\bar{z} = \bar{x}_1 + i\bar{x}_2$.

For $p = 1$, we obtain

$$Q_{1,hom}^{\bar{\mathbf{x}},(2)}(x_1, x_2) = (x_1 - \bar{x}_1)^2 - (x_2 - \bar{x}_2)^2, \qquad Q_{2,hom}^{\bar{\mathbf{x}},(2)}(x_1, x_2) = (x_1 - \bar{x}_1)(x_2 - \bar{x}_2),$$

while $p = 2$,

$$Q_{1,hom}^{\bar{\mathbf{x}},(3)}(x_1, x_2) = (x_1 - \bar{x}_1)^3 - 3(x_1 - \bar{x}_1)(x_2 - \bar{x}_2)^2,$$
$$Q_{2,hom}^{\bar{\mathbf{x}},(3)}(x_1, x_2) = -(x_2 - \bar{x}_2)^3 + 3(x_1 - \bar{x}_1)^2(x_2 - \bar{x}_2)$$

and $p = 3$ we obtain

$$Q_{1,hom}^{\bar{\mathbf{x}},(4)}(x_1, x_2) = (x_1 - \bar{x}_1)^4 + (x_2 - \bar{x}_2)^4 - 6(x_1 - \bar{x}_1)^2(x_2 - \bar{x}_2)^2,$$
$$Q_{2,hom}^{\bar{\mathbf{x}},(4)}(x_1, x_2) = (x_1 - \bar{x}_1)^3(x_2 - \bar{x}_2) - (x_1 - \bar{x}_1)(x_2 - \bar{x}_2)^3.$$

Thus for the tensor product (bi-p) spline spaces in 2D the problem of finding the zeros (110) will reduce only to these two polynomials $Q_{i,hom}^{\bar{\mathbf{x}},(p+1)}$, $i = 1, 2$.

Uniform mesh partitions

To find the derivative superconvergence points for the Poisson problem in 2D, we first consider the case of tensor product spline approximation space $\mathcal{S}_{\Omega_h}^p$ with uniform mesh distribution. The computed derivative superconvergence points are obtained by finding the common zeros of the derivatives of the difference between the monomials $\{Q_1, Q_2\}$ and its Neumann projections, where the monomials are defined as

$$Q_1(\mathbf{x}) = (x_1 - \bar{x}_1)^{(p+1)} \quad \text{and} \quad Q_2(\mathbf{x}) = (x_2 - \bar{x}_2)^{(p+1)}.$$

In Fig. 12, we consider the case with respect to quadratic splines with $p = 2$. The local subdomain $K(\xi, H)$ to compute the Neumann projection for each monomials and the element of interest $K(\xi, h)$ to compute derivative superconvergence points are shown in Fig. 12(a). The blue lines and red lines within the element of interest shown

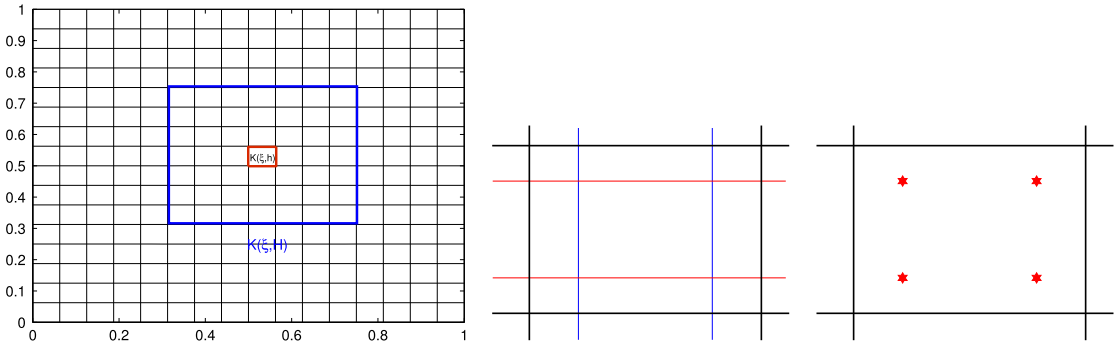

(a) Computational domain. (b) Zeros of derivatives. (c) Derivative Sup. pts.

Fig. 12. Tensor product case with uniform mesh partition: (a) Computational domain for an element $(K(\xi, h))$ and subdomain $K(\xi, H)$ for Neumann projection with quadratic B-spline tensor product mesh with uniform spacing $h = 1/16$; (b) Zeros of the derivatives for $Q_1(x)$ and $Q_2(x)$; (c) Derivative superconvergence points at element level: (2×2)-Gauss Legendre points.

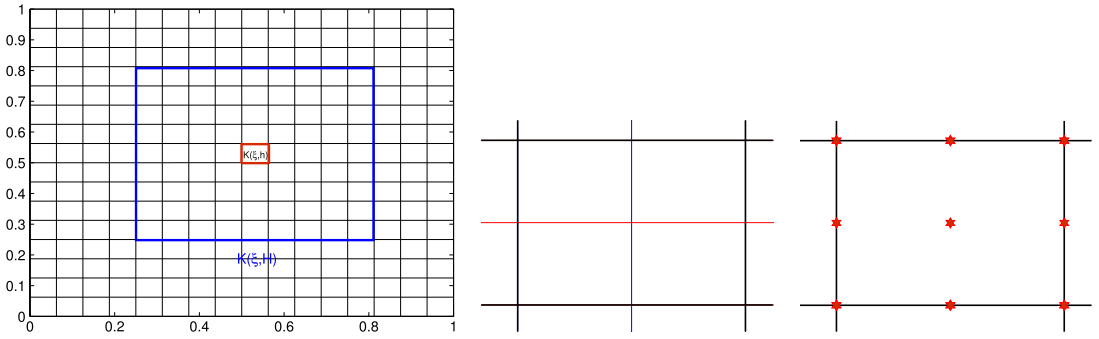

(a) Computational domain. (b) Zeros of derivatives. (c) Derivative Sup. pts.

Fig. 13. Tensor product case with uniform mesh partition: (a) Computational domain for an element $(K(\xi, h))$ and subdomain $K(\xi, H)$ for Neumann projection with cubic B-spline tensor product mesh with uniform spacing $h = 1/16$; (b) Zeros of the derivatives for $Q_1(x)$ and $Q_2(x)$; (c) Derivative superconvergence points at element level: (3×3)-Gauss Lobatto points.

in Fig. 12(b) are the Gauss-lines and they represent the location of derivative zeros with respect to $Q_1(x)$ and $Q_2(x)$ monomials, respectively. The common zeros of these lines, as (2×2)-Gauss Legendre points, are shown in Fig. 12(c) which will be the derivative superconvergence points for tensor product quadratic spline spaces. Similar to the quadratic case, in Fig. 13 we compute the location of computed derivative superconvergence points for tensor product cubic spline spaces, which will be the (3×3)-Gauss Lobatto points. Using the same methodology the derivative superconvergence points at the element level for the case of C^0-quadratic splines, C^0-cubic splines and C^1-cubic splines are shown in Fig. 14. The C^0-quadratic splines represent the case of classical Lagrange elements and (2×2)-Gauss points will be the derivative superconvergence points within each elements, while C^1-cubic splines share the same location of derivative superconvergence points within each elements as does C^2-cubic splines. For C^0-cubic splines we obtain the (3×3)-Gauss Legendre points as derivative superconvergence points within each elements.

Non-uniform mesh partitions

For the tensor product case in 2D, we can also compute the location of derivative superconvergence points by computing the location of points in the univariate case for each direction separately. In Fig. 15(a) we consider a case with respect to tensor product spline approximation space $\mathcal{S}^2_{\Omega_h}$ in 2D with non-uniform mesh distribution, here the mesh interface lines are shown in dark black lines. We discuss different cases arising by enforcing the C^0 or C^1 continuity along mesh interface lines for C^0 and C^1 quadratic spline spaces. In Fig. 15(b) we show the location of computed derivative superconvergence points for C^0-quadratic splines using the Neumann projection in 2D. We obtain the same results by using the Neumann projection for univariate case in each directions and then taking the tensor product of those points. The results for C^1-quadratic splines with C^1 and C^0-continuity lines along mesh

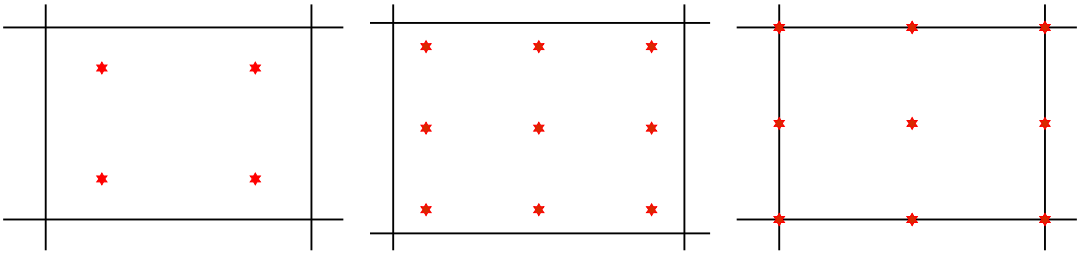

(a) C^0-quadratic spline. (b) C^0-cubic spline. (c) C^1-cubic spline.

Fig. 14. Derivative superconvergence points for tensor product case with uniform mesh partition: (a) C^0-quadratic spline: (2×2)-Gauss Legendre points; (b) C^0-cubic spline: (3×3)-Gauss Legendre points; (c) C^1-cubic spline: (3×3)-Gauss Lobatto points.

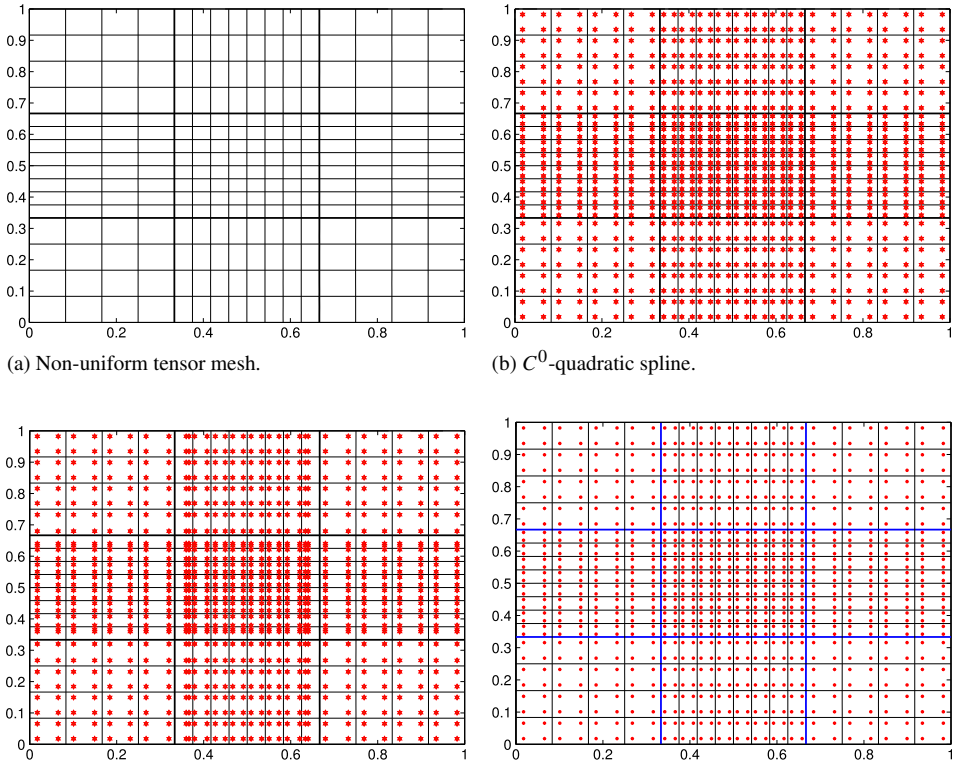

(a) Non-uniform tensor mesh. (b) C^0-quadratic spline.

(c) C^1-quadratic spline. (d) C^1-quadratic spline with C^0 interface line.

Fig. 15. Derivative superconvergence points for quadratic tensor product case with non-uniform mesh partition: (a) non-uniform mesh tensor mesh; (b) C^0-quadratic spline; (b) C^1-quadratic spline; (d) C^1-quadratic spline with C^0 interface line (in blue color). (For interpretation of the references to color in this figure legend, the reader is referred to the web version of this article.)

interface lines are shown in Fig. 15(c) and Fig. 15(d), respectively. When there is C^1 continuity along the interface lines, there will be a shift towards the fine meshes while for the case of C^0 continuity along the interface the derivative superconvergence points will remain at (2×2)-Gauss Legendre points as the case with C^0-quadratic splines. The results for tensor product spline approximation space $\mathcal{S}^p_{\Omega_h}$ of degree three with non-uniform mesh distribution, with different cases arises by enforcing the C^0, C^1 and C^2 continuity along mesh interface lines for C^0, C^1 and C^2 cubic splines are shown in Fig. 16. Due to the presence of C^0 continuity lines along the mesh interfaces and C^{-1} lines along the boundary for C^2-cubic spline case as shown in Fig. 16(d), the derivative points in immediate neighborhood

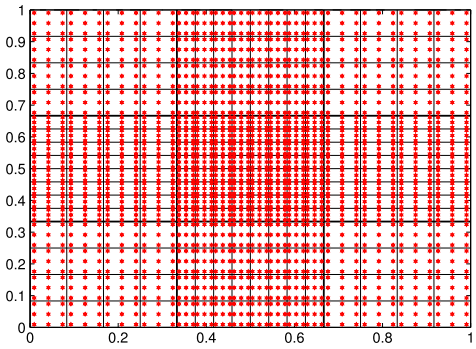

(a) C^0-cubic spline.

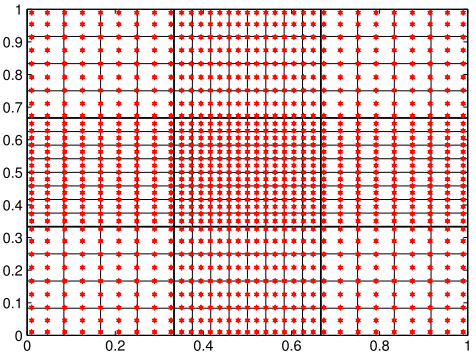

(b) C^1-cubic spline.

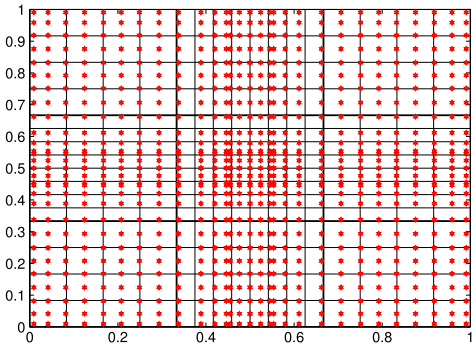

(c) C^2-cubic spline.

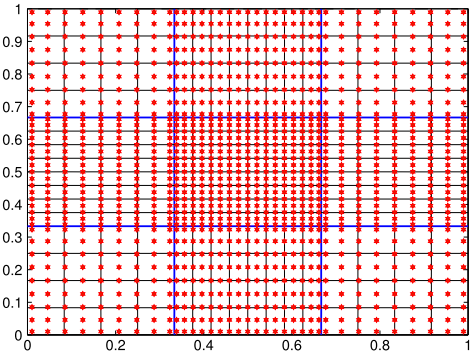

(d) C^1-cubic spline with C^0 interface line (in blue color).

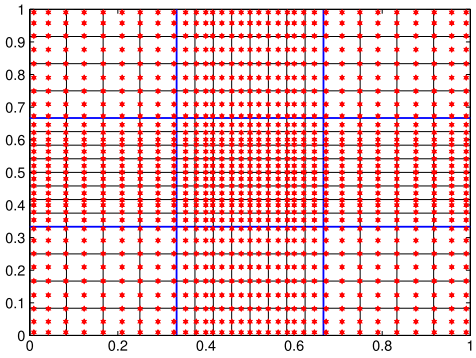

(e) C^2-cubic spline with C^1 interface line (in blue color).

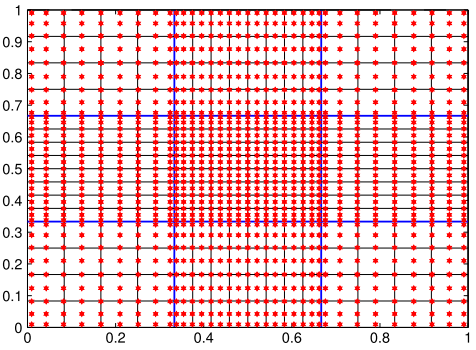

(f) C^2-cubic spline with C^0 interface line (in blue color).

Fig. 16. Derivative superconvergence points for cubic tensor product case with non-uniform mesh partition: (a) C^0-cubic spline; (b) C^1-cubic spline; (c) C^2-cubic spline; (d) C^1-cubic spline with C^0 interface line (in blue color); (e) C^2-cubic spline with C^1 interface line (in blue color); (f) C^2-cubic spline with C^0 interface line (in blue color). (For interpretation of the references to color in this figure legend, the reader is referred to the web version of this article.)

of the reduced continuity interface line will shift at the derivative superconvergent lines of their reduced continuity counterparts while in other part of the domain they will be at (3×3)-Gauss Lobatto points.

5.2.3. Computation of superconvergence points for LR B-spline spaces

To find the derivative superconvergence points for Poisson problem on adaptive structured mesh of LR B-splines of degree two, $\mathcal{S}^2_{\Omega_h}$, we consider an example of LR mesh shown in Fig. 17(a) with three domain of interests $K_i(\xi, H_i)$,

for $i = 1, 2, 3$. The domain of interest $K_1(\xi, H_1)$ is considered within the fine mesh of two level of refinements, while the cases of $K_2(\xi, H_2)$ and $K_3(\xi, H_3)$ represent different interface regions affected by one side and both sides of refinements, respectively. The domain $K_3(\xi, H)$ to compute the Neumann projection for the domain of interest $K_3(\xi, H_3)$ is also shown in Fig. 17(a). The B-splines basis functions representation on the LR mesh of Fig. 17(a) is shown Fig. 17(b). The green circle represents the coarse basis functions and red circle represents the fine basis functions, while the blue circle represents the coarse basis function whose supports were affected via the local refinement. The computed derivatives are obtained by finding the zeros of the derivatives of the difference between the monomials $\{Q_1, Q_2\}$ and its Neumann elliptic projections, where the monomials are defined as

$$Q_1(\mathbf{x}) = (x_1 - \bar{x}_1)^{(p+1)} \quad \text{and} \quad Q_2(\mathbf{x}) = (x_2 - \bar{x}_2)^{(p+1)}.$$

The zeros of derivative components with respect to $Q_1(x)$ and $Q_2(x)$ are represented by the blue and red lines in Fig. 17(c), (e), and (g) for the domain of interests $K_1(\xi, H_1)$, $K_2(\xi, H_2)$, and $K_3(\xi, H_3)$, respectively. The location of computed derivative superconvergence points for these cases is given by the common zeros of the derivatives with respect to $Q_1(x)$ and $Q_2(x)$ as shown in Fig. 17(d), (f) and (h). The computed derivative superconvergence points for the case of LR B-spline mesh with C^0-quadratic B-splines for the domain of interests $K_i(\xi, H_i)$, for $i = 1, 2, 3$ are shown in Fig. 18.

We also found that the location of derivative superconvergence points for tensor product cases as discussed here will remain the same for Poisson and Laplace equations. So all the above results also hold for the case of Laplace equation.

6. Abstract recovery operator G_h

In this section we define the *abstract* recovery operator G_h which act on the FE approximation u_h to give an approximation to the gradient ∇u. In particular we will focus on the set of conditions proposed by Ainsworth and Craig in [75] which constitutes a good approximation to the gradient in order for the resulting estimator to be asymptotically exact. A gradient recovery operator on V_h is a linear operator $G_h : V_h \to [V_h]^n$ that satisfy the following properties:
(i) *Consistency condition*: Whenever $u \in \mathbb{P}_{p+1}(\Omega)$

$$G_h(\mathcal{I}_h u) \equiv \nabla u \tag{113}$$

where $\mathcal{I}_h$ is the interpolation (or projection) operator. Here we consider $\mathcal{I}_h$ as the Neumann projection operator defined in Section 5.
(ii) *Localizing condition*: In order to ensure that the scheme is truly local and the sub-domain $\hat{\Omega}_i^h := \cup_{j \in adj(i)} \Omega_j^h$ (or element patch) are small, we shall make a restriction upon the cardinality of the indexing sets. Then the localizing condition becomes: For any $x^* \in \Omega_i^h$, $G_h[v](x^*)$ depends only upon the values of ∇v on the domain $\hat{\Omega}_i^h$. Further, $i \in \text{adj}(i)$ and there should exist a constant M, which is independent of h such that,

$$\text{card}[\text{adj}(i)] \leq M, \quad \forall i. \tag{114}$$

(iii) *Boundedness and linearity condition*: There exists a constant C, which is independent of h

$$|G_h[v]|_{0,\infty,\Omega_i^h} \leq C|v|_{1,\infty,\hat{\Omega}_i^h}. \ \forall v \in V_h. \tag{115}$$

Now we will show that the SPR operator presented in Section 4.2 will satisfy the above stated set of conditions. It can be seen easily that the present SPR operator will satisfy the localization condition (ii) and boundedness and linearity conditions (iii) by following the standard technique as shown in an example from [75]. Here we mainly focus to satisfy the consistency condition (i) which in general will be expected to obtain an approximation consistent with the true gradient under favorable circumstances.

6.1. Consistency of SPR in one dimension

In Figs. 19(a)–19(b), we show that the consistency condition (i) is satisfied by the SPR operator defined by Eq. (43) considered as G_h here, for quadratic spline approximating space on uniform mesh using two Gauss–Legendre points as the derivative superconvergence points from Table 3. Here we consider the exact solution $u(x) = x^3 \in \mathbb{P}_3(\Omega)$

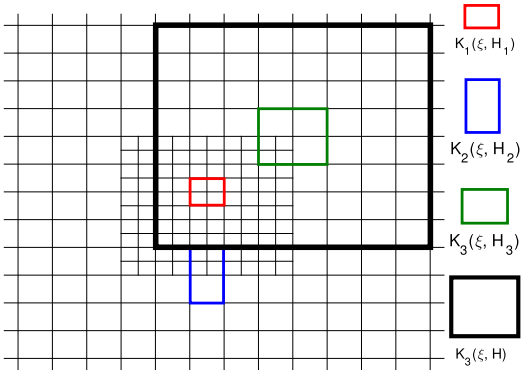

(a) $K_i(\xi, H_i)$ for $i = 1, 2, 3$ and $K_3(\xi, H)$ on LR mesh.

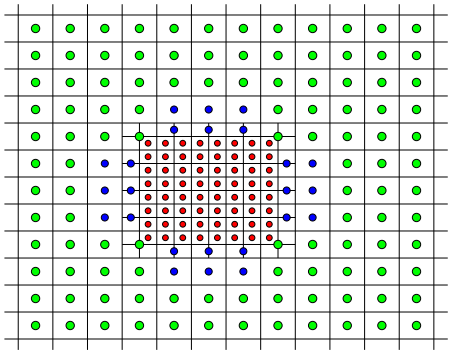

(b) Basis functions representation: C^0 quadratic LR B-splines.

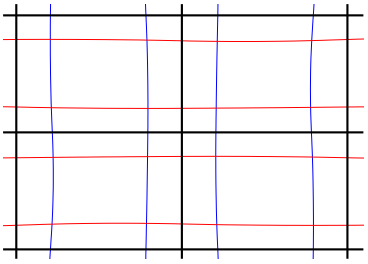

(c) Zeros lines of derivatives.

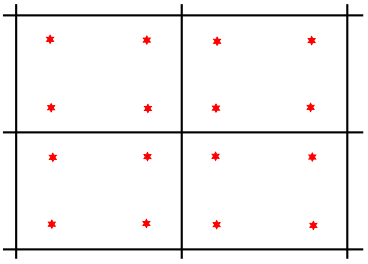

(d) Derivative Sup. pts.

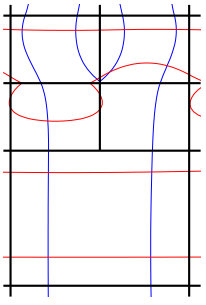

(e) Zeros lines of derivatives.

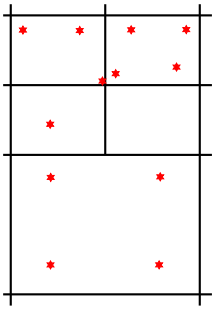

(f) Derivative Sup. pts.

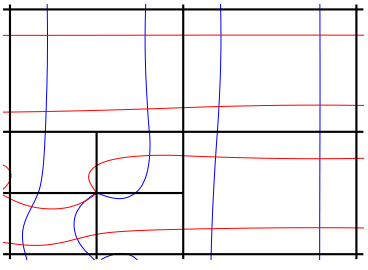

(g) Zeros lines of derivatives.

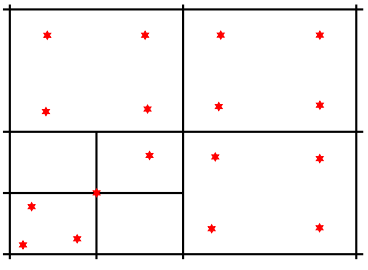

(h) Derivative Sup. pts.

Fig. 17. C^1 quadratic LR B-splines case: (a) Structured LR mesh with computational domain of interests $(K_i(\xi, H_i))$, $i = 1, 2, 3$ and extended patch $K_3(\xi, H)$ for Neumann projection; (b) C^1-quadratic LR B-splines basis function representation; (c) Zeros lines of the derivatives for $Q_1(x)$ and $Q_2(x)$ on $K_1(\xi, H_1)$; (d) Derivative superconvergence points at $K_1(\xi, H_1)$; (e) Zeros lines of the derivatives for $Q_1(x)$ and $Q_2(x)$ on $K_2(\xi, H_2)$; (f) Derivative superconvergence points at $K_2(\xi, H_2)$; (g) Zeros lines of the derivatives for $Q_1(x)$ and $Q_2(x)$ on $K_3(\xi, H_3)$; (h) Derivative superconvergence points at $K_3(\xi, H_3)$. (For interpretation of the references to color in this figure legend, the reader is referred to the web version of this article.)

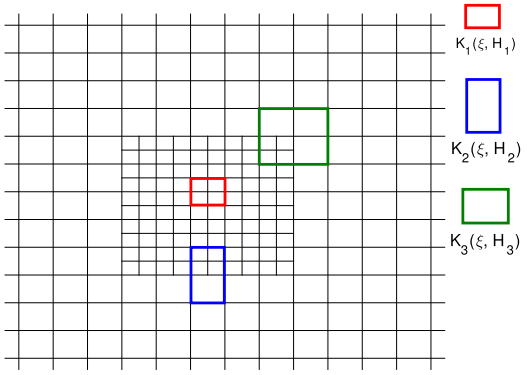

(a) $K_i(\xi, H_i)$ for $i = 1, 2, 3$ on LR mesh.

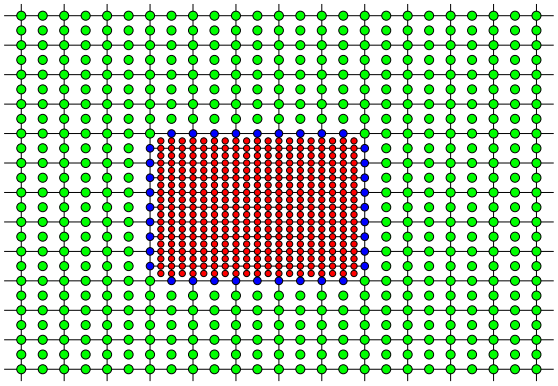

(b) Basis functions representation: C^0 quadratic LR B-splines.

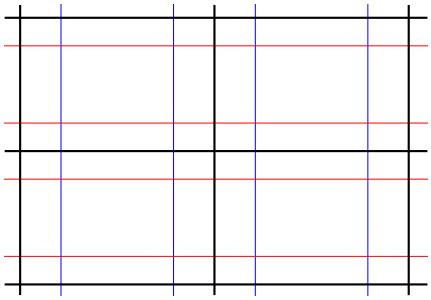

(c) Zeros lines of derivatives.

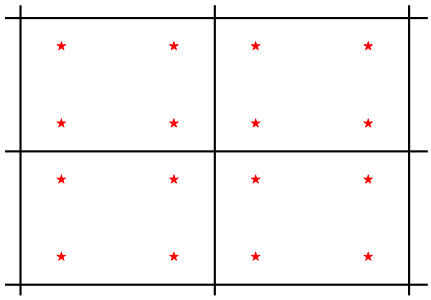

(d) Derivative Sup. pts.

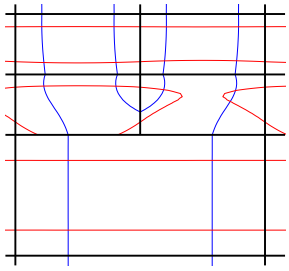

(e) Zeros lines of derivatives.

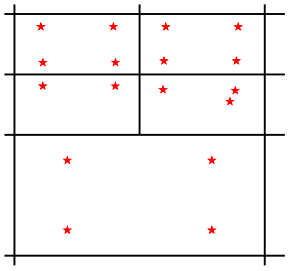

(f) Derivative Sup. pts.

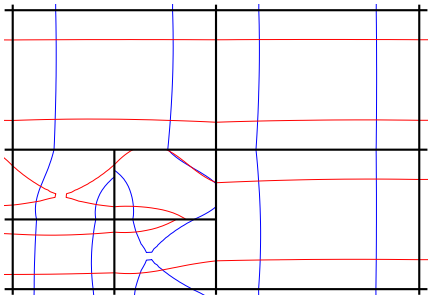

(g) Zeros lines of derivatives.

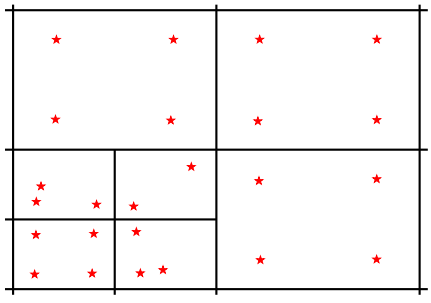

(h) Derivative Sup. pts.

Fig. 18. C^0 quadratic LR B-splines case: (a) Structured LR mesh with computational domain of interests $(K_i(\xi, H_i))$, $i = 1, 2, 3$; (b) C^0-quadratic LR B-splines representation; (c) Zeros lines of the derivatives for $Q_1(x)$ and $Q_2(x)$ on $K_1(\xi, H_1)$; (d) Derivative superconvergence points at $K_1(\xi, H_1)$; (e) Zeros lines of the derivatives for $Q_1(x)$ and $Q_2(x)$ on $K_2(\xi, H_2)$; (f) Derivative superconvergence points at $K_2(\xi, H_2)$; (g) Zeros lines of the derivatives for $Q_1(x)$ and $Q_2(x)$ on $K_3(\xi, H_3)$; (h) Derivative superconvergence points at $K_3(\xi, H_3)$.

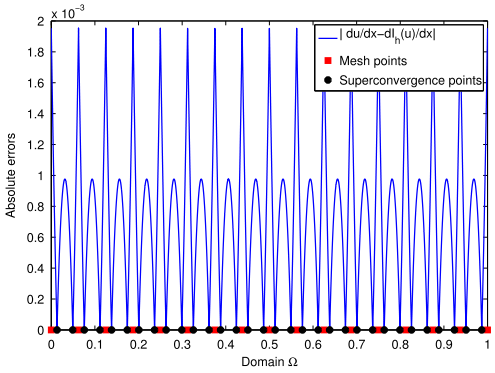

(a) Absolute error on domain Ω.

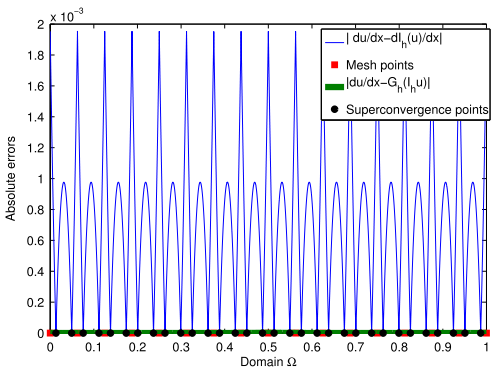

(b) Consistency of recovery operator G_h.

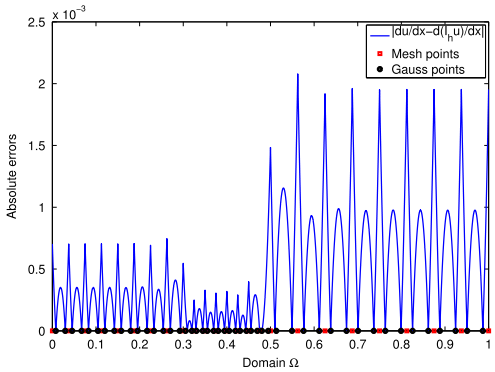

(c) Absolute error on domain Ω.

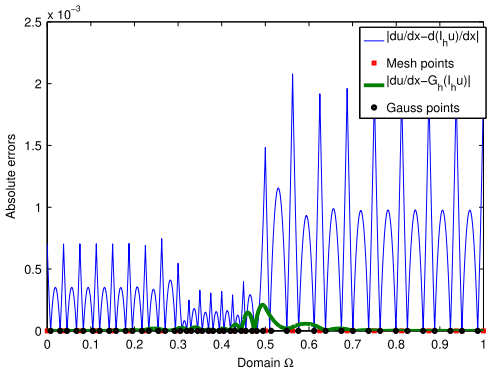

(d) Consistency of recovery operator G_h.

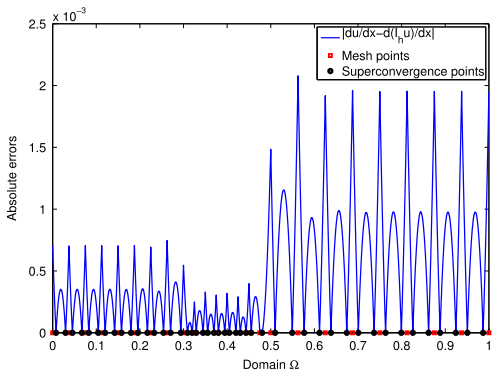

(e) Absolute error on domain Ω.

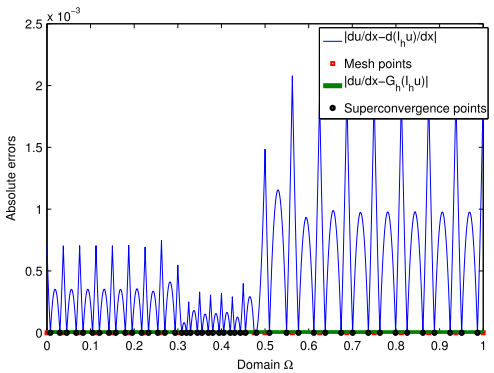

(f) Consistency of recovery operator G_h.

Fig. 19. One dimensional case: The consistency of SPR operator considered as G_h here; *first* row satisfies the consistency condition on uniform mesh with two Gauss–Legendre points as sampling point in the SPR procedure, *second* row does not satisfies the consistency condition on a non-uniform mesh with two Gauss–Legendre points as sampling point in SPR procedure, *third* row satisfies the consistency condition on general non-uniform mesh with computed true derivative superconvergence points as sampling point in SPR procedure, where we have considered $u = x^3 \in \mathbb{P}_3(\Omega)$ and $\mathcal{I}_h$ a local Neumann projection of u in quadratic B-spline space. (For interpretation of the references to color in this figure legend, the reader is referred to the web version of this article.)

and $\mathcal{I}_h$ as the Neumann projection operator defined by (59)–(60). In general one can choose $\mathcal{I}_h$ as a interpolation operator instead of local Neumann projection as considered here, but the local Neumann projection is general and can be extended to multi-dimensional cases. In Fig. 19(a) we show the absolute error in the derivative of u and the

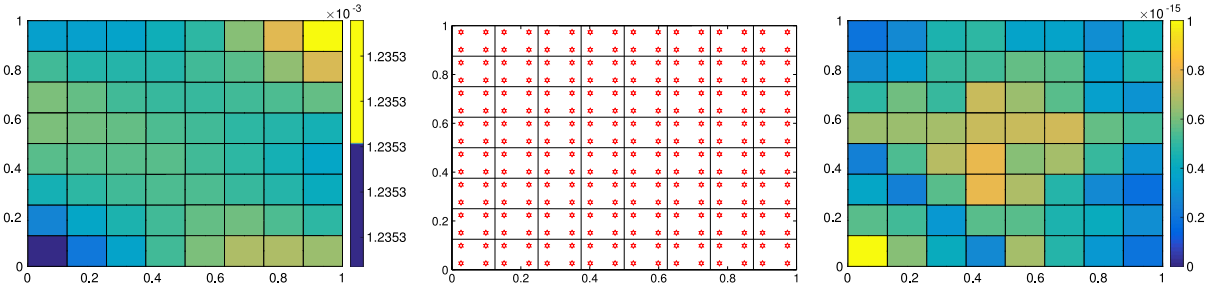

(a) $\|\nabla u - \nabla(\mathcal{I}_h u)\|_{L^2(\Omega)} := 9.88e{-}03.$ (b) LR mesh with superconvergence points. (c) $\|\nabla u - G_h(\mathcal{I}_h u)\|_{L^2(\Omega)} := 4.17e{-}15.$

Fig. 20. Two dimensional case: The consistency of SPR operator considered as G_h here; The SPR operator G_h satisfies the consistency condition on uniform mesh with (2×2)-Gauss Legendre points as sampling point in SPR procedure, where we have considered $u = (2x^3-3x^2)+(2y^3-3y^2) \in \mathbb{P}_3(\Omega)$ and $\mathcal{I}_h$ a local Neumann projection of u in quadratic B-spline space.

location of superconvergence points with dark black circles which coincide with the two Gauss–Legendre points on each mesh intervals. While in Fig. 19(b) we confirm that the recovered gradient obtained using the SPR operator of Section 4.2 results in exact derivative du/dx and the absolute error becomes zeros which is shown with the green curve. In Fig. 19(d), we consider the case of non-uniform mesh and show that the consistency condition is not satisfied when we use the two Gauss–Legendre points, whereas in Fig. 19(f) the consistency conditions are again satisfied when we use the true superconvergence points computed by our procedure presented in Section 5. Notice that the use of two Gauss–Legendre points gives zero consistency error at certain number of elements away from the change in element size, see 19(d). However, nearby the transition the true superconvergent points are located differently from the corresponding Gauss–Legendre points.

6.2. *Consistency of SPR in two dimension*

In Fig. 20, we illustrate that the consistency condition (i) is satisfied by the SPR operator defined by Eq. (43) considered as G_h here, for quadratic spline approximating space on uniform mesh using the (2×2)-Gauss Legendre points as derivative superconvergence points from Table 3. Here we consider the exact solution $u = (2x^3 - 3x^2) + (2y^3 - 3y^2) \in \mathbb{P}_3(\Omega)$ and $\mathcal{I}_h$ as the Neumann projection operator defined by (102)–(103). Fig. 20(a) shows the L^2-norm error in the gradient of u and the location of superconvergence points which coincide with the (2×2)-Gauss Legendre points on each mesh elements are shown in Fig. 20(b). While in Fig. 20(c) we show that the recovered gradient obtained using the SPR operator of Section 4.2 results in exact gradient and the absolute error in the projected gradient becomes numerically zero as shown in Fig. 20(c). In Fig. 21 we consider the case with a general non-uniform mesh of quadratic LR B-spline. It can be seen from Fig. 21(b) that the consistency condition is not satisfied when we use the (2×2)-Gauss Legendre points on a general non-uniform mesh with quadratic LR B-spline space approximation in our SPR procedure. While in Fig. 21(d) the consistency conditions are satisfied when we use the computed superconvergence points using the procedure developed in Section 5. It can also be noticed from Fig. 21(b) that although the consistency condition is not satisfied on a general non-uniform mesh using (2×2)-Gauss Legendre points still the L^2-norm of the projected error $\|\nabla u - G_h(\mathcal{I}_h u)\|_{L^2(\Omega)}$ has a smaller value than the error in the Neumann projection $\|\nabla u - \nabla(\mathcal{I}_h u)\|_{L^2(\Omega)}$. Below we give a sketch of our ideas to prove the superconvergence of the proposed SPR procedure based on the use of computed superconvergence points. Assume that the consistency condition is fulfilled, then given that the Bramble–Hilbert lemma together with the stability property (in the H^1 norm) can be proven for the operator $\mathcal{I}_h$, we have that the following proposition to hold:

Proposition 6.1. *Let $u \in H^{p+2}(\Omega) \cap H_0^1(\Omega)$ be the exact solution of the elliptic problem (17)–(19) and $\mathcal{I}_h u$ be its elliptic Neumann projection in $\mathcal{S}^p_{\Omega_h}$. Suppose that G_h operator satisfy* (i)–(iii)*, then*

$$\|\nabla u - G_h(\mathcal{I}_h u)\|_{L^2(\Omega)} \leq C h^{p+1} \|u\|_{H^{p+2}(\Omega)}. \tag{116}$$

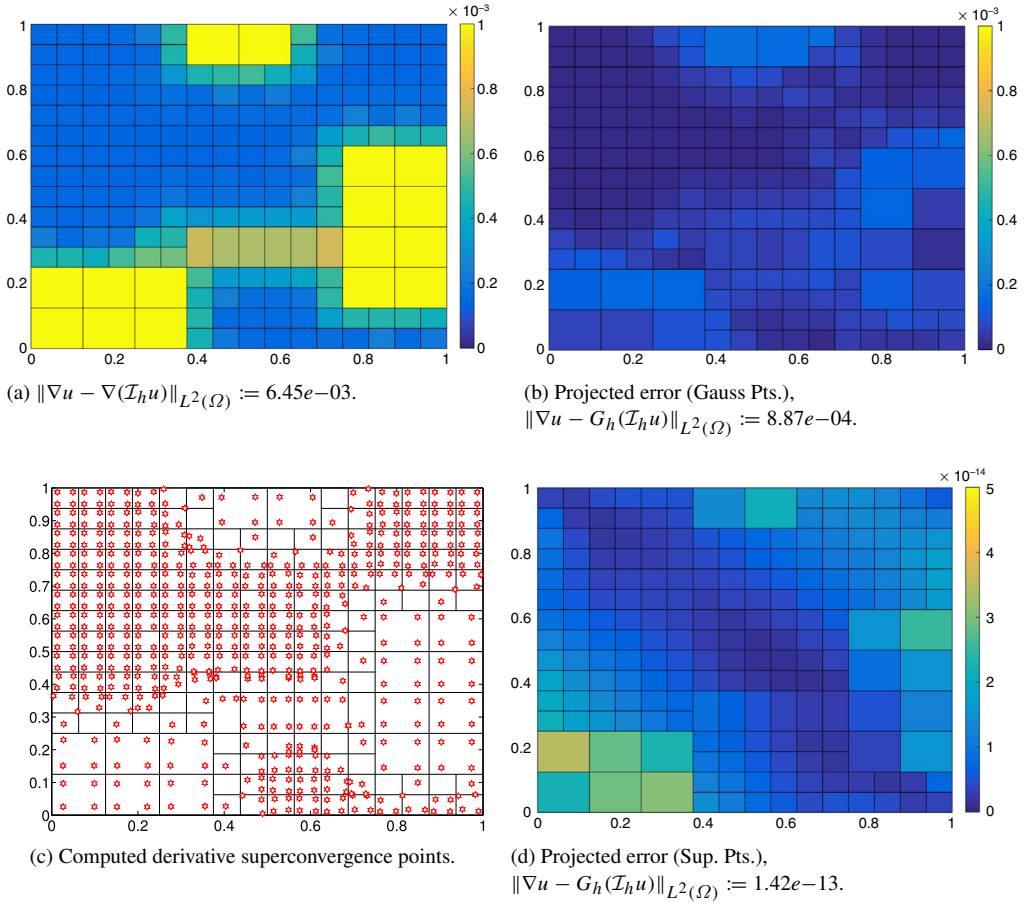

(a) $\|\nabla u - \nabla(\mathcal{I}_h u)\|_{L^2(\Omega)} := 6.45e{-}03$.

(b) Projected error (Gauss Pts.), $\|\nabla u - G_h(\mathcal{I}_h u)\|_{L^2(\Omega)} := 8.87e{-}04$.

(c) Computed derivative superconvergence points.

(d) Projected error (Sup. Pts.), $\|\nabla u - G_h(\mathcal{I}_h u)\|_{L^2(\Omega)} := 1.42e{-}13$.

Fig. 21. Two dimensional case: The consistency of SPR operator considered as G_h here; a L^2-norm of the error between the gradient of u and its projection $\mathcal{I}_h u$, (b) SPR operator G_h with (2×2)-Gauss Legendre points as sampling point on a general non-uniform LR mesh does not satisfies the consistency condition, (c) computed derivative superconvergence points using computer based algorithm (d) SPR operator G_h with computed derivative superconvergence points as sampling point on a general non-uniform LR mesh does satisfies the consistency condition. Here we have considered $u = (2x^3 - 3x^2) + (2y^3 - 3y^2) \in \mathbb{P}_3(\Omega)$ and $\mathcal{I}_h$ a local Neumann projection of u in quadratic LR B-spline space.

Now using the triangle inequality, we can write

$$\|\nabla u - G_h(u_h)\|_{L^2(\Omega)} \leq \|\nabla u - G_h(\mathcal{I}_h u)\|_{L^2(\Omega)} + \|G_h(\mathcal{I}_h u) - G_h(u_h)\|_{L^2(\Omega)}.$$

Then by using the result from Proposition 6.1 and the boundedness and linearity condition (iii) with quasi-uniform mesh having an upper bound on G_h independent of h, we can obtain

$$\|\nabla u - G_h(u_h)\|_{L^2(\Omega)} \leq C h^{p+1} \|u\|_{H^{p+2}(\Omega)} + C\|\nabla \mathcal{I}_h u - \nabla u_h\|_{L^2(\Omega)}, \tag{117}$$

where C is a constant independent of h.

Now if we assume the superconvergence property in FE solution u_h holds, which is true under certain regularity conditions regarding the partition Ω_h, the regularity of the true solution and the topology of the mesh, an estimate of the following form holds:

$$\|\nabla u_h - \nabla \mathcal{I}_h u\|_{L^2(\Omega)} \leq C(u) h^{p+1}, \tag{118}$$

while a priori error estimates on the other hand give only $\|\nabla u - \nabla u_h\|_{L^2(\Omega)} \leq C(u) h^p$.

Then on inserting (119) into (117) the following result holds.

Proposition 6.2. *Let $u \in H^{p+2}(\Omega) \cap H_0^1(\Omega)$ be the exact solution of the elliptic problem (17)–(19) and $u_h \in \mathcal{S}^p_{\Omega_h,0}$ be the spline based FE solution (22). Then*

$$\|\nabla u - G_h(u_h)\|_{L^2(\Omega)} \leq C h^{p+1} \|u\|_{H^{p+2}(\Omega)}. \tag{119}$$

The above result gives the superconvergence in the SPR procedure of order 1 which can be obtained in very special cases, e.g. with uniform mesh topology and with enough regularity of the solution. In general, on practical quasi-uniform meshes, the results may reduce to

$$\|\nabla u - G_h(u_h)\|_{L^2(\Omega)} \leq C(u) h^{p+\alpha}, \tag{120}$$

where $\alpha \in (0, 1]$. Then the SPR procedure is superconvergent of order α instead of order 1. The results presented in (119) and (120) are verified by numerical results of Section 7.

7. Numerical results

In this section we report some numerical studies to demonstrate the accuracy of the recovered derivatives achieved by the proposed recovery procedures and their rates of convergence. The main focus will be to study the superconvergence behavior of recovery procedures and the performance of recovery based error estimators developed in this article. We have divided numerical results into three main parts where we will study the followings:

- Superconvergence behavior of gradient recovery procedures under uniform h-refinement.
- Superconvergence behavior of gradient recovery procedures under adaptive meshes obtained through *Structured mesh* refinement strategy of LR B-splines.
- Adaptive isogeometric analysis using a posteriori error estimators proposed in this article.

Error measures

We consider several numerical examples for model elliptic problem with available exact solution. The effectiveness of the various recovery procedures is assessed by evaluating the following relative errors (%) in energy norm

$$\text{Exact error } \|e\|_{RE} := \|u - u_h\|_{RE} = \frac{\|\nabla u - \nabla u_h\|_{L^2(\Omega)}}{\|\nabla u\|_{L^2(\Omega)}} \times 100\%, \tag{121}$$

$$\text{Projected error } \|e^*\|_{RE} := \|u - u_h^*\|_{RE} = \frac{\|\nabla u - \nabla u_h^*\|_{L^2(\Omega)}}{\|\nabla u\|_{L^2(\Omega)}} \times 100\%. \tag{122}$$

Here the superscript $*$ represents the recovery procedures and will be replaced appropriately by $* =$ CL2P, DLSF, SPR in the article.

Error estimators (η_h^*)

The error estimator (η_h^*) and the element indicator (η_{el}^*) are defined by

$$\eta_h^* = \left(\sum_{el=1}^{Nel} (\eta_{el}^*)^2 \right)^{1/2} \quad \text{and} \quad \eta_{el}^* = \|\nabla u_h^* - \nabla u_h\|_{L^2(\Omega_{el})}. \tag{123}$$

Effectivity indices (θ)

To measure the quality of proposed recovery based error estimators in this article, we consider the following global and local effectivity indices

$$\theta^* = \frac{\eta_h^*}{\|\nabla u - \nabla u_h\|_{L^2(\Omega)}} \quad \text{and} \quad \theta_{local}^* = \frac{\|\nabla u_h^* - \nabla u_h\|_{L^2(\Omega_{el})}}{\|\nabla u - \nabla u_h\|_{L^2(\Omega_{el})}}. \tag{124}$$

Here we refer to $\eta_h^{(*)}$ as an asymptotically exact error estimator if $\lim_{h\to 0} \theta^{(*)} = 0$.

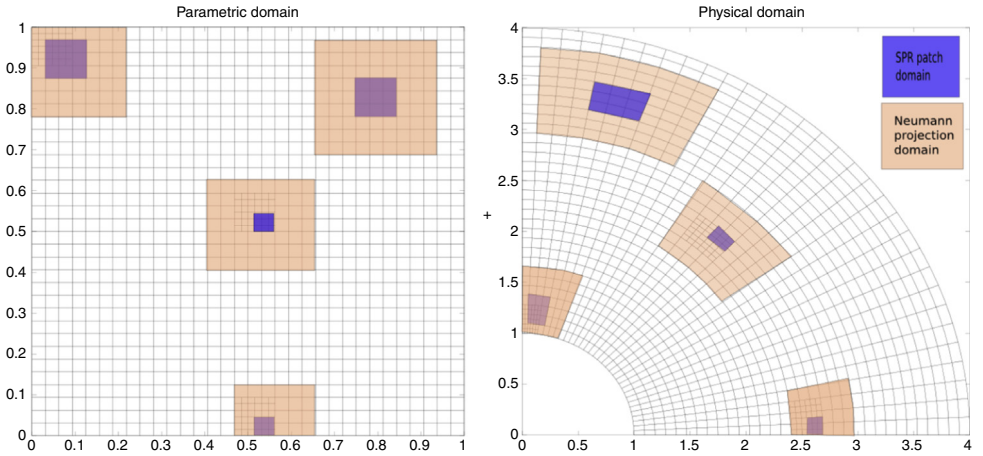

Fig. 22. Examples of SPR-patches $\hat{\Omega}_{el}^{A}$, Ω_{el}^{A} and Neumann projection domains $\hat{\Omega}_{el,sp}^{A}$, $\Omega_{el,sp}^{A}$ in the parametric (to the left) and physical domains (to the right), respectively for degree $p = 2$. (For interpretation of the references to color in this figure legend, the reader is referred to the web version of this article.)

7.1. Adaptive IGA using SPR based error estimator

In this article we consider the following procedure to solve a given elliptic boundary value problem with adaptive IGA using SPR based error estimator:

Input: Let Ω_h^0 be an initial coarse discretized domain for the physical domain Ω with associated discrete spline space $\mathcal{V}_h^0$. Suppose a marking parameter $\beta = 5\%$ for the **Mark** step of the procedure is given. Then for successive adaptive steps $\ell = 0, 1, 2, \ldots$ do the following:

Solve: Compute the isogeometric FE solution $u_h^\ell \in \mathcal{V}_h^\ell$ such that

$$\boxed{a(u_h^\ell, v_h^\ell) = f(v_h^\ell) \;\; \forall \; v_h^\ell \in \mathcal{V}_h^\ell}$$

where $u_h^\ell = \sum_{A=1}^{N_{dim}^\ell} c_A^\ell R_A^\ell$ with the basis function R_A^ℓ with respect to B-splines/NURBS (or LR B-splines space) $\mathcal{V}_h^\ell$ and c_A^ℓ are control variables at level ℓ.

Estimate: Compute the SPR based error estimator

$$\boxed{\eta_{SPR}^\ell = \left(\sum_{el=1}^{Nel} (\eta_{el}^\ell)^2 \right)^{1/2}, \quad \text{with elementwise indicator } \; \eta_{el}^\ell = \|\sigma_{SPR}^\ell - \sigma_h^\ell\|_{L^2(\Omega_{el})}.}$$

Here $\sigma_h^\ell = \nabla u_h^\ell$ is the gradient of computed solution u_h^ℓ and $\sigma_{SPR}^\ell(\mathbf{x}) = \sum_{\forall A} \sigma_A^\ell R_A(\mathbf{x})$ is the global gradient recovered field obtained from the ***Step 4*** of the SPR procedure given below.

Stop, if σ_h is sufficiently accurate (e.g., η_{SPR}^ℓ is sufficiently small). Otherwise go to next step.

Mark: We adopt the fixed β percentage marking strategy from [8] based on the error contribution at each basis functions $\eta_{el,A}$ with largest errors, which is obtained by adding elementwise errors within the support of each basis R_A. For the implementation in this article we always consider $\beta = 5\%$ of the basis functions to refine in each adaptive refinement step. Put the selected basis functions to refine in the set $\mathcal{S}_{mark}$.

Refine: The marked basis in the set $\mathcal{S}_{mark}$ is refined based on *Structured mesh refinement algorithm* of Section 1. This forms a new refined mesh $\Omega_h^{\ell+1}$ and an associated discrete space $\mathcal{V}_h^{\ell+1}$. Go to **Solve**.

SPR procedure

Step 1: For each basis function R_A^ℓ's with $A = 1, 2, \ldots, N_{dim}^\ell$, form a SPR element patch Ω_{el}^A which contains all the elements within its support. The SPR patches are highlighted with blue color in Figure 22 for the $p = 2$ case. Note that along the boundary we have to consider an extended patch as described in Section 4.

Step 2: Now perform gradient SPR either based on computed superconvergence points (CSCP) or precomputed superconvergence points (PSCP). Based on the choice go to either **Step 2a** or **2b**.

Step 2a: Select the sampling points for each element of the SPR patch Ω_{el}^A from Table 3 . Go to **Step 3**.

Step 2b: Compute the derivative superconvergence points within each SPR patch Ω_{el}^A after solving the local Neumann projection on the parametric domain $\hat{\Omega}_{el,sp}^A$, i.e., Find $Q^h_{\hat{\Omega}_{el,sp}^A} \in \mathcal{S}_{\hat{\Omega}_{el,sp}^A}$ such that

$$\left(\nabla(Q^{\bar{\mathbf{x}},(p+1)} - Q^h_{\hat{\Omega}_{el,sp}^A}), \nabla v\right) = 0 \quad \forall \ v \in \mathcal{S}_{\hat{\Omega}_{el,sp}^A},$$

$$\int_{\mathcal{S}_{\Omega_{el,sp}^A}} (Q^{\bar{\mathbf{x}},(p+1)} - Q^h_{\hat{\Omega}_{el,sp}^A}) d\Omega = 0,$$

where $Q^{\bar{\mathbf{x}},(p+1)}$ is the monomial of degree $p+1$ and $\mathcal{S}_{\hat{\Omega}_{el,sp}^A}$ is the restriction of the spline space to $\hat{\Omega}_{el,sp}^A$. Compute the superconvergence points as the common zeros of $\frac{\partial^i}{\partial x_i}(Q^{\bar{\mathbf{x}},(p+1)} - Q^h_{\hat{\Omega}_{el,sp}^A}) = 0$, for $i = 1, 2$ within the SPR patch domain $\hat{\Omega}_{el}^A$. The superconvergence points for physical domain Ω_{el}^A is obtained after applying the mapping on the parametric domain $\hat{\Omega}_{el}^A$. Go to **Step 3**.

Step 3: The recovered gradient is obtained after performing the local discrete least square fitting of $\sigma_\alpha^\ell = \mathbf{P}(\mathbf{x})\mathbf{a}_\alpha$ using PSCP (**Step 2a**) or CSCP points (**Step 2b**) within the SPR patches Ω_{el}^A for each derivative components separately, i.e., for $\alpha = x, y$.

Step 4: The global gradient recovered field $\sigma_{SPR}^\ell(\mathbf{x}) = \sum_{\forall A} \sigma_A^\ell R_A(\mathbf{x})$ is obtained with $\sigma_A^\ell = \{\sigma_x^\ell, \sigma_y^\ell\}_A$.

7.2. *Superconvergent gradient recovery under uniform h-refinement*

We consider three test examples with given smooth solution in this section. The aim here is to show the superconvergent behavior of the developed gradient recovery procedures under uniform h-refinement. For this we consider the case of B-spline and NURBS spaces of degrees $p = 2, 3, 4$. The location of optimal sampling points, i.e., the derivative superconvergence points are taken from Table 3 with respect to their degrees in the proposed recovery procedure of DLSF and SPR of Section 4.

7.2.1. *Example 1. (Sinus problem)*

We consider the following two dimensional elliptic problem

$$-\Delta u = f \quad \text{in } \Omega, \tag{125}$$

with homogeneous boundary condition

$$u = 0 \quad \text{on } \partial\Omega. \tag{126}$$

Here $\Omega = (0, 1)^2$ is a square domain and f is constructed to correspond to the exact solution

$$u(x, y) = \sin(2\pi x)\sin(2\pi y). \tag{127}$$

The error plots of exact error, projected error and estimated error in relative energy norm using the recovery procedures $* =$ CL2P, DLSF, SPR with B-splines of degree $p = 2, 3, 4$ are shown in Fig. 23(a), (c), (e), respectively. While the performance of the recovery procedure in terms of the effectivity index θ^* for $* =$ CL2P, DLSF, SPR with B-splines of degree $p = 2, 3, 4$ are shown in Fig. 23(b), (d), (f).

From the error plots of the projected error in Fig. 23(a), (c), (e), it can be noticed that the SPR procedure outperform other recovery procedures as the results are not only more accurate but clearly show the superconvergent behavior of order 1 in the recovered gradient in comparison to the exact error. It can also be seen in Fig. 23(a), (c), (e), that the projected errors with DLSF and CL2P procedures are also more accurate than the exact error, but the CL2P procedure does not show the superconvergence behavior of order 1 for degree $p = 2$, while its performance greatly improves for higher degrees and superconvergence behavior of order 1 is clearly observed.

In Fig. 23(b), (d), (f), we study the performance of recovery based error estimators and their performance in estimating the exact error under uniform h-refinement. All the recovery based error estimators show asymptotic exactness behavior, the SPR and CL2P recovery procedures are more rapidly approaching to the value 1 in comparison to DL2P procedure. For the case of higher degrees we noticed that the performance of CL2P increases while DL2P decreases. The SPR procedure has higher effectivity index on coarse meshes for higher degree B-splines, but as we refine the mesh the effectivity index rapidly tends to 1 and shows the desired asymptotic exactness behavior.

The comparison of the distribution of exact error vs. estimated error (at element level) obtained by different recovery procedures for quadratic B-splines at step 2 of uniform refinement is shown in Fig. 24, whereas the comparison of the deviation of local effectivity index $|\theta^*_{local} - 1|$ for degree $p = 2, 3, 4$ are shown in Fig. 25. The results displayed in Fig. 25 indicate that the recovery based error estimators capture the error at correct location as they are all very similar to the exact error distribution shown in 25(a).

The deviation of local effectivity index shown in Fig. 25 confirms that the quality of SPR based error estimator is better at element level than the others. The deviation of local effectivity index at element level is very close to zero in the region where we have the maximum error as displayed in Fig. 25(a). However, some disturbances may be observed along the boundary for higher degrees. This is well known behavior of the SPR-procedure and might be handled by introducing special recovery schemes for the patches along the boundary (see e.g. [34] and [35]). Notice that the global recovered gradient field using SPR (without special treatments of the boundaries) is still superconvergent of order one.

In this example we also notice that the estimated error for the recovery procedures is conservative and giving a bound on the exact error from above. Herein we do not guarantee that our error estimates are bounding the exact error (either from above or below). We focus instead on h-asymptotic exactness. Guaranteed upper and lower bounds is a topic for future investigation—see the discussion in the end of this article.

7.2.2. Example 2. (Circular domain problem)

Consider the following elliptic problem

$$-\Delta u = f \quad \text{in } \Omega, \tag{128}$$

with homogeneous boundary condition

$$u = 0 \quad \text{on } \partial\Omega, \tag{129}$$

the domain Ω is a quarter of an annulus as shown in Fig. 26 and the source term f is constructed correspond to the exact solution

$$u(x, y) = (x^2 + y^2 - 1)(x^2 + y^2 - 16)\sin(x)\sin(y). \tag{130}$$

The error plots of exact error, projected error and estimated error in relative energy norm using the recovery procedures $* =$ CL2P, DLSF, SPR with NURBS of degree $p = 2, 3, 4$ are shown in Fig. 27(a), (c), (e), respectively. While the performance of the recovery procedure in terms of the effectivity index θ^* for $* =$ CL2P, DLSF, SPR with NURBS of degree $p = 2, 3, 4$ are shown in Fig. 27(b), (d), (f).

From the error plots of the projected error in Fig. 27(a), (c), (e), it can be noticed that the DLSF and SPR procedures show the superconvergent behavior of order 1 in the recovered gradient in comparison to the exact error. The results with CL2P and DLSF procedures are similar to the previous case, where CL2P does not show the superconvergence

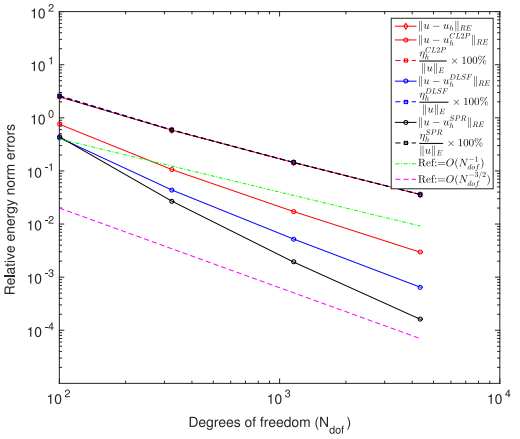

(a) Errors with quadratic splines.

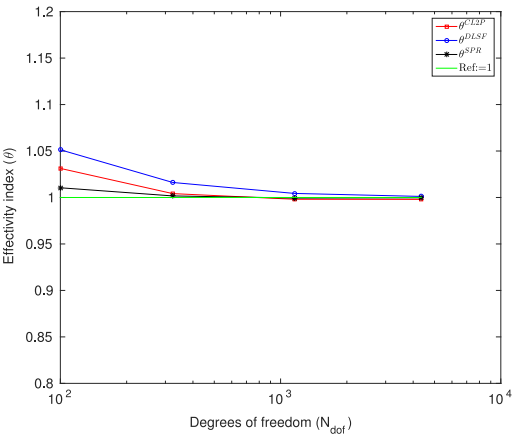

(b) Effectivity index with quadratic splines.

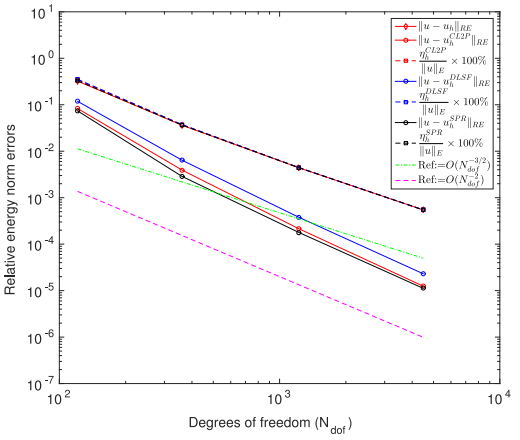

(c) Errors with cubic splines.

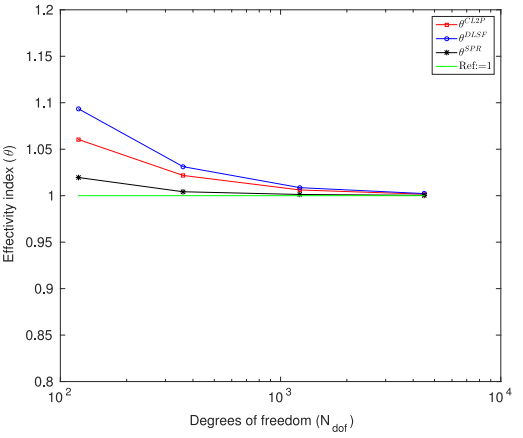

(d) Effectivity index with cubic splines.

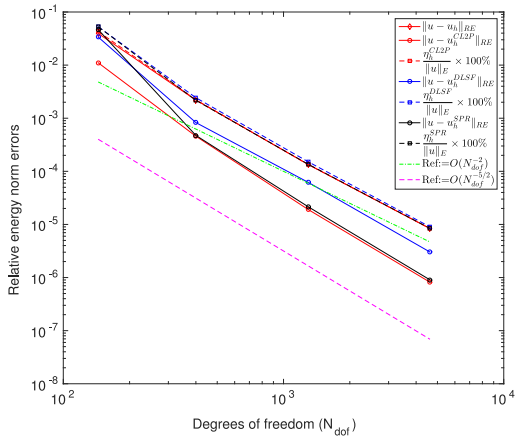

(e) Errors with quartic splines.

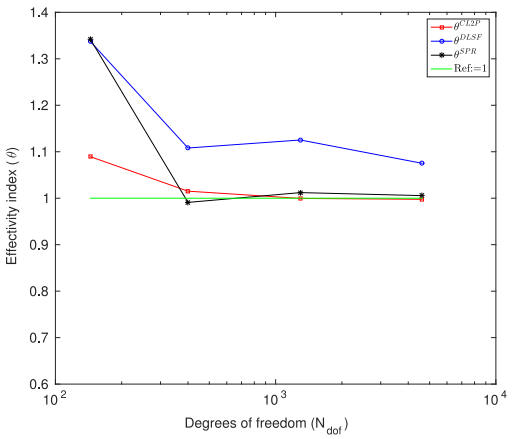

(f) Effectivity index with quartic splines.

Fig. 23. Sinus problem: Errors and effectivity index results obtained with different recovery procedures (CL2P, DLSF and SPR) using polynomial splines spaces of degrees $p = 2, 3, 4$ to approximate the solution u_h with uniform h-refinement.

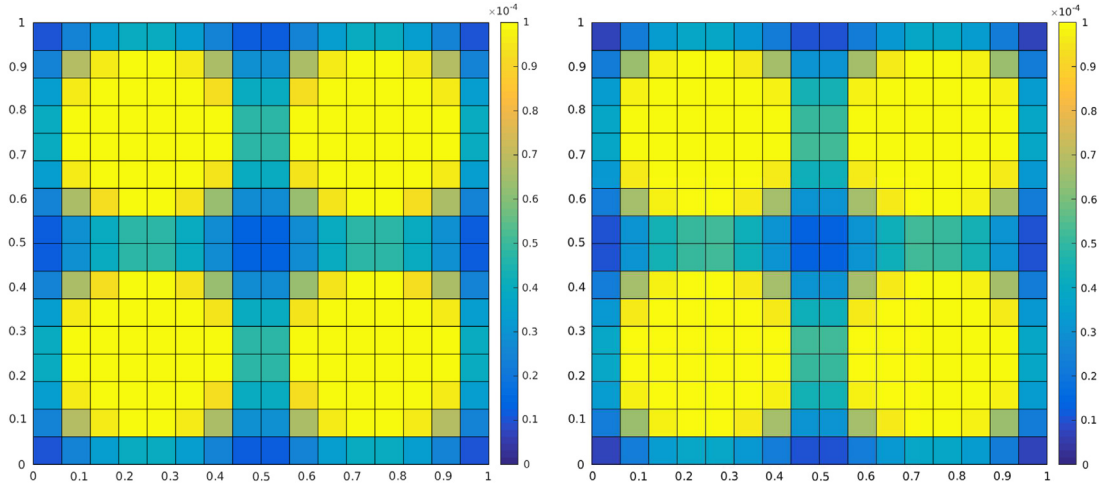

(a) Exact error distribution.

(b) CL2P error estimator.

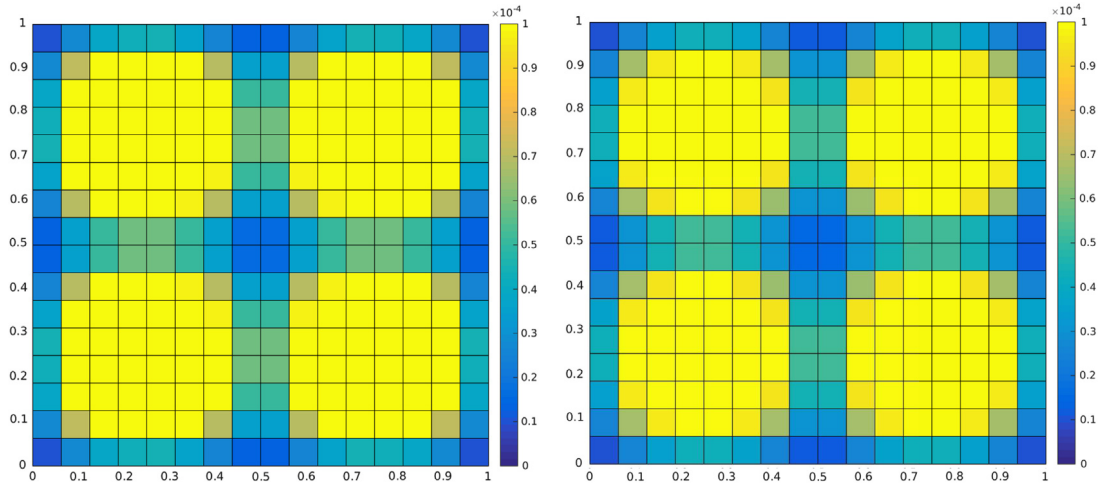

(c) DLSF error estimator.

(d) SPR error estimator.

Fig. 24. Sinus problem: Comparison of distribution of exact error vs. error estimator (at element level) obtained by Continuous L^2-projection (CL2P), Discrete least square fitting (DLSF) and Superconvergent patch recovery (SPR) for quadratic B-splines approximate solution u_h at step 2 of uniform refinement.

behavior of order 1 for degree $p = 2$, while its performance greatly improves for higher degrees and superconvergence behavior of order 1 is clearly observed, while the errors with DLSF will be less accurate in comparison to SPR and Cl2P for higher degrees. The projected errors with DLSF and CL2P procedures are always more accurate than the exact error, but with SPR procedure the projected error on the first coarse mesh is higher than exact error while the projected error after one step of refinement becomes more accurate and then shows superconvergence behavior of order 1.

In Fig. 27(b), (d), (f), we study the performance of recovery based error estimators and their performance in estimating the exact error under uniform h-refinement. All the recovery based error estimator shows asymptotic exactness behavior, the SPR and CL2P procedures are rapidly approaching to the value 1 in comparison to DL2P procedure. For the case of higher degrees we notice that the performance of CL2P increases while DL2P decreases. The SPR procedure shows higher effectivity index on coarse meshes for higher degree B-splines, but as we refine the mesh the effectivity index rapidly tends to 1 shows asymptotic exactness behavior.

The comparison of distribution of exact error vs. estimated error (at element level) obtained by different recovery procedures for quadratic NURBS at step 2 of uniform refinement is shown in Fig. 28, whereas the comparison of

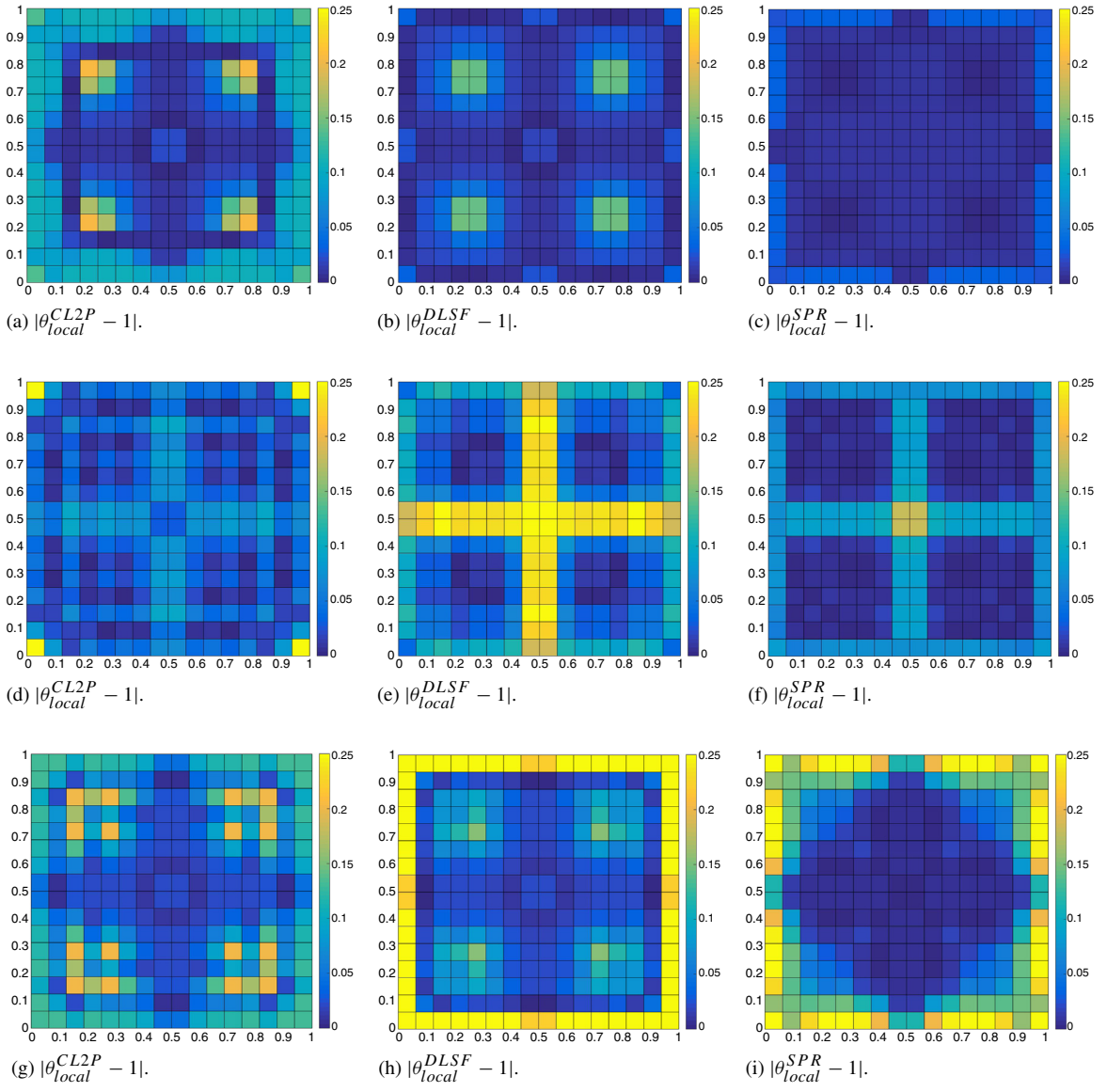

(a) $|\theta^{CL2P}_{local} - 1|$. (b) $|\theta^{DLSF}_{local} - 1|$. (c) $|\theta^{SPR}_{local} - 1|$.

(d) $|\theta^{CL2P}_{local} - 1|$. (e) $|\theta^{DLSF}_{local} - 1|$. (f) $|\theta^{SPR}_{local} - 1|$.

(g) $|\theta^{CL2P}_{local} - 1|$. (h) $|\theta^{DLSF}_{local} - 1|$. (i) $|\theta^{SPR}_{local} - 1|$.

Fig. 25. Sinus problem: Comparison of deviation of local effectivity index $|\theta^{*}_{local} - 1|$ obtained by Continuous L^2-projection (CL2P), Discrete least square fitting (DLSF) and Superconvergent patch recovery (SPR) for NURBS (first row ($p = 2$), second row ($p = 3$), and third row ($p = 4$)) approximate solution u_h at step 2 of uniform refinement.

deviation of local effectivity index $|\theta^{*}_{local} - 1|$ for degree $p = 2, 3, 4$ are shown in Fig. 29. The results displayed in Fig. 29 indicates that the recovery based error estimators capture the error at correct location which is very similar to the exact error distribution shown in 29(a).

The deviation of local effectivity index shown in Fig. 29 confirms the quality of all recovery based error estimators. The deviation of local effectivity index at element level is very close to zero in the region where we notice the maximum error from Fig. 29(a). It can be noticed from figures that SPR and DLSF are very comparable and better than CL2P for degrees $p = 2, 3$ while for degree $p = 4$ their performance is slightly disturbed along the boundary.

7.2.3. Example 3. (Smooth solution with non-homogeneous Dirichlet BC's)

Now we consider the elliptic problem

$$-\Delta u = f \quad \text{in } \Omega, \tag{131}$$

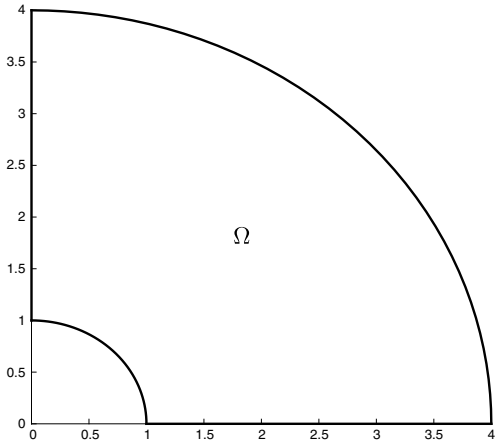

Fig. 26. Circular domain problem: Geometry for the quarter of an annulus.

with non-homogeneous boundary condition

$$u = g \quad \text{on } \partial\Omega, \tag{132}$$

where $\Omega = (0, 1)^2$, f and g are constructed to correspond to the exact solution

$$u(x, y) = (x^3 + y^2)\sin(xy). \tag{133}$$

The error plots of exact error, projected error and estimated error in relative energy norm using the recovery procedures $* =$ CL2P, DLSF, SPR with B-splines of degree $p = 2, 3, 4$ are shown in Fig. 30(a), (c), (e), respectively. While the performance of the recovery procedure in terms of the effectivity index θ^* for $* =$ CL2P, DLSF, SPR with B-splines of degree $p = 2, 3, 4$ are shown in Fig. 30(b), (d), (f).

From the error plots of the projected error in Fig. 30(a), (c), (e), we notice the similar pattern as in the first example that the DLSF and SPR procedures show the superconvergent behavior of order 1 in the recovered gradient in comparison to the exact error. The CL2P recovery procedure does not show the superconvergence behavior of order 1 for degree $p = 2$, while its performance greatly improves for higher degrees and superconvergence behavior of order 1 is clearly observed, while the errors with DLSF will be less accurate in comparison to SPR and Cl2P for higher degrees.

Fig. 30(b), (d), (f) show the recovery based error estimators are asymptotic exact under uniform h-refinement. The SPR and CL2P procedures are rapidly approaching to the value 1 in comparison to DL2P procedure. For the case of higher degrees we notice that the performance of CL2P increases while DL2P decreases which is similar to the previous examples.

The comparison of distribution of exact error vs. estimated error (at element level) obtained by different recovery procedures for quadratic B-spline at step 2 of uniform refinement is shown in Fig. 31, whereas the comparison of deviation of local effectivity index $|\theta^*_{local} - 1|$ for degree $p = 2, 3, 4$ are shown in Fig. 32. The results displayed in Fig. 32 indicate that the recovery based error estimators capture the error at correct location which is very similar to the exact error distribution shown in Fig. 32(a).

The deviation of local effectivity index shown in Fig. 32 confirms the quality of all recovery based error estimators. The deviation of local effectivity index at element level is very close to zero in the region where we notice the maximum error from Fig. 32(a). It can be noticed from the figures that SPR and DLSF are very comparable and better than CL2P for degree $p = 2$ while for degrees $p = 3, 4$ their performance is slightly disturbed along the boundary.

Discussion of results obtained for smooth solution problems

The numerical results obtained in Example 1–3 all confirm that the recovered gradient using DLSF and SPR are superconvergent of one order for smooth solution problems, whereas CL2P recover gradients are definitely more accurate than exact errors, and sometimes superconvergence of order between zero and one (here close to one) is also observed. All the recovery schemes are shown to be h-asymptotic exact for such smooth solution problems. However, the deviation from unity of the local effectivity index is pronounced along the boundary for SPR in all cases, whereas

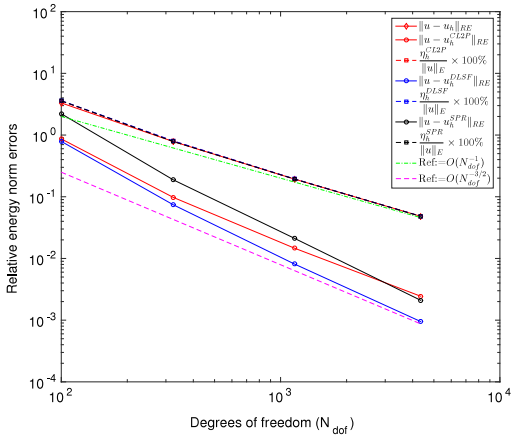

(a) Errors with quadratic NURBS.

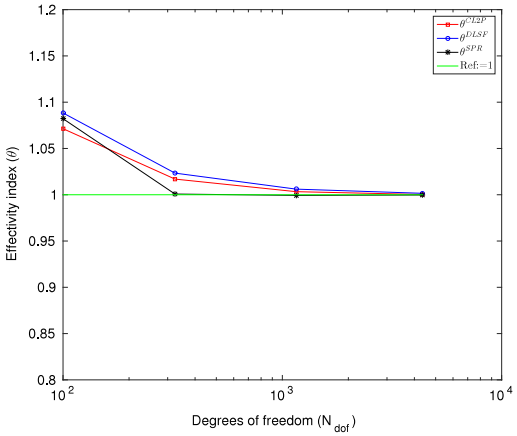

(b) Effectivity index with quadratic NURBS.

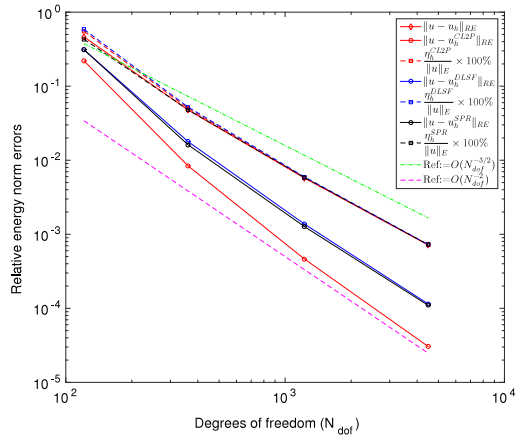

(c) Errors with cubic splines.

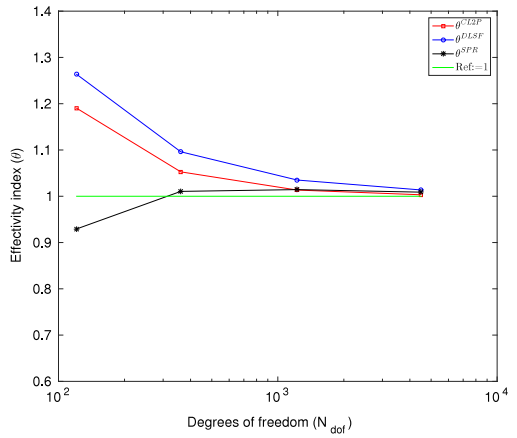

(d) Effectivity index with cubic NURBS.

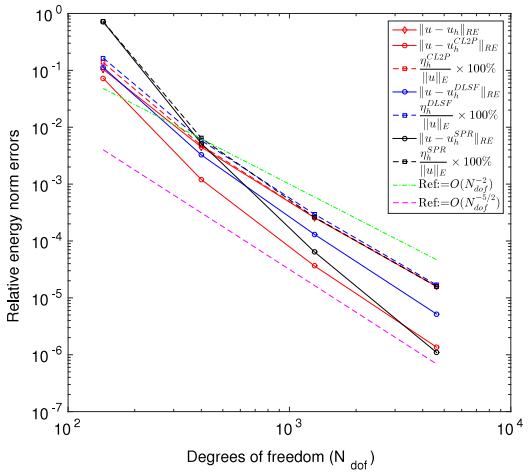

(e) Errors with quartic NURBS.

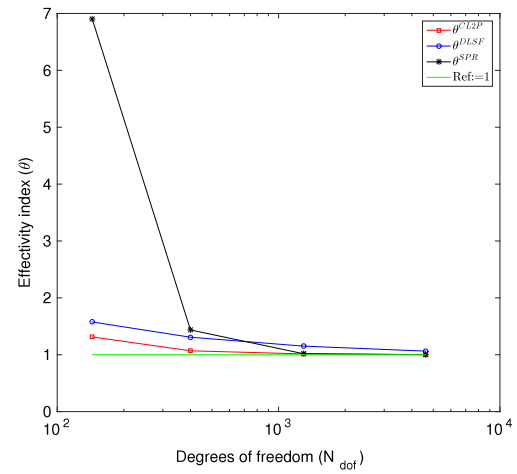

(f) Effectivity index with quartic NURBS.

Fig. 27. Circular domain problem: Errors and effectivity index results obtained with different recovery procedures (CL2P, DLSF and SPR) using NURBS spaces of degrees $p = 2, 3, 4$ to approximate the solution u_h with uniform h-refinement.

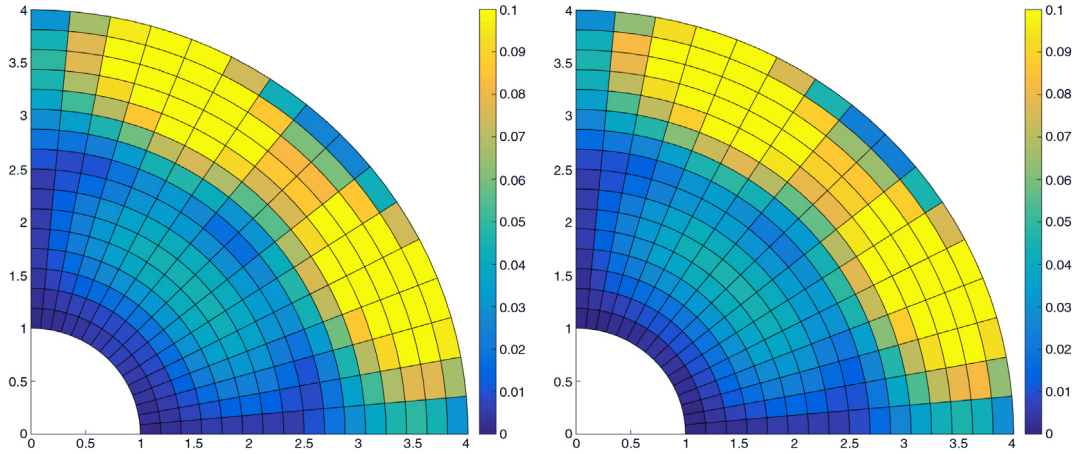

(a) Exact error distribution.

(b) CL2P error estimator.

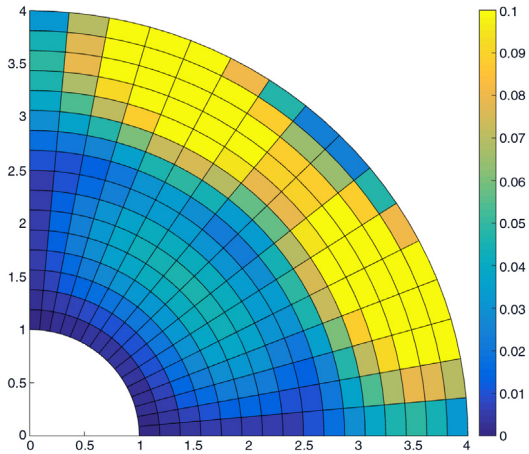

(c) DLSF error estimator.

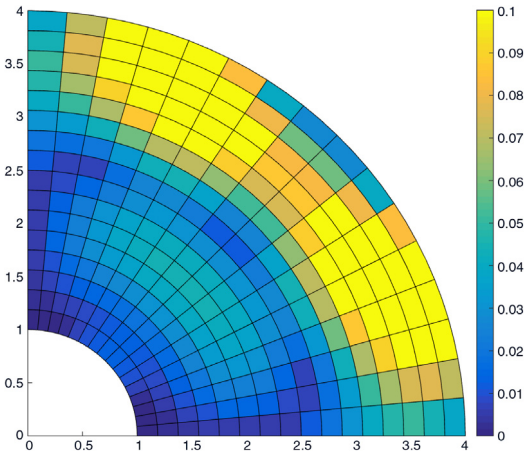

(d) SPR error estimator.

Fig. 28. Circular domain problem: Comparison of distribution of exact error vs. error estimator (at element level) obtained by Continuous L^2-projection (CL2P), Discrete least square fitting (DLSF) and Superconvergent patch recovery (SPR) for quadratic NURBS approximate solution u_h at step 2 of uniform refinement.

the DLSF handles homogeneous Dirichlet boundary conditions quite well but not non-homogeneous Dirichlet. We just remark that there exist remedies for handling the issues of boundary conditions for SPR [34,35].

7.3. Superconvergent gradient recovery for adaptive meshes

7.3.1. Example 4. (Smooth solution problem with non-homogeneous BC's on irregular meshes)

To investigate the significance of using computed superconvergent points (CSCP) compared to precomputed superconvergent points (PSCP) given in Table 3, we redo the *Smooth solution problem with non-homogeneous BC's* using quadratic LR B-splines defined on a set of arbitrary given irregular meshes as displayed in Fig. 33. In Tables 4–6, we report the obtained error norms as well as the effectivity indices θ^*. When using the PSCP points the DLSF and SPR give results in the range 0.75–0.96 and 0.80–1.02, respectively. Furthermore, we see that for all except second irregular mesh the effectivity index for SPR using PSCP points is in the range 0.96–1.02. The corresponding results when using CSCP points are 0.96–1.04 and 0.98–1.02 for DLSF and SPR, respectively. Thus, using CSCP points clearly improve the effectivity indices for both DLSF and SPR for the given problem. However, in practice when the meshes are refined in order to distribute the error equally among the elements we might expect

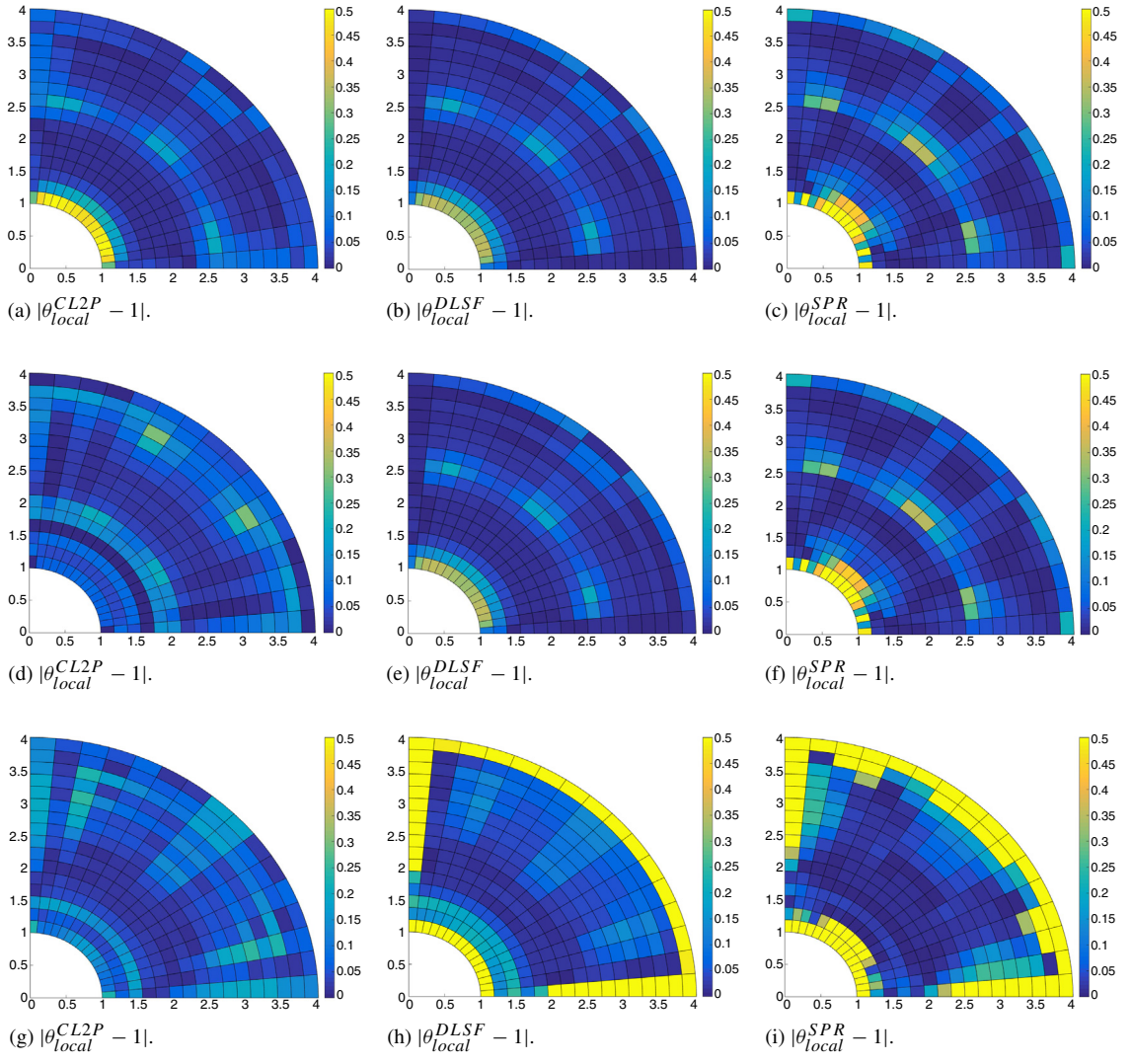

(a) $|\theta^{CL2P}_{local} - 1|$. (b) $|\theta^{DLSF}_{local} - 1|$. (c) $|\theta^{SPR}_{local} - 1|$.

(d) $|\theta^{CL2P}_{local} - 1|$. (e) $|\theta^{DLSF}_{local} - 1|$. (f) $|\theta^{SPR}_{local} - 1|$.

(g) $|\theta^{CL2P}_{local} - 1|$. (h) $|\theta^{DLSF}_{local} - 1|$. (i) $|\theta^{SPR}_{local} - 1|$.

Fig. 29. Circular domain problem: Comparison of deviation of local effectivity index $|\theta^{*}_{local} - 1|$ obtained by Continuous L^2-projection (CL2P), Discrete least square fitting (DLSF), and Superconvergent patch recovery (SPR) for NURBS (first row ($p = 2$), second row ($p = 3$), and third row ($p = 4$)) approximate solution u_h at step 2 of uniform refinement.

Table 4
Smooth solution problem with non-homogeneous BC's: Comparison of errors and effectivity index θ^{CL2P} for Continuous L^2 projection (CL2P) procedure on randomly generated irregular meshes of LR B-splines spaces.

Meshes	Exact error $\|\nabla u - \nabla u_h\|_{L^2(\Omega)}$	Projected error $\|\nabla u - \nabla u_h^{CL2P}\|_{L^2(\Omega)}$	Error estimate $\|\nabla u_h^{CL2P} - \nabla u_h\|_{L^2(\Omega)}$	Effectivity index θ^{CL2P}
irrMesh 1	1.56e−03	7.05e−04	1.41e−03	0.90
irrMesh 2	1.78e−03	1.27e−03	1.25e−03	0.70
irrMesh 3	9.17e−04	5.87e−04	7.09e−04	0.77
irrMesh 4	1.47e−03	4.66e−04	1.40e−03	0.95

less differences, and this issue is investigated below. Finally we remark that CL2P in general here gives less reliable effectivity indices.

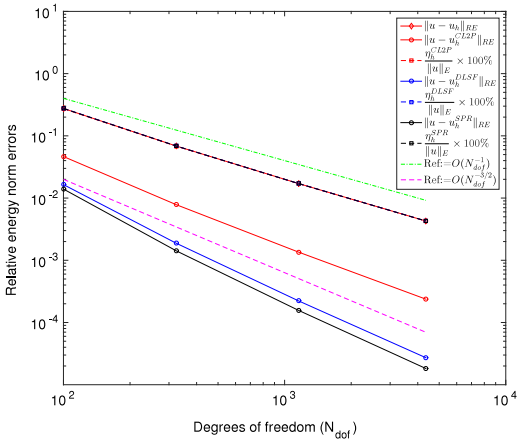

(a) Errors with quadratic splines.

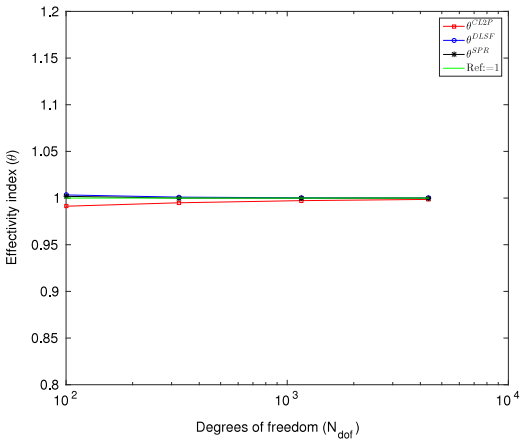

(b) Effectivity index with quadratic splines.

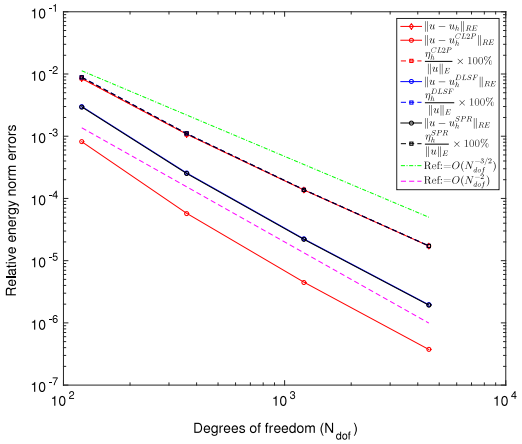

(c) Errors with cubic splines.

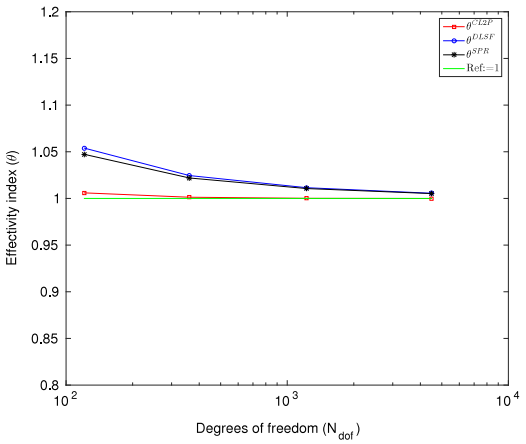

(d) Effectivity index with cubic splines.

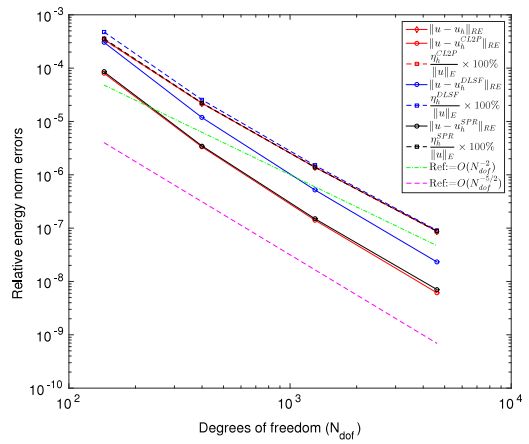

(e) Errors with quartic splines.

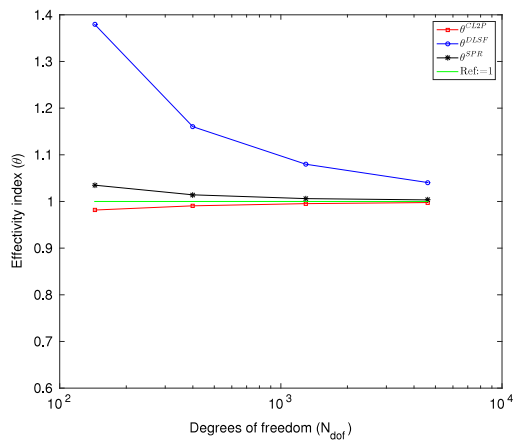

(f) Effectivity index with quartic splines.

Fig. 30. Smooth solution problem with non-homogeneous Dirichlet BC's: Errors and effectivity index results obtained with different recovery procedures (CL2P, DLSF, and SPR) using polynomial spline spaces of degrees $p = 2, 3, 4$ to approximate the solution u_h with uniform h-refinement.

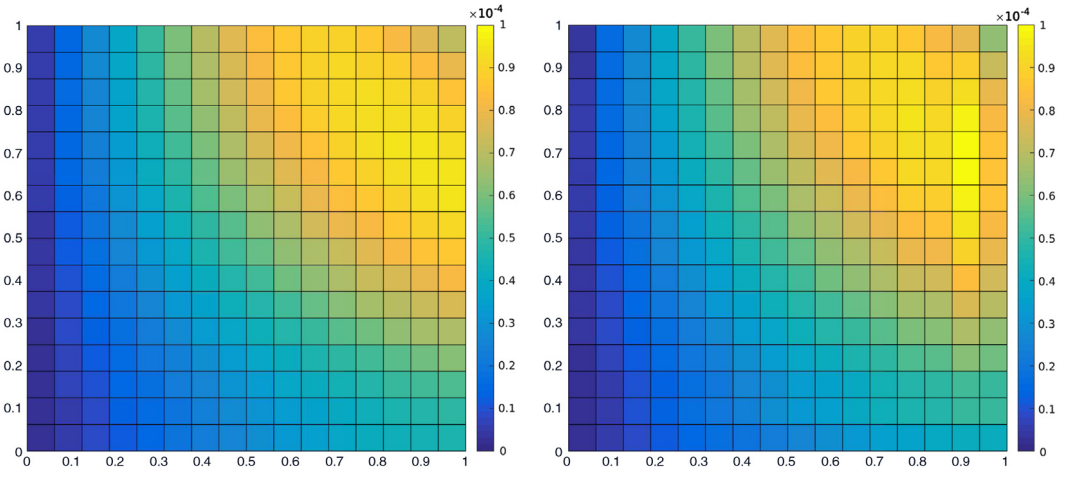

(a) Exact error distribution.

(b) CL2P error estimator.

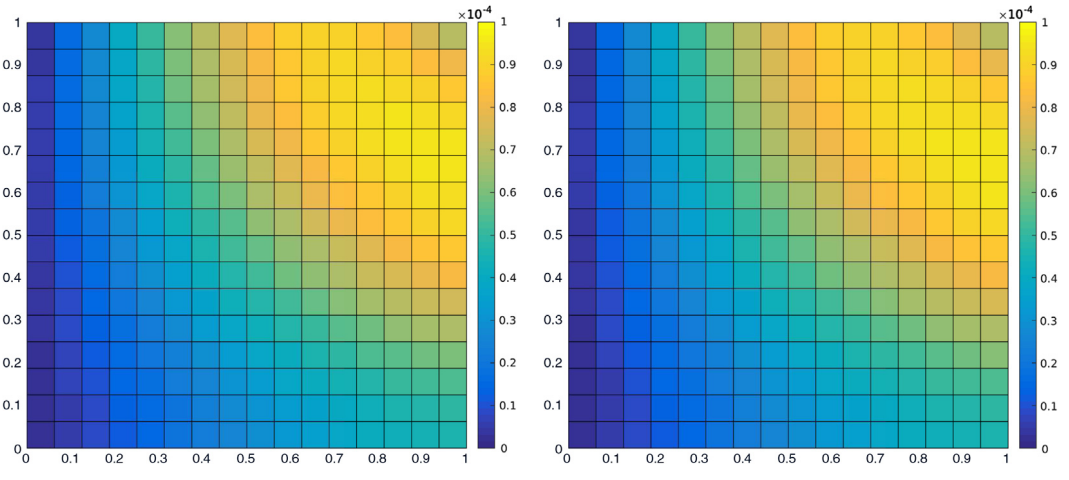

(c) DLSF error estimator.

(d) SPR error estimator.

Fig. 31. Smooth solution problem with non-homogeneous Dirichlet BC's: Comparison of distribution of exact error vs. error estimator (at element level) obtained by Continuous L^2-projection (CL2P), Discrete least square fitting (DLSF), and Superconvergent patch recovery (SPR) for quadratic B-splines approximate solution u_h at step 2 of uniform refinement.

Table 5
Smooth solution problem with non-homogeneous BC's: Comparison of errors and effectivity index θ^{DLSF} for Discrete least square fitting (DLSF) procedure on randomly generated irregular meshes of LR B-splines spaces.

Meshes	Sampling points	Exact error $\|\nabla u - \nabla u_h\|_{L^2(\Omega)}$	Projected error $\|\nabla u - \nabla u_h^{DLSF}\|_{L^2(\Omega)}$	Error estimate $\|\nabla u_h^{DLSF} - \nabla u_h\|_{L^2(\Omega)}$	Effectivity index θ^{DLSF}
irrMesh	PSCP	1.56e−03	5.59e−04	1.43e−03	0.92
1	CSCP		3.02e−04	1.57e−03	1.01
irrMesh	PSCP	1.78e−03	8.74e−04	1.35e−03	0.75
2	CSCP		2.44e−04	1.71e−03	0.96
irrMesh	PSCP	9.17e−04	4.89e−04	7.25e−04	0.79
3	CSCP		2.88e−04	9.55e−04	1.04
irrMesh	PSCP	1.47e−03	4.12e−04	1.41e−03	0.95
4	CSCP		3.40e−04	1.42e−03	0.96

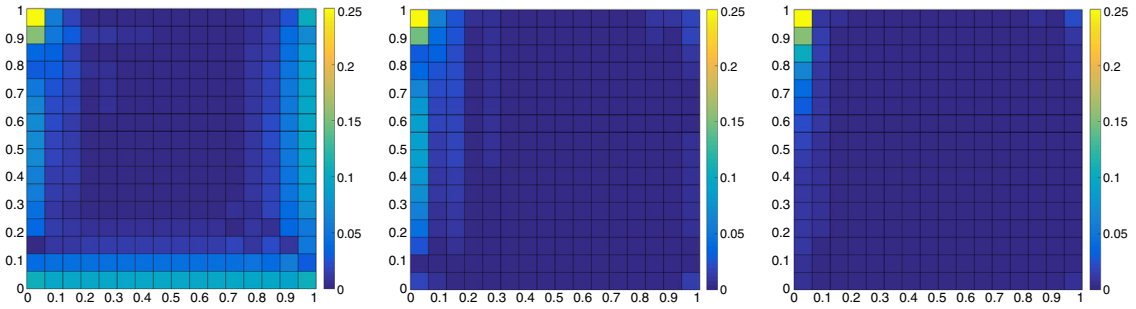

(a) $|\theta_{local}^{CL2P} - 1|$. (b) $|\theta_{local}^{DLSF} - 1|$. (c) $|\theta_{local}^{SPR} - 1|$.

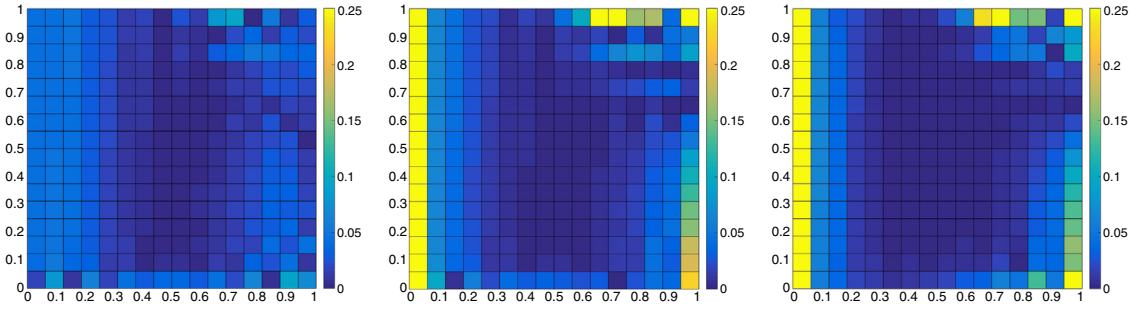

(d) $|\theta_{local}^{CL2P} - 1|$. (e) $|\theta_{local}^{DLSF} - 1|$. (f) $|\theta_{local}^{SPR} - 1|$.

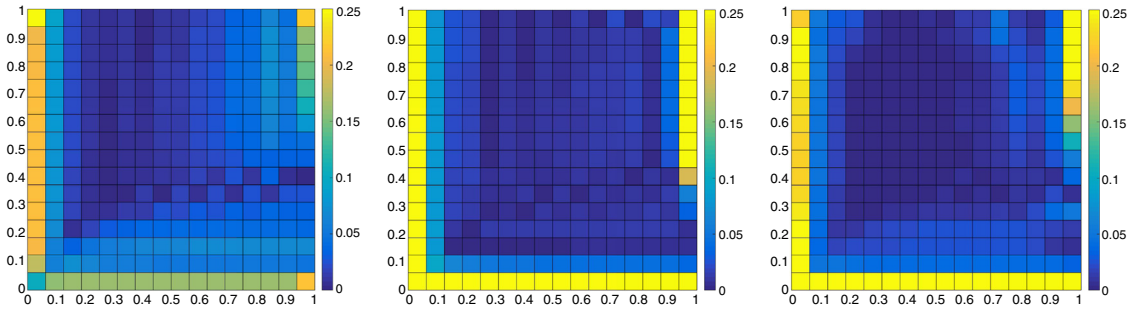

(g) $|\theta_{local}^{CL2P} - 1|$. (h) $|\theta_{local}^{DLSF} - 1|$. (i) $|\theta_{local}^{SPR} - 1|$.

Fig. 32. Smooth solution problem with non-homogeneous Dirichlet BC's: Comparison of deviation of local effectivity index $|\theta_{local}^{*} - 1|$ obtained by Continuous L^2-projection (CL2P), Discrete least square fitting (DLSF), and Superconvergent patch recovery (SPR) for NURBS (first row ($p = 2$), second row ($p = 3$), and third row ($p = 4$)) approximate solution u_h at step 2 of uniform refinement.

Table 6
Smooth solution problem with non-homogeneous BC's: Comparison of errors and effectivity index θ^{SPR} for Superconvergent patch recovery (SPR) procedure on randomly generated irregular meshes of LR B-splines spaces.

Meshes	Sampling points	Exact error $\|\nabla u - \nabla u_h\|_{L^2(\Omega)}$	Projected error $\|\nabla u - \nabla u_h^{SPR}\|_{L^2(\Omega)}$	Error estimate $\|\nabla u_h^{SPR} - \nabla u_h\|_{L^2(\Omega)}$	Effectivity index θ^{SPR}
irrMesh	PSCP	1.56e−03	5.48e−04	1.52e−03	0.97
1	CSCP		4.21e−04	1.59e−03	1.01
irrMesh	PSCP	1.78e−03	9.45e−04	1.44e−03	0.80
2	CSCP		2.77e−04	1.75e−03	0.98
irrMesh	PSCP	9.17e−04	2.92e−04	8.85e−04	0.96
3	CSCP		9.61e−05	9.17e−04	1.00
irrMesh	PSCP	1.47e−03	3.84e−04	1.50e−03	1.02
4	CSCP		3.07e−04	1.51e−03	1.02

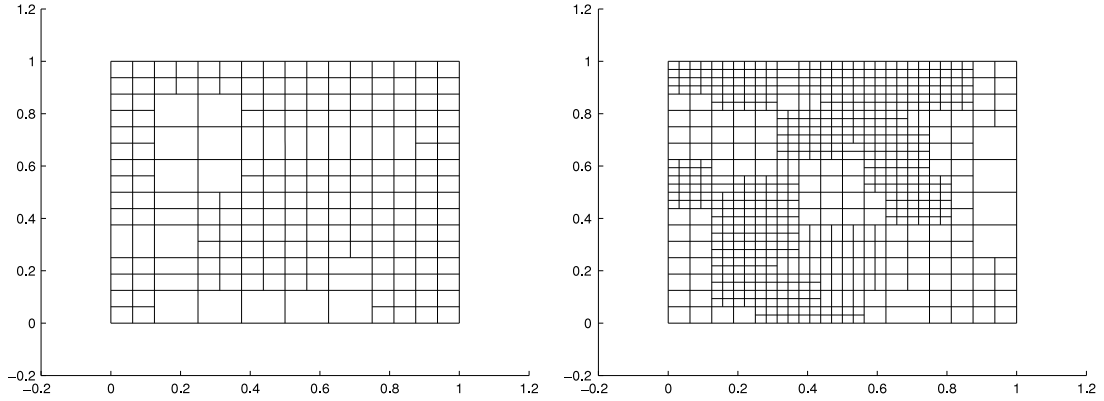

(a) irrMesh 1, N_{DOF} 250.

(b) irrMesh 2, N_{DOF} 612.

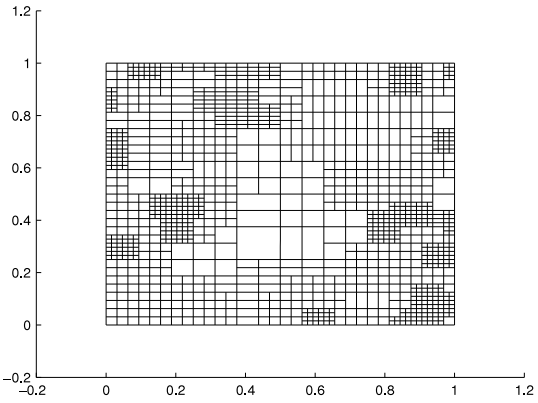

(c) irrMesh 3, N_{DOF} 1173.

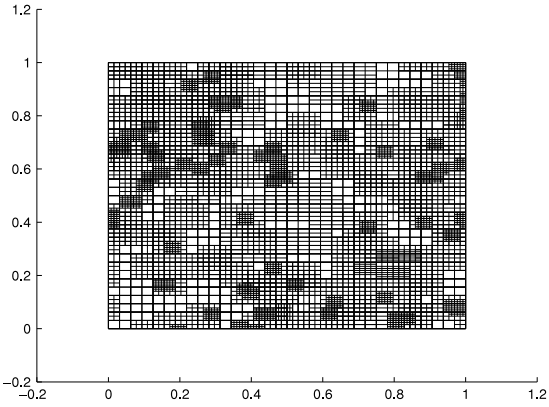

(d) irrMesh 4, N_{DOF} 1785.

Fig. 33. Smooth solution problem with non-homogeneous Dirichlet BC's on irregular meshes: A set of randomly generated irregular meshes for quadratic LR B-spline elements.

Table 7
Smooth solution problem with non-homogeneous BC's: Effectivity index θ^* for Continuous L^2-projection (CL2P), Discrete least square fitting (DLSF), and Superconvergent patch recovery (SPR) procedures using PSCP and CSCP points on adaptive meshes of Fig. 34.

Steps	θ^{CL2P}	θ^{DLSF} PSCP	θ^{DLSF} CSCP	θ^{SPR} PSCP	θ^{SPR} CSCP
1	0.99	1.00	1.00	1.02	1.02
3	0.99	0.99	1.00	1.01	1.02
5	0.96	0.97	1.00	0.99	1.00
7	0.99	0.99	1.00	1.00	1.01

7.3.2. Example 5. (Smooth solution problem with non-homogeneous BC's on adaptive meshes)

To investigate the significance of using CSCP points compared to PSCP points as given in Table 3 on realistic adapted meshes based on exact error distribution (see Fig. 34) we redo the *Smooth solution problem with non-homogeneous BC's* using quadratic LR B-splines. In Table 7 we report the obtained effectivity indices θ^* for different recovery procedures. When using the PSCP points the DLSF and SPR give results in the range 0.97–1.00 and 0.99–1.02, respectively. The corresponding results when using CSCP points are 1.00–1.00 and 1.00–1.02 for DLSF and SPR, respectively. Thus, using CSCP points again improve the effectivity indices for both DLSF and SPR, but only marginally. However, as seen from Fig. 35 the use of CSCP points within DLSF and SPR slightly lower the

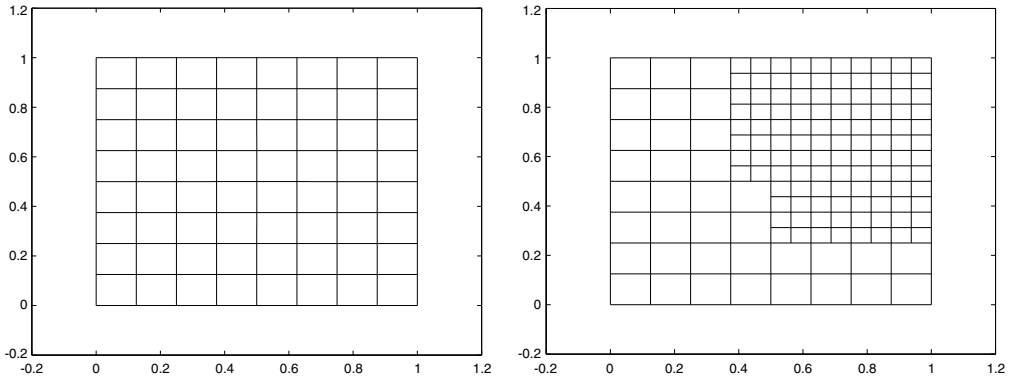

(a) Step 1, N_{DOF} 100.

(b) Step 3, N_{DOF} 294.

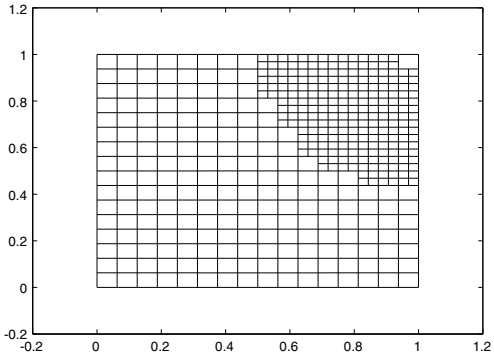

(c) Step 5, N_{DOF} 716.

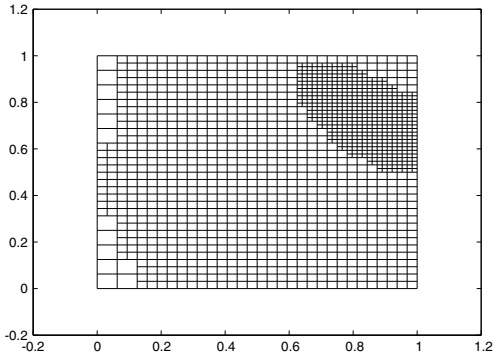

(d) Step 7, N_{DOF} 1447.

Fig. 34. Smooth solution problem with non-homogeneous BC's on adapted meshes: Meshes obtained by means of adaptive refinement based on exact error estimate and the use of LR B-splines.

error in recovered gradients as well as make the error estimates slightly more conservative. Finally, we remark that CL2P in general again gives less reliable effectivity indices (0.96–0.99), but this time fairly close to one.

On comparing the results obtained on these practical adapted meshes with the results obtained for irregular set of meshes shown in Fig. 33, we see that the results using CSCP points are better, i.e., the effectivity indices obtained on these practical meshes is close to unity and approaching to unity in h-asymptotic sense. Notice that the number of elements in the close neighborhood of change in element size h is much less for the adapted meshes compared to the irregular meshes. As shown in Fig. 21(c) the location of computed superconvergent points (CSCP) will differ with PSCP only for elements nearby the change of element size h, i.e., PSCP and CSCP will be different only for those elements nearby the interface.

7.3.3. Example 6. (Circular wave front problem on adaptive meshes)

The above case was studied for the problem with smooth solution. Now we consider a problem with *rough right hand side* which exhibits internal layer behavior.

The governing equation for the elliptic problem is

$$-\Delta u = f \quad \text{in } \Omega, \tag{134}$$

with the boundary condition

$$u = g \quad \text{on } \partial\Omega. \tag{135}$$

Here $\Omega = (0, 1)^2$ is a square domain and f, g are constructed to correspond to the exact solution

$$u(x, y) = \arctan(S(r - r_0)), \text{ where } r = \sqrt{(x - 1/2)^2 + (y - 1/2)^2} \tag{136}$$

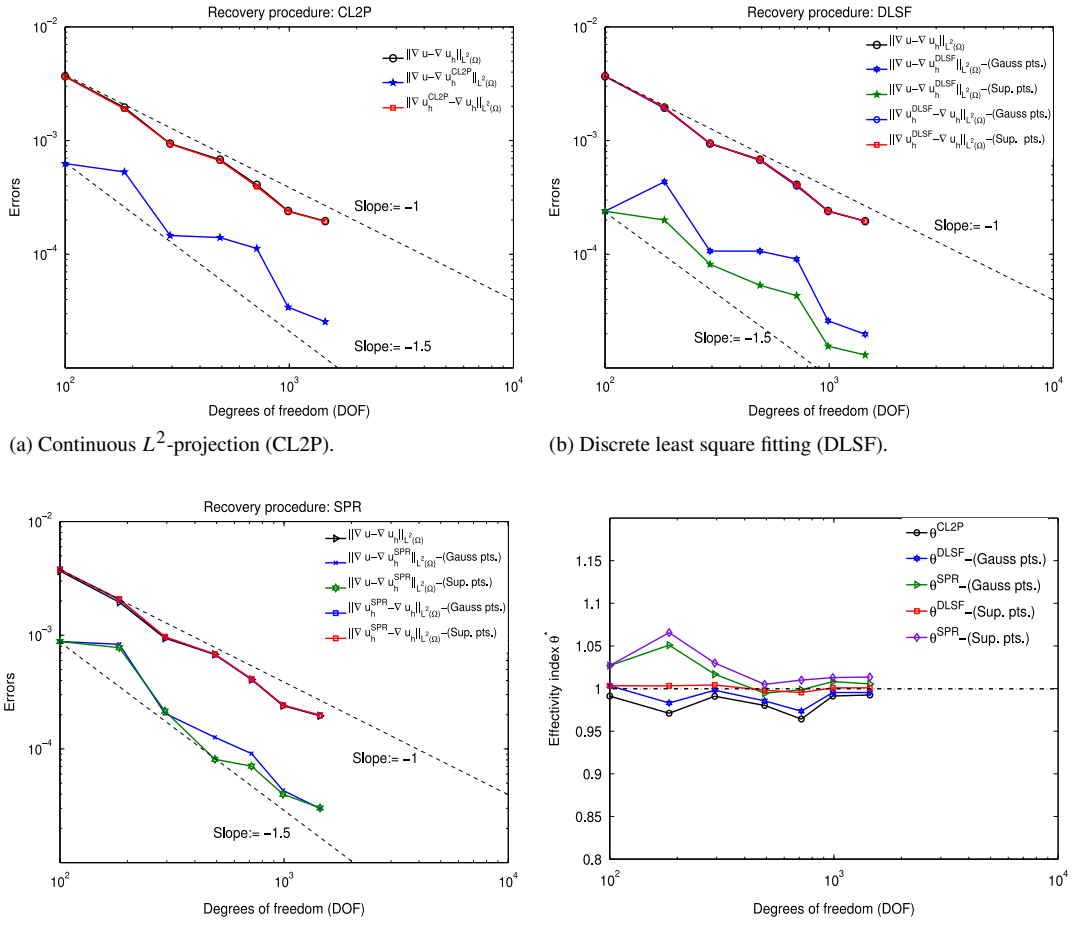

(a) Continuous L^2-projection (CL2P).

(b) Discrete least square fitting (DLSF).

(c) Superconvergent patch recovery (SPR).

(d) Effectivity index θ^*.

Fig. 35. Smooth solution problem with non-homogeneous BC's on adapted meshes: Comparison of error plots and effectivity index by Continuous L^2-projection (CL2P), Discrete least square fitting (DLSF), and Superconvergent patch recovery (SPR) using PSCP and CSCP points in adaptive isogeometric analysis using quadratic LR B-splines based on exact error estimator.

with $r_0 = 1/16$ is the distance from the wave front to the center of the circle, and $S = 20$ gives a mild steepness of the wave front along the circular region in the interior of the domain Ω.

The comparison of the performance of the error estimators on a set of quasi-uniform meshes obtained via the adaptive refinement algorithm using exact error estimate with structured mesh refinement strategy of LR B-splines of degree $p = 2$ are presented in Figs. 36 and 37. The results with respect to two choices of sampling points, i.e., PSCP and CSCP points, for DLSF and SPR procedures are also given in Table 8. It can be seen from the figures that both choices of sampling points in our recovery procedures give good effectivity indices and provide h-asymptotic results as expected. However, the use of CSCP points again provides slightly better accuracy and convergence in the recovered gradient field and slightly faster asymptotic exactness results.

7.4. Adaptive isogeometric analysis using a posteriori error estimators

In this section, we demonstrate the performance of developed recovery based error estimators in adaptive isogeometric analysis, in particular, we show that the developed SPR procedure does produce adaptive meshes on which the recovered gradient is indeed superconvergent of order $\delta \in (0, 1]$. We present the numerical results with respect to each developed recovery based error estimator $\eta^* = \|\nabla u_h^* - \nabla u_h\|_{L^2(\Omega)}$, with $* =$ CL2P, DLSF, SPR, using LR B-spline based structured mesh refinement algorithm. The significance of using CSCP and PSCP as sampling points in DLSF and SPR procedures has been investigated in Section 7.3. From numerical results we noticed that the

Table 8
Circular wave front problem: Effectivity index θ^* for Continuous L^2-projection (CL2P), Discrete least square fitting (DLSF), and Superconvergent patch recovery (SPR) procedures using PSCP and CSCP points on adaptive meshes of Fig. 36.

Steps	θ^{CL2P}	θ^{DLSF} PSCP	θ^{DLSF} CSCP	θ^{SPR} PSCP	θ^{SPR} CSCP
1	1.63	1.67	1.67	2.24	2.24
3	0.98	1.00	1.06	1.28	1.35
7	0.96	0.99	1.00	1.04	1.05
10	0.98	0.99	1.00	1.01	1.01

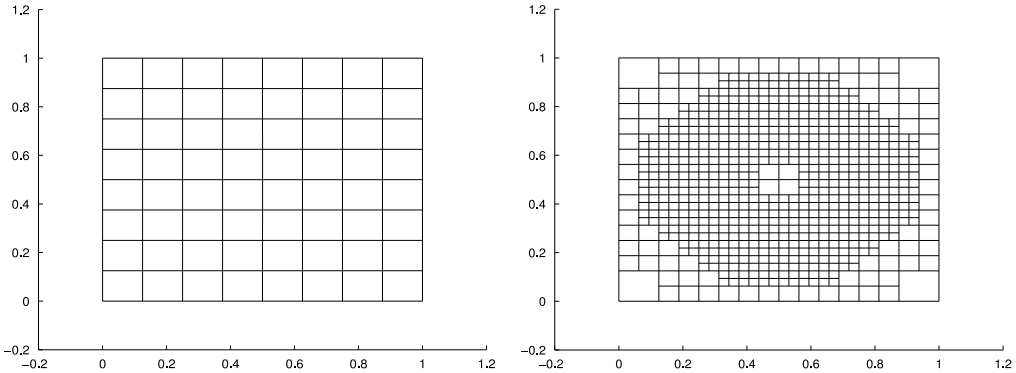

(a) Step 1, N_{DOF} 100.

(b) Step 3, N_{DOF} 688.

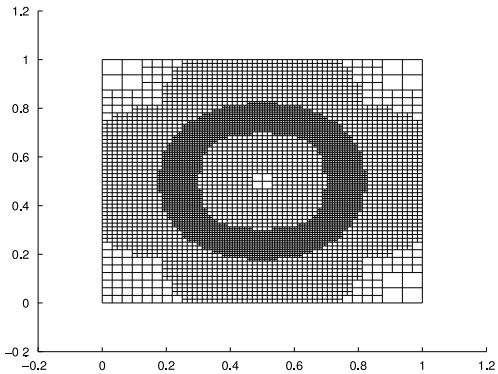

(c) Step 5, N_{DOF} 5880.

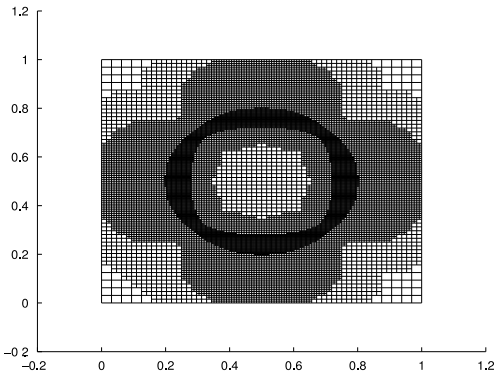

(d) Step 7, N_{DOF} 16809.

Fig. 36. Circular wave front problem: Meshes obtained by means of adaptive refinement based on exact error estimate and the use of LR B-splines at different steps.

choice of CSCP is *in general* better than using PSCP in recovery procedures. There is also computational cost involved with the choice of CSCP, alternative to which is PSCP that gives slightly less accurate but very comparable results on adaptive meshes generated with LR B-splines refinement algorithm based on a posteriori error estimator. Thus we propose a cost effective a posteriori error estimation technique which consider the IGA-SPR procedure defined in Section 7.1 with the choice of PSCP. The results obtained by CSCP is in general better, i.e., one may consider the presented results below to represent the ”worst case”. The aim here is to verify the performance of IGA-SPR in solving elliptic problems with internal layer and non-smooth solutions using adaptive isogeometric analysis.

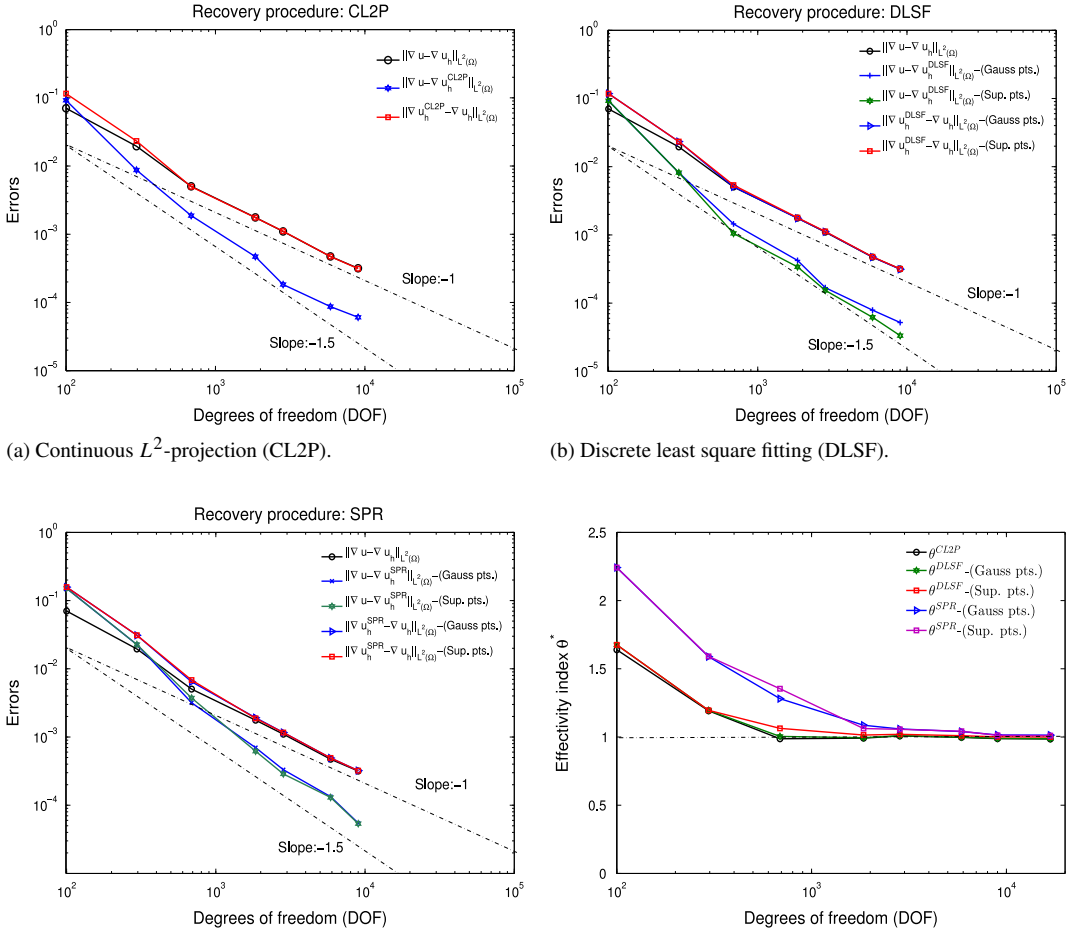

(a) Continuous L^2-projection (CL2P).

(b) Discrete least square fitting (DLSF).

(c) Superconvergent patch recovery (SPR).

(d) Effectivity index θ^*.

Fig. 37. Circular wave front problem: Comparison of error plots and effectivity index by Continuous L^2-projection (CL2P), Discrete least square fitting (DLSF), and Superconvergent patch recovery (SPR) using PSCP and CSCP points in adaptive isogeometric analysis using quadratic LR B-splines based on exact error estimator.

7.4.1. Example 7. (Internal layer problem)

The governing equation of the internal layer problem is

$$-\Delta u = f \quad \text{in } \Omega := (0,1)^2, \tag{137}$$

with the boundary conditions

$$u = u_d \quad \text{on } \Gamma_D \quad \text{and} \quad \frac{\partial u}{\partial n} = g \quad \text{on } \Gamma_N. \tag{138}$$

Here the boundary data u_d, g and f are constructed to correspond to the exact solution

$$u(x,y) = \arctan\left(S\left(\sqrt{x^2+y^2} - 0.60\right)\right). \tag{139}$$

We consider the problem with $S = 60$ in the exact solution u, which exhibits the curved internal layer of width $O(1/60)$ in interior of the domain. The set up of the problem with given boundary conditions and the exact solution u are shown in Fig. 38.

The comparison of error plots and effectivity index of different recovery procedures using SPR based error estimator for degree $p = 2, 3$ LR-B splines are shown Fig. 39. The results obtained for the error in projected field are

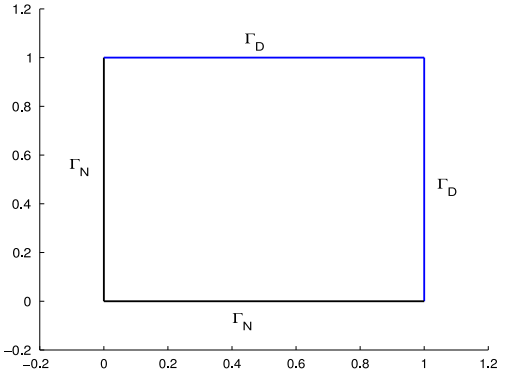

(a) Internal layer problem description.

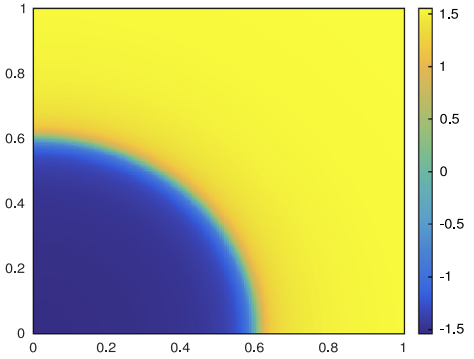

(b) Exact solution u.

Fig. 38. Internal layer problem: Problem description and exact solution u.

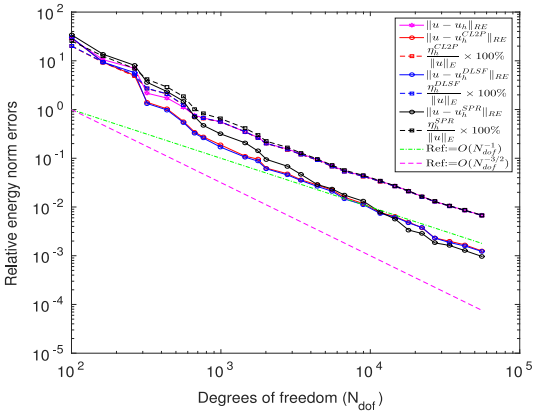

(a) Errors with quadratic LR B-splines.

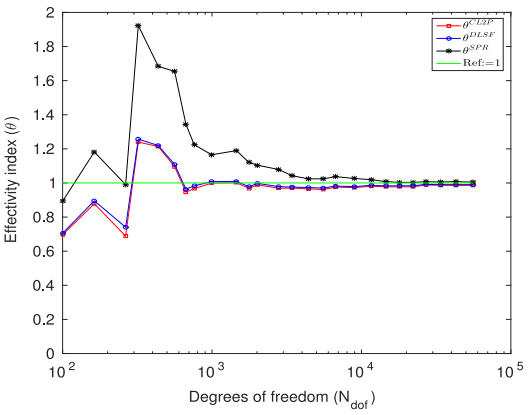

(b) Effectivity index with quadratic LR B-splines.

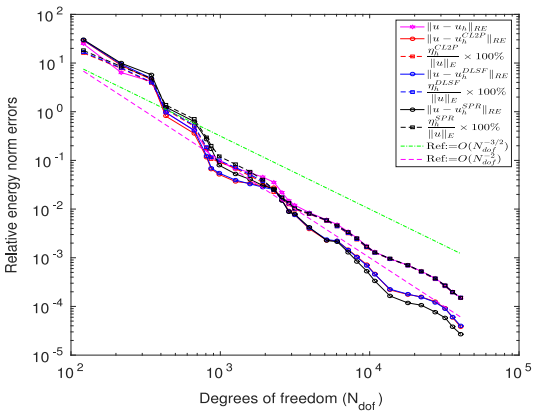

(c) Errors with cubic LR B-splines.

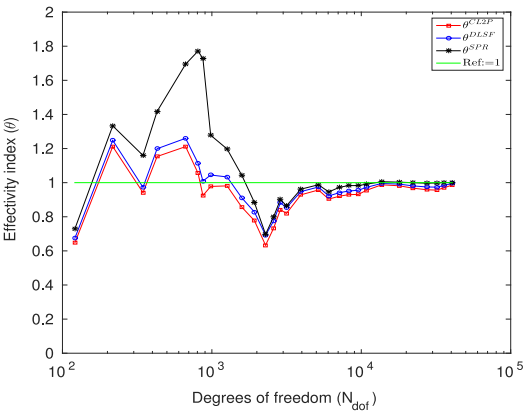

(d) Effectivity index with cubic LR B-splines.

Fig. 39. Internal layer problem: Error plots and effectivity index for different recovery based a posteriori error estimators in adaptive isogeometric analysis using quadratic and cubic LR B-splines in first and second row, respectively.

quite comparable between the different recovery procedures for both degrees $p = 2, 3$. With SPR we obtain higher rate of convergence in projected error in comparison to the two other recovery procedures, while the results for CL2P and DLSF is initially more accurate than the SPR. We also obtain the asymptotic exactness for all the recovery based error estimators, see Fig. 39(b), (d).

This problem exhibits an internal layer of width $O(1/60)$ due to the rough right hand side function f. In order to obtain optimal convergence rate, i.e., $O(h^{p+1})$, the internal layer has to be resolved. For uniform refined meshes this means when $h < 1/60$. Starting with $h = 1/8$ it means 3 uniform mesh refinement steps resulting in $h = 1/64$ which is about $N_{DOF} = 66^2 = 4356$ degrees of freedom for degree $p = 2$ case. Using the developed a posteriori error estimates for degree $p = 2$ we start to resolve the internal layer after 6 adaptive refinement steps where $h_{max} = 1/8$ and $h_{min} = 1/64$ with approximately $N_{DOF} = 800$ degrees of freedom. The resolving of the internal layer after 6 refinement steps for quadratic case is seen from the fact that the effectivity indices are starting converging to 1 at this stage in the adaptive process, see Fig. 39(b). The observed behavior of the SPR-procedure for coarse meshes i.e., before the internal layer is properly resolved complies well with other investigations, see e.g., [32,34]. The SPR-procedure works well when we have smooth error distribution throughout the mesh. Thus, for non-smooth problems the SPR-procedure can only give good effectivity indices after some initial refinement steps that get rid of any pollution error present. All known experience from more than two decades of use of SPR-procedures has shown that adaptive finite element methods based on SPR error estimates are able to achieve smooth error distribution for non-smooth problems having singularity points/lines or rough right hand sides.

The comparison of the deviation in local effectivity index for these recovery procedures at various steps are presented in Fig. 41 for degree $p = 2$. The results for degree $p = 3$ show similar behavior. We observe that the three different recovery procedures not only give good global effectivity indices but it also show that the local effectivity index at element level is fairly close to one. However, along the boundary the results for SPR are less accurate than the other two methods. This complies with the observation done in earlier examples described above. The results presented in Fig. 41 show that the recovery procedures capture very well the location of the internal layer and the numerical solution based on adaptive refinement using these error estimates all attain optimal rate of convergence for degrees $p = 2, 3$, see Fig. 39. The corresponding adaptive meshes obtained at different refinement steps are shown in Fig. 40.

7.4.2. Example 8. (L-shaped domain problem)

The governing equation of L-shaped domain problem is

$$\Delta u = 0 \quad \text{in } \Omega, \tag{140}$$

with the boundary conditions

$$u = 0 \quad \text{on } \Gamma_D \quad \text{and} \quad \frac{\partial u}{\partial n} = g \quad \text{on } \Gamma_N. \tag{141}$$

Here $\Omega = (-1, 1)^2 \setminus (0, 1) \times (-1, 0)$ is a L-shape domain and g is constructed to correspond to the exact solution

$$u(x, y) = r^{\frac{2}{3}} \sin\left(\frac{2\theta}{3}\right), \quad \text{with } r = (x^2 + y^2)^{\frac{1}{2}}, \quad \theta = \tan^{-1}\left(\frac{y}{x}\right). \tag{142}$$

The set up of the problem with given boundary conditions and the exact solution u are shown in Fig. 42.

For the given elliptic problem, re-entrant corner at the origin $(0, 0)$ in the domain cause a singularity in the solution. It is known that the convergence for uniform mesh refinement is limited by the strength of the singularity, i.e., the convergence rate (versus degrees of freedoms) is equal to $-1/3$. For problems where the solution is not sufficiently smooth, $u \notin H^{p+1}(\Omega)$, as is the case for the L-shaped domain problem that has a singularity point at its boundary, we do not obtain optimal convergence rate when we do uniform mesh refinement. In particular, the use of high order polynomials is then inefficient.

The error plots and effectivity index of different recovery procedures using SPR based error estimator for LR B-splines of degrees $p = 2, 3$ are shown Fig. 43. The results show that the recovery procedures achieve the superconvergence behavior in the projected field on adaptive generated meshes for degree $p = 2$, while for degree $p = 3$ the projected error is less in comparison to the exact error for all the recovered gradients. The DLSF and CL2P procedures give a more accurate recovered field than the SPR in the initial steps of the adaptive refinement. After few step of initial refinement the projected error shows superconvergence behavior and at the end of the refinement process the SPR procedure have a slightly higher convergence rate than DLSF and CL2P, see Fig. 43(a). It should be noted from Fig. 43(a) that for degree $p = 2$, when we achieved optimal rate of convergence in the exact error after 12 steps

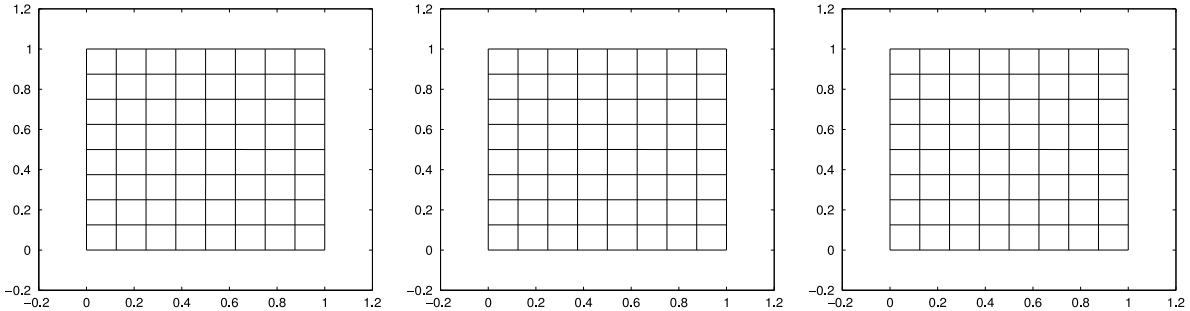

(a) Step 1, N_{DOF} 100. (b) Step 1, N_{DOF} 100. (c) Step 1, N_{DOF} 100.

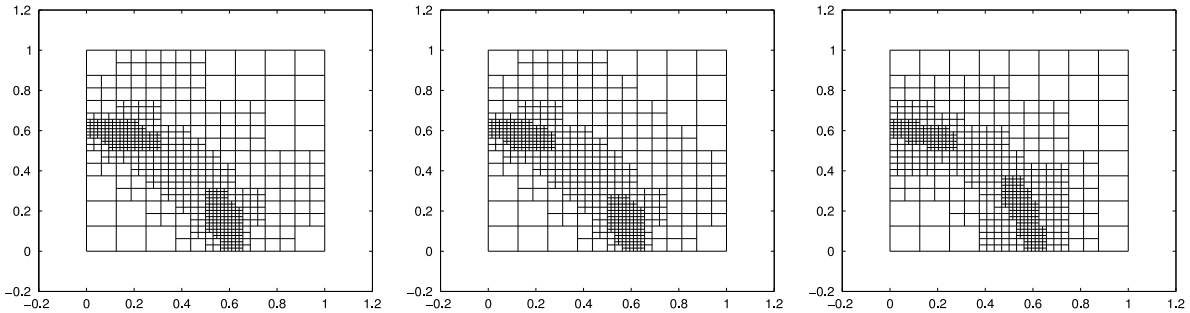

(d) Step 6, N_{DOF} 591. (e) Step 6, N_{DOF} 583. (f) Step 6, N_{DOF} 601.

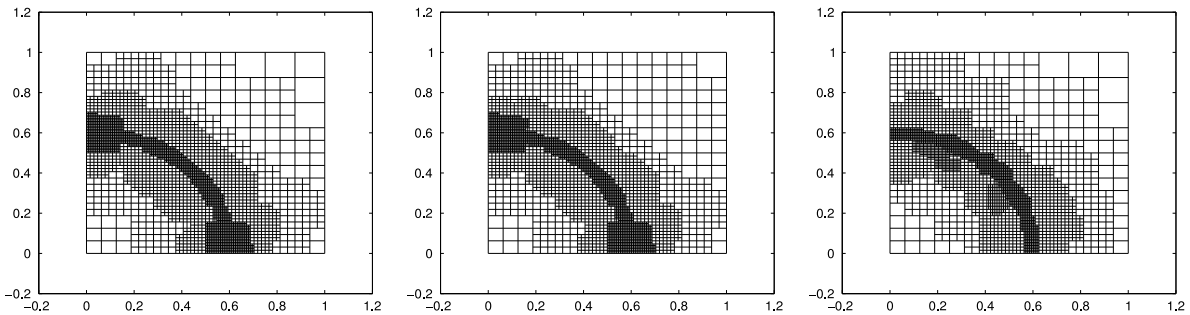

(g) Step 12, N_{DOF} 3072. (h) Step 12, N_{DOF} 3094. (i) Step 12, N_{DOF} 2660.

Fig. 40. Internal layer problem: Adapted LR meshes obtained via adaptive LR B-splines refinement algorithm for degree $p = 2$ using different recovery based error estimators at different refinement steps for Internal layer problem. The columns from left to right represent the cases with respect to Continuous L^2-projection (CL2P), Discrete least square fitting (DLSF), and Superconvergent patch recovery (SPR), respectively.

of adaptive refinement (as before these steps the rate of convergence was more than 2) a higher rate of convergence close to 3 in the recovered gradient field is clearly visible. While for degree $p = 3$, the error plots in Fig. 43(c) show that the exact error and the projected errors are converging with a rate close to 4, which is higher than its optimal rate of convergence for degree 3. The effectivity index plots given in Fig. 43(b), (d) show that the effectivity index for the SPR procedure for degrees $p = 2, 3$ is very close to 1 and show asymptotic exactness behavior, while for the DLSF and CL2P recovery procedures the effectivity index value is with a good range of $1 - 1.2$ close to 1 and for the case of degree $p = 2$ converges to 1 in h-asymptotic exactness sense, while for $p = 3$ remains bounded from above for these results.

Regarding the ability to capture the error distribution, the behavior of the local element effectivity indices are shown in Fig. 45 for degree $p = 2$ (the result are similar for $p = 3$). We observe from Fig. 45 that the three different recovery procedures not only give good global effectivity indices but it also show the local effectivity index at element level is fairly close to one. However, along the boundary the results for SPR are again less accurate than the other two methods. In any case all the recovery procedure capture very well the singularity in the solution at the re-entrant

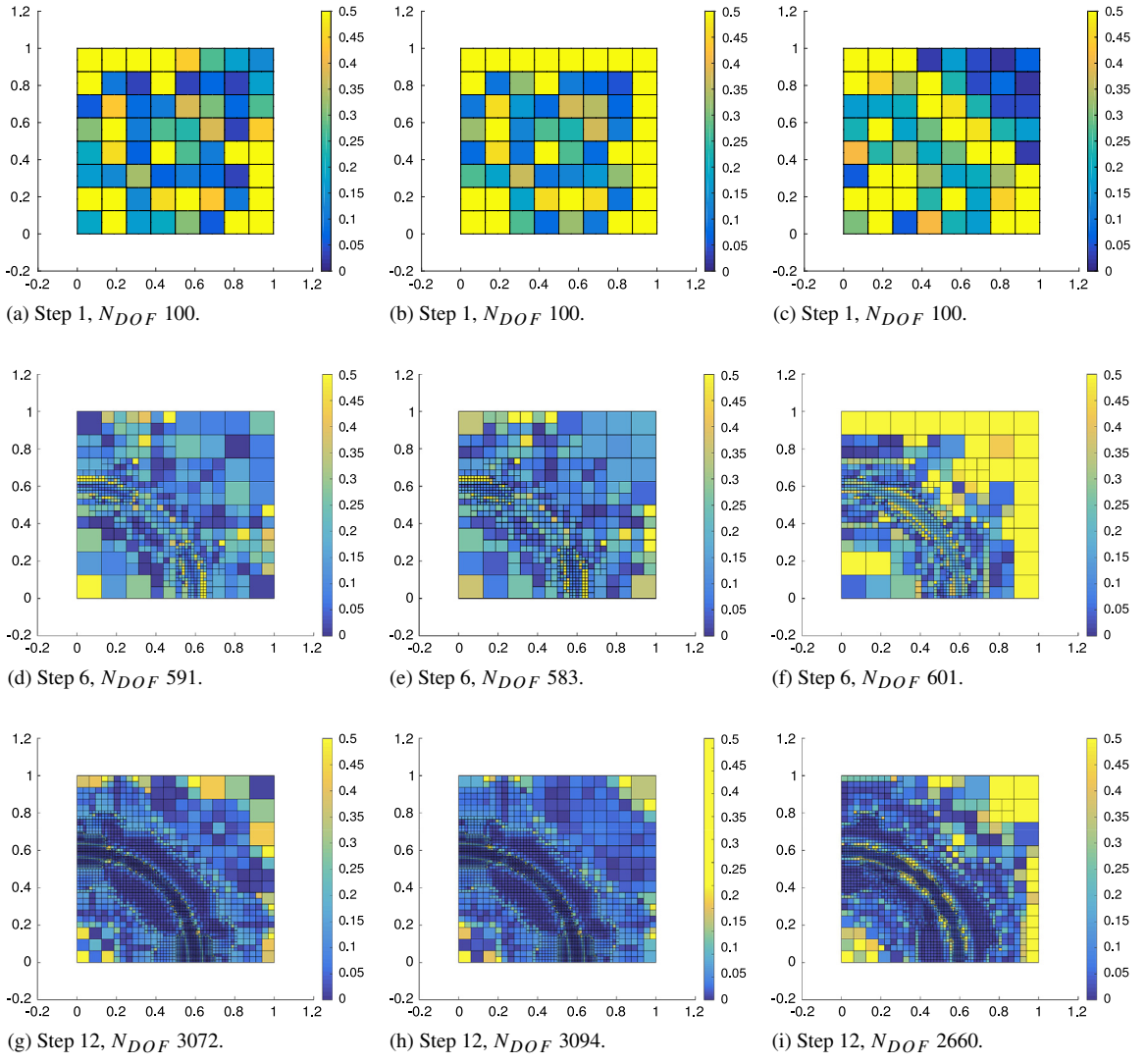

(a) Step 1, N_{DOF} 100. (b) Step 1, N_{DOF} 100. (c) Step 1, N_{DOF} 100.

(d) Step 6, N_{DOF} 591. (e) Step 6, N_{DOF} 583. (f) Step 6, N_{DOF} 601.

(g) Step 12, N_{DOF} 3072. (h) Step 12, N_{DOF} 3094. (i) Step 12, N_{DOF} 2660.

Fig. 41. Internal layer problem: Comparison of absolute value of the deviation effectivity index at element level $|1-\theta^*_{el}|$ at LR meshes obtained via adaptive LR B-splines refinement algorithm for degree $p=2$ using different recovery based error estimators at different refinement steps for Internal layer problem. The columns from left to right represent the cases with respect to Continuous L^2-projection (CL2P), Discrete least square fitting (DLSF) and Superconvergent patch recovery (SPR), respectively.

corner and the numerical solution based on adaptive refinement using these error estimates all attain optimal rate of convergence. The corresponding adaptive meshes obtained at different refinement steps are shown in Fig. 44.

Remark 7.1. We would like to underline the very high quality of the obtained effectivity indices obtained herein for SPR compared to earlier experience with SPR and unstructured adaptive mesh refinement of linear finite elements, see e.g. [34]. Fig. 17b in [34] shows an effectivity index for the SPR-procedure in the range of (0.65–0.8) for $N_{DOF} < 1000$, whereas we herein achieve effectivity indices in the range (0.96–1.04) for the L-shaped domain problem.

Computational cost

Regarding the computational cost for the IGA-SPR-procedure we notice that it grows linearly with the number of basis functions (i.e., N_{DOF}). Thus, compared to the computational time for solving the global IGA finite element system of equations (e.g. for direct sparse solvers the computational cost is of order N^{γ}_{DOF}, with $\gamma \geq 1.5$), this cost will be relatively smaller the larger the system (i.e., N_{DOF}) is. Our current implementation is done in Matlab and is not optimized regarding computational costs. However, earlier experience with SPR-procedures for classical finite

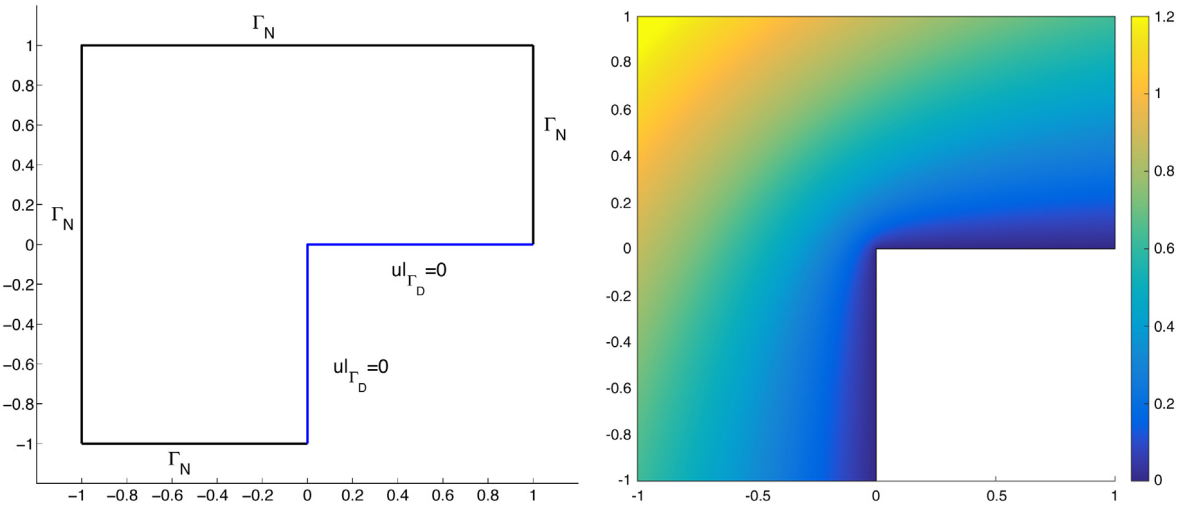

(a) L-shaped problem description. (b) Exact solution u.

Fig. 42. L-shaped problem: Problem description and exact solution u.

element method implemented both in Fortran and C++ show that the post-processing consumes less than 10% of the time spent by the IGA itself, for relatively moderate sized problems [83]. In case of parallel computers we notice that IGA-SPR procedure may utilize massively parallel processors as well as GPU-architecture very efficiently, as the local least square equation systems that have to be solved for each basis function are disjoint. The computational cost for the global recovery procedures CL2P and DLSF will be similar to the cost of computed IGA solution.

8. Concluding remarks

This article addresses adaptive methods for isogeometric analysis based on local refinement using LR B-splines, guided by recovery based a posteriori error estimates. The present approach integrates the following main concepts in order to achieve an accurate, effective and reliable adaptive methodology for isogeometric analysis:

1. *Precomputed superconvergent points (PSCP) for uniform meshes:* The location of superconvergent points (for the derivative) for smooth problems (i.e., with no pollution) and meshes with certain restrictions (e.g., locally symmetric) is determined following the ideas introduced by Walhbin [72].
2. *Computation of true superconvergent points (CSCP) for non-uniform meshes:* Non-uniform meshes are handled by means of local patchwise computations for localization of the superconvergent points inspired by ideas set forth by Babuška [69] and co-workers developed for classical finite elements.
3. *Consistent superconvergent patch recovery operator:* Recovery of superconvergent derivatives, by means of solving equations on local patches, is achieved using recovery operators that fulfills the consistency requirement prescribed by Ainsworth and Craig [75].
4. *Structured mesh refinement using LR B-splines:* Adaptive meshes that are locally tensorial and symmetrical (away from the region where one has changes in element sizes) are achieved by combining uniform knot-vectors and local refinement according to the concept of structured mesh refinement using LR B-splines, as introduced by Johannessen, Kvamsdal and Dokken [8].
5. *Recovery based a posteriori error estimation:* Asymptotic exact energy error estimate is achieved by computing the L_2 norm of the difference between the superconvergent recovered gradient and the computed isogeometric finite element gradient.

One main finding from the study performed herein is that a posteriori error estimation based on the concept of superconvergent patch recovery is very well suited for driving adaptive isogeometric analyses using local structured mesh refinement of a (nearly) uniform initial tensorial mesh.

The superconvergence property relies on smooth error distribution (i.e., pollution error is under control) and restrictions (local symmetry) on the meshes. For non-smooth problems, e.g., problems with singularity at points along

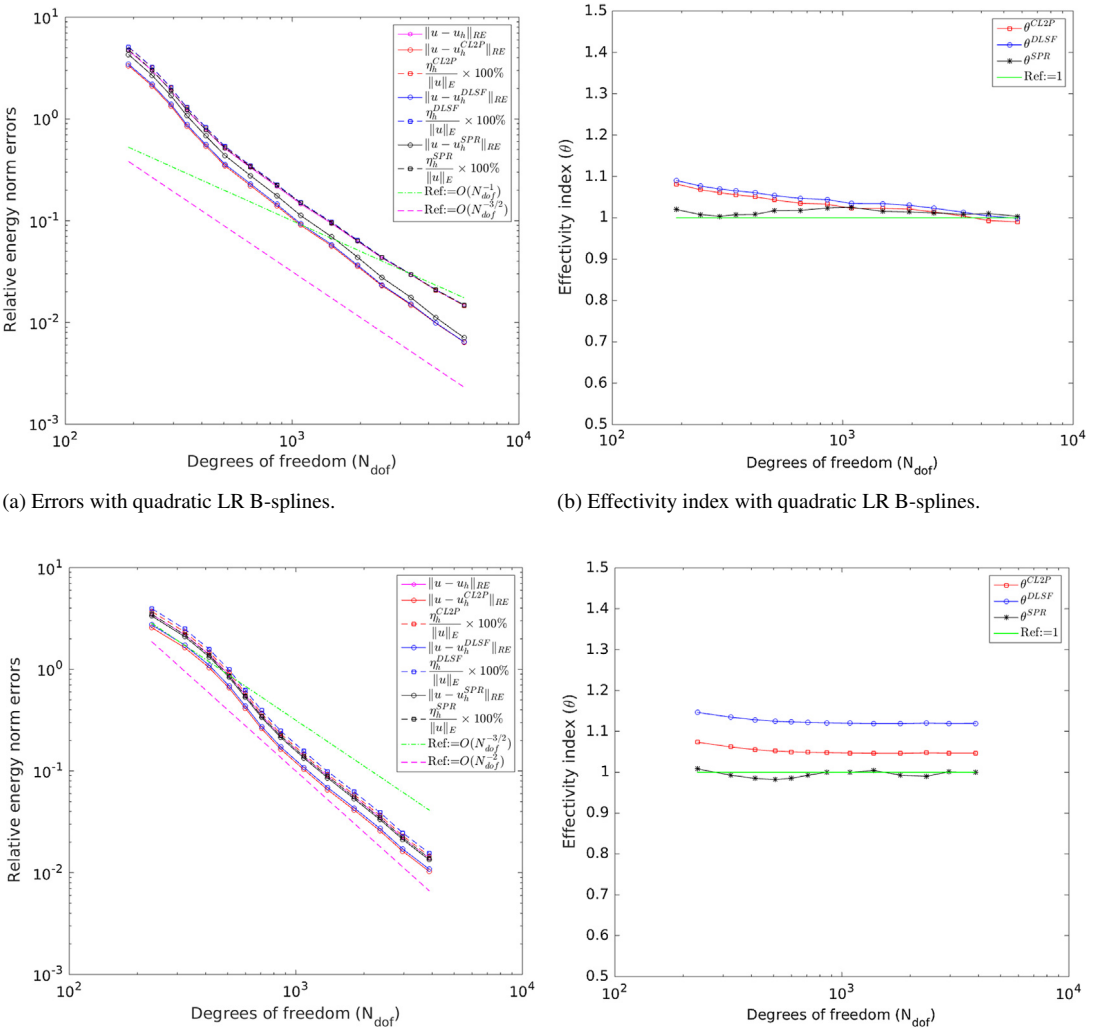

(a) Errors with quadratic LR B-splines.

(b) Effectivity index with quadratic LR B-splines.

(c) Errors with cubic LR B-splines.

(d) Effectivity index with cubic LR B-splines.

Fig. 43. L-shaped domain problem: Error plots and effectivity index for different recovery based a posteriori error estimators in adaptive isogeometric analysis using quadratic and cubic LR B-splines in first and second row, respectively.

the boundary, the proposed adaptive methodology herein is able to identify the proper elements in the neighborhood of the singularity that needs to be refined. Thus, after a certain number of steps the adaptive procedure enables to get the pollution error under control. The use of a uniform (or a nearly uniform) initial mesh and structured mesh refinement based on LR B-splines ensures (for many practical problems) the fulfillment of the mesh restriction, except for a limited number of elements in the vicinity of mesh size changes. Thus, our benchmark examples indicate that we may achieve superconvergent recovered gradients based on the precomputed superconvergent points (PSCP) for the adapted (non-uniform) meshes as well.

In addition to the Superconvergent Patch Recovery (SPR), we have also investigated the use of L^2-Projection (CL2P) and Discrete Least Square Fitting (DLSF). Our main findings are:

- For smooth problems and uniform mesh refinement, the developed recovery procedures DLSF and SPR are superconvergent of order one, whereas the recovered gradient using CL2P shows superconvergence of order close to one, especially for higher degree approximations.
- For the SPR and DLSF procedures, the difference between using PSCP and CSCP is noticeable but not pronounced for the accuracy of the recovered gradient field and the corresponding global effectivity indices for structured meshes refinement obtained by LR-B splines.

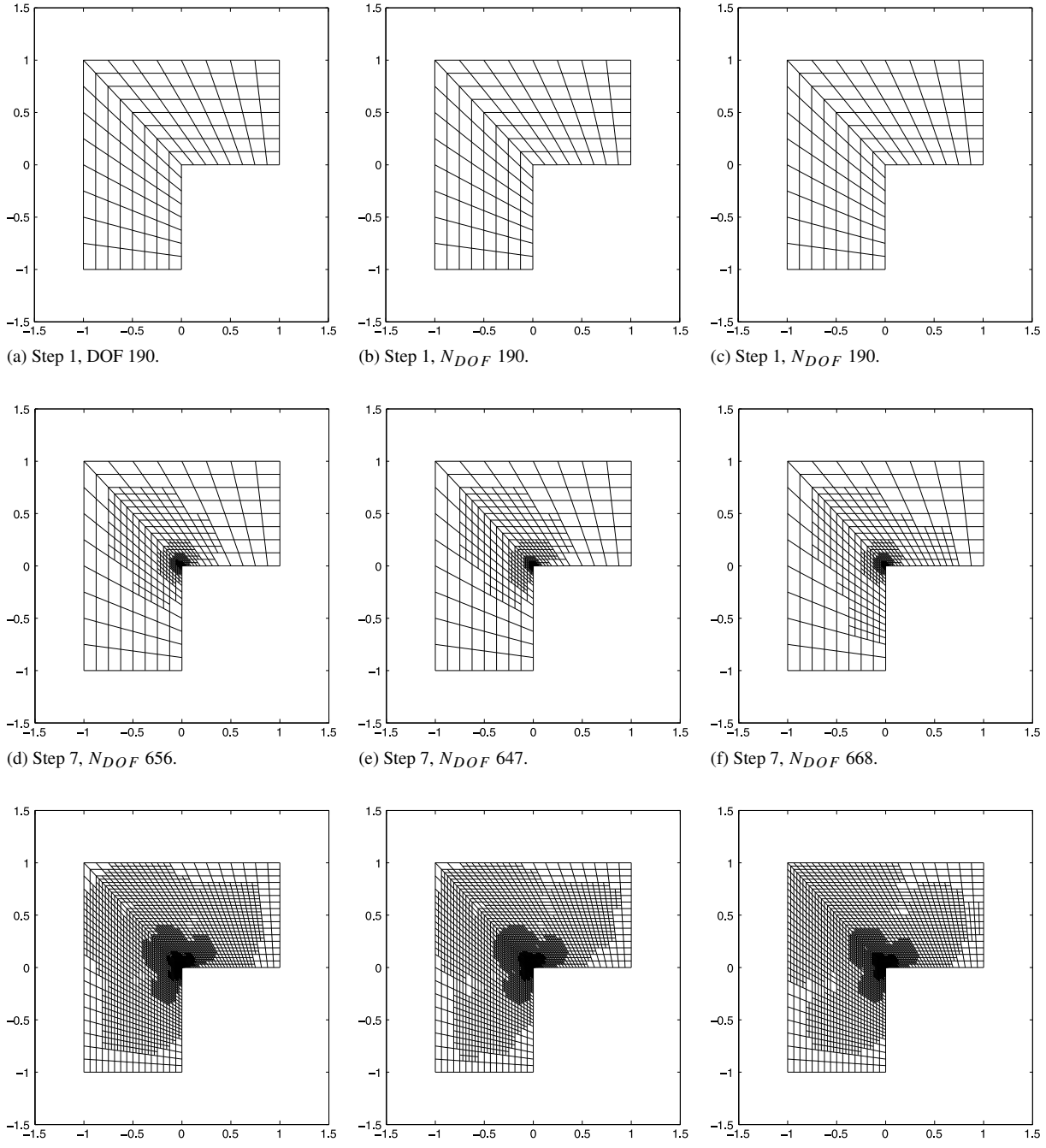

(a) Step 1, DOF 190. (b) Step 1, N_{DOF} 190. (c) Step 1, N_{DOF} 190.

(d) Step 7, N_{DOF} 656. (e) Step 7, N_{DOF} 647. (f) Step 7, N_{DOF} 668.

(g) Step 14, N_{DOF} 4563. (h) Step 14, N_{DOF} 4509. (i) Step 14, N_{DOF} 4357.

Fig. 44. L-shaped domain problem: LR meshes obtained via adaptive LR B-splines refinement algorithm for degree $p = 2$ using different recovery based error estimators at different refinement steps for L-shaped domain problem. The columns from left to right represent the cases with respect to Continuous L^2-projection (CL2P), Discrete least square fitting (DLSF) and Superconvergent patch recovery (SPR), respectively.

- The obtained global effectivity indices for all the three recovery techniques are close to one. This is in contrast to classical residual based error estimates.
- The local elementwise effectivity indices for all the three recovery techniques are also close to one, after some initial refinement steps that is needed to keep any possible pollution effects under control.

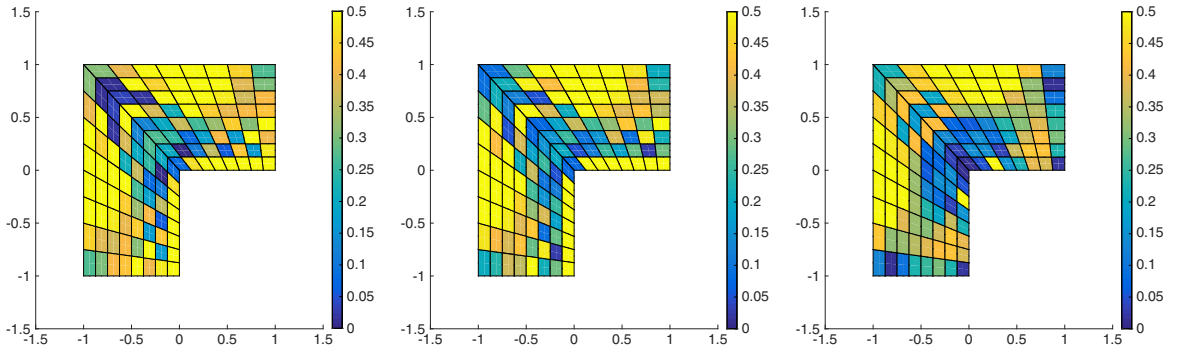

(a) Step 1, N_{DOF} 190. (b) Step 1, N_{DOF} 190. (c) Step 1, N_{DOF} 190.

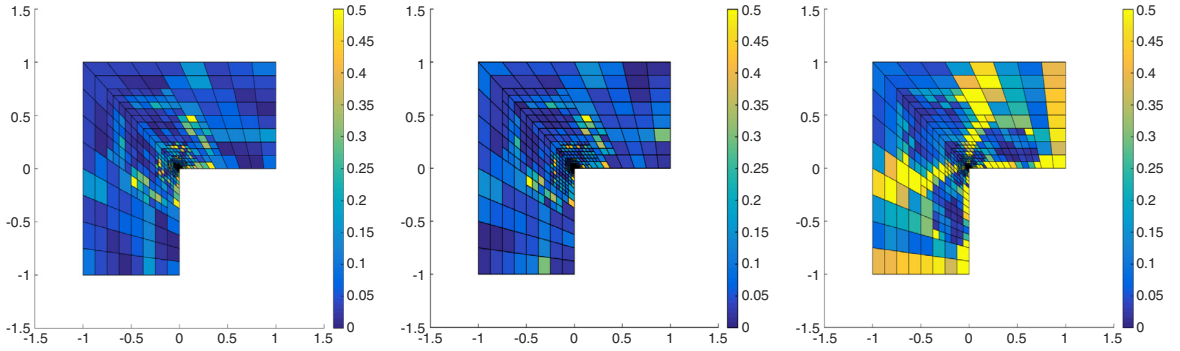

(d) Step 7, N_{DOF} 656. (e) Step 7, N_{DOF} 647. (f) Step 7, N_{DOF} 668.

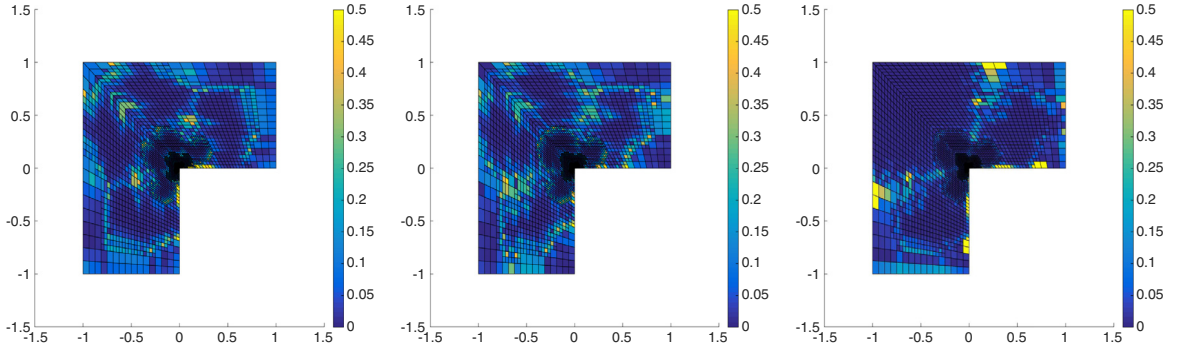

(g) Step 14, N_{DOF} 4563. (h) Step 14, N_{DOF} 4509. (i) Step 14, N_{DOF} 4357.

Fig. 45. L-shaped domain problem: Comparison of absolute value of the deviation effectivity index at element level $|1-\theta^{*}_{el}|$ at LR meshes obtained via adaptive LR B-splines refinement algorithm for degree $p = 2$ using different recovery based error estimators at different refinement steps for L-shaped domain problem. The columns from left to right represent the cases with respect to Continuous L^2-projection (CL2P), Discrete least square fitting (DLSF) and Superconvergent patch recovery (SPR), respectively.

- An important difference between the three recovery methods is that for both CL2P and DLSF we have to solve a global (mass matrix) problem, whereas SPR only involves solution of local problems. This makes SPR favorable in comparison to CL2P and DLSF for realistic (large) industrial problems.

Notice that for randomly adapted meshes (or highly graded meshes) one may not expect recovery of superconvergent gradients using PSCP. However, this may be achieved using CSCP, and we will in an upcoming paper investigate the performance for the recovery techniques proposed herein on highly non-uniform meshes.

The performance of global CL2P and DLSF procedures presented in this article are very encouraging. Thus, it can be worthwhile to develop a local version of these global recovery procedures and some work in this direction have been recently presented in [84,85].

The aim of the present study has been to develop an adaptive methodology that produces global (and local) effectivity indices close to one, i.e., h-asymptotic exact. A natural extension will be to provide guaranteed upper and lower bounds using these recovery techniques and this will be pursued in an upcoming article.

Acknowledgments

The authors gratefully acknowledge the financial support from the Norwegian Research Council and the industrial partners of the ICADA project (RCN grant no: 187993); Ceetron, DNV GL, Statoil, and the FME NOWITECH (RCN grant no: 193823/S60) (www.nowitech.no). The authors also acknowledge the support from Knut Morten Okstad for his help in improving the manuscript.

References

[1] T.J.R. Hughes, J.A. Cottrell, Y. Bazilevs, Isogeometric analysis: CAD, finite elements, NURBS, exact geometry and mesh refinement, Comput. Methods Appl. Mech. Engrg. 194 (39–41) (2005) 4135–4195.
[2] J.A. Cottrell, T.J.R. Hughes, Y. Bazilevs, Isogeometric Analysis. Toward Integration of CAD and FEA, John Wiley & Sons, 2009.
[3] Y. Bazilevs, L. Beirão da Veiga, J.A. Cottrell, T.J.R. Hughes, G. Sangalli, Isogeometric analysis: approximation, stability and error estimates for h-refined meshes, Math. Models Methods Appl. Sci. 16 (7) (2006) 1031–1090.
[4] L. Beirão da Veiga, A. Buffa, J. Rivas, G. Sangalli, Some estimates for h-p-k-refinement in isogeometric analysis, Numer. Math. 118 (2) (2011) 271–305.
[5] L. Beirão da Veiga, D. Cho, G. Sangalli, Anisotropic NURBS approximation in isogeometric analysis, Comput. Methods Appl. Mech. Engrg. 209/212 (2012) 1–11.
[6] L. Beirão da Veiga, A. Buffa, G. Sangalli, R. Vázquez, Mathematical analysis of variational isogeometric methods, Acta Numer. 23 (2014) 157–287.
[7] T. Dokken, T. Lyche, K.F. Pettersen, Polynomial splines over locally refined box-partitions, Comput. Aided Geom. Design 30 (3) (2013) 331–356.
[8] K.A. Johannessen, T. Kvamsdal, T. Dokken, Isogeometric analysis using LR B-splines, Comput. Methods Appl. Mech. Engrg. 269 (2014) 471–514.
[9] M. Kumar, T. Kvamsdal, K.A. Johannessen, A simple a posteriori error estimatior in adaptive isogeometric analysis, Comput. Math. Appl. 70 (7) (2015) 1555–1582.
[10] A. Bressan, Some properties of LR-splines, Comput. Aided Geom. Design 30 (8) (2013) 778–794.
[11] K.A. Johannessen, M. Kumar, T. Kvamsdal, Divergence-conforming discretization for Stokes problem on locally refined meshes using LR B-splines, Comput. Methods Appl. Mech. Engrg. 293 (2015) 38–70.
[12] Y.W. Bekele, T. Kvamsdal, A.M. Kvarving, S. Nordal, Adaptive isogeometric finite element analysis of steady-state groundwater flow, Int. J. Numer. Anal. Methods Geomech. 40(5) (2016) 738–765.
[13] K.A. Johannessen, F. Remonato, T. Kvamsdal, On the similarities and differences between Classical Hierarchical, Truncated Hierarchical and LR B-splines, Comput. Methods Appl. Mech. Engrg. 291 (2015) 64–101.
[14] A. Stahl, T. Kvamsdal, C. Schellewald, Post-processing and visualization techniques for isogeometric analysis results, Comput. Methods Appl. Mech. Engrg. 316 (2017) 880–943.
[15] T.W. Sederberg, J. Zheng, A. Bakenov, A. Nasri, T-splines and t-nurccs, ACM Trans. Graph. 22 (3) (2003) 477–484.
[16] Y. Bazilevs, V.M. Calo, J.A. Cottrell, J.A. Evans, T.J.R. Hughes, S. Lipton, M.A. Scott, T.W. Sederberg, Isogeometric analysis using t-splines, Comput. Methods Appl. Mech. Engrg. 199 (5–8) (2010) 229–263.
[17] M.R. Dörfel, B. Jüttler, B. Simeon, Adaptive isogeometric analysis by local h-refinement with T-splines, Comput. Methods Appl. Mech. Engrg. 199 (5–8) (2010) 264–275.
[18] M.A. Scott, X. Li, T.W. Sederberg, T.J.R. Hughes, Local refinement of analysis-suitable T-splines, Comput. Methods Appl. Mech. Engrg. 213/216 (2012) 206–222.
[19] R. Kraft, Adaptive and Linearly Independent Multilevel B-splines. Bericht. SFB 404, Geschäftsstelle, 1997.
[20] C. Giannelli, B. Jüttler, H. Speleers, Thb-splines: the truncated basis for hierarchical splines, Comput. Aided Geom. Design 29 (7) (2012) 485–498.
[21] A.-V. Vuong, C. Giannelli, B. Jüttler, B. Simeon, A hierarchical approach to adaptive local refinement in isogeometric analysis, Comput. Methods Appl. Mech. Engrg. 200 (49–52) (2011) 3554–3567.
[22] I. Babuška, W.C. Rheinboldt, Error estimates for adaptive finite element computations, SIAM J. Numer. Anal. 15 (4) (1978) 736–754.
[23] I. Babuška, W.C. Rheinboldt, A posteriori error estimates for the finite element method, Internat. J. Numer. Methods Engrg. 12 (1978) 1597–1615.
[24] M. Ainsworth, J.T. Oden, A Posteriori Error Estimation in Finite Element Analysis, John Wiley & Sons, New York, 2000.
[25] P. Ladevèze, D. Leguillon, Error estimate procedure in the finite element method and applications, SIAM J. Numer. Anal. 20 (3) (1983) 485–509.

[26] N. Parés, H. Santos, P. Díez, Guaranteed energy error bounds for the Poisson equation using a flux-free approach: solving the local problems in subdomains, Internat. J. Numer. Methods Engrg. 79 (10) (2009) 1203–1244.
[27] P. Díez, N. Parés, A. Huerta, Recovering lower bounds of the error by postprocessing implicit residual a posteriori error estimates, Internat. J. Numer. Methods Engrg. 56 (10) (2003) 1465–1488.
[28] M. Ainsworth, J.T. Oden, A posteriori error estimation in finite element analysis, Comput. Methods Appl. Mech. Engrg. 142 (1–2) (1997) 1–88.
[29] R. Verfürth, A posteriori error estimation techniques for finite element methods, in: Numerical Mathematics and Scientific Computation, Oxford University Press, Oxford, 2013.
[30] O.C. Zienkiewicz, J.Z. Zhu, A simple error estimator and adaptive procedure for practical engineering analysis, Internat. J. Numer. Methods Engrg. 24 (2) (1987) 337–357.
[31] O.C. Zienkiewicz, J.Z. Zhu, The superconvergent patch recovery and a posteriori error estimates. I. The recovery technique, Internat. J. Numer. Methods Engrg. 33 (7) (1992) 1331–1364.
[32] O.C. Zienkiewicz, J.Z. Zhu, The superconvergent patch recovery and a posteriori error estimates. II. Error estimates and adaptivity, Internat. J. Numer. Methods Engrg. 33 (7) (1992) 1365–1382.
[33] P. Díez, J.J. Ródenas, O.C. Zienkiewicz, Equilibrated patch recovery error estimates: simple and accurate upper bounds of the error, Internat. J. Numer. Methods Engrg. 69 (10) (2007) 2075–2098.
[34] T. Kvamsdal, K.M. Okstad, Error estimation based on superconvergent patch recovery using statically admissible stress fields, Internat. J. Numer. Methods Engrg. 42 (3) (1998) 443–472.
[35] K.M. Okstad, T. Kvamsdal, K.M. Mathisen, Superconvergent patch recovery for plate problems using statically admissible stress resultant fields, Internat. J. Numer. Methods Engrg. 44 (5) (1999) 697–727.
[36] S. Bordas, M. Duflot, Derivative recovery and a posteriori error estimate for extended finite elements, Comput. Methods Appl. Mech. Engrg. 196 (35–36) (2007) 3381–3399.
[37] S. Bordas, M. Duflot, P. Le, A simple error estimator for extended finite elements, Commun. Numer. Methods Eng. 24 (11) (2008) 961–971.
[38] O.A. González-Estrada, S. Natarajan, J.J. Ródenas, H. Nguyen-Xuan, S.P.A. Bordas, Efficient recovery-based error estimation for the smoothed finite element method for smooth and singular linear elasticity, Comput. Mech. 52 (1) (2013) 37–52.
[39] A. Buffa, D. Cho, M. Kumar, Characterization of T-splines with reduced continuity order on T-meshes, Comput. Methods Appl. Mech. Engrg. 201/204 (2012) 112–126.
[40] A. Buffa, C. Giannelli, Adaptive isogeometric methods with hierarchical splines: error estimator and convergence, Math. Models Methods Appl. Sci. 26 (1) (2016) 1–25.
[41] K.A. Johannessen, An Adaptive Isogeometric Finite Element Analysis (Master thesis), Norwegian University of Science and Technology, Norway, 2009.
[42] S.K. Kleiss, S. Tomar, Guaranteed and sharp a posteriori error estimates in isogeometric analysis, Comput. Math. Appl. 70 (3) (2015) 167–190.
[43] M.A. Scott, D.C. Thomas, E.J. Evans, Isogeometric spline forests, Comput. Methods Appl. Mech. Engrg. 269 (2014) 222–264.
[44] L. Tian, F. Chen, Q. Du, Adaptive finite element methods for elliptic equations over hierarchical T-meshes, J. Comput. Appl. Math. 236 (5) (2011) 878–891.
[45] P. Wang, J. Xu, J. Deng, F. Chen, Adaptive isogeometric analysis using rational pht-splines, Comput.-Aided Des. 43 (11) (2011) 1438–1448.
[46] G. Xu, B. Mourrain, R. Duvigneau, A. Galligo, Parameterization of computational domain in isogeometric analysis: methods and comparison, Comput. Methods Appl. Mech. Engrg. 200 (23–24) (2011) 2021–2031.
[47] G. Xu, B. Mourrain, R. Duvigneau, A. Galligo, Optimal analysis-aware parameterization of computational domain in 3D isogeometric analysis, Comput.-Aided Des. 45 (4) (2013) 812–821.
[48] R.E. Bank, R.K. Smith, A posteriori error estimates based on hierarchical bases, SIAM J. Numer. Anal. 30 (4) (1993) 921–935.
[49] S.I. Repin, A posteriori error estimates for approximate solutions to variational problems with strongly convex functionals, J. Math. Sci. (N. Y.) 97 (4) (1999) 4311–4328.
[50] S.I. Repin, A posteriori error estimation for variational problems with uniformly convex functionals, Math. Comp. 69 (230) (2000) 481–500.
[51] I. Babuška, T. Strouboulis, C.S. Upadhyay, A model study of the quality of a posteriori error estimators for linear elliptic problems. Error estimation in the interior of patchwise uniform grids of triangles, Comput. Methods Appl. Mech. Engrg. 114 (3–4) (1994) 307–378.
[52] I. Babuška, T. Strouboulis, C.S. Upadhyay, A model study of the quality of a posteriori error estimators for finite element solutions of linear elliptic problems, with particular reference to the behavior near the boundary, Internat. J. Numer. Methods Engrg. 40 (14) (1997) 2521–2577.
[53] I. Babuška, T. Strouboulis, C.S. Upadhyay, S.K. Gangaraj, K. Copps, Validation of a posteriori error estimators by numerical approach, Internat. J. Numer. Methods Engrg. 37 (7) (1994) 1073–1123.
[54] L.A. Oganesjan, L.A. Ruhovec, An investigation of the rate of convergence of variation-difference schemes for second order elliptic equations in a two-dimensional region with smooth boundary, Zh. Vychisl. Mat. Mat. Fiz. 9 (1969) 1102–1120.
[55] J. Douglas Jr., T. Dupont, Some superconvergence results for Galerkin methods for the approximate solution of two-point boundary problems, in: Topics in Numerical Analysis (Proc. Roy. Irish ACAD. Conf., University Coll., Dublin, 1972), Academic Press, London, 1973, pp. 89–92.
[56] A.B. Andreev, R.D. Lazarov, Superconvergence of the gradient for quadratic triangular finite elements, Numer. Methods Partial Differential Equations 4 (1) (1988) 15–32.
[57] I. Babuška, T. Strouboulis, S.K. Gangaraj, C.S. Upadhyay, η%-superconvergence in the interior of locally refined meshes of quadrilaterals: superconvergence of the gradient in finite element solutions of Laplace's and Poisson's equations, Appl. Numer. Math. 16 (1–2) (1994) 3–49.
[58] I. Babuška, T. Strouboulis, C.S. Upadhyay, S.K. Gangaraj, Computer-based proof of the existence of superconvergence points in the finite element method; superconvergence of the derivatives in finite element solutions of Laplace's, Poisson's, and the elasticity equations, Numer. Methods Partial Differential Equations 12 (3) (1996) 347–392.
[59] J. Douglas Jr., T. Dupont, M.F. Wheeler, An L^∞ estimate and a superconvergence result for a Galerkin method for elliptic equations based on tensor products of piecewise polynomials, Rev. Française Automat. Informat. Recherche Opérationnelle Sér Rouge 8 (R-2) (1974) 61–66.

[60] M. Křížek, Superconvergence phenomena on three-dimensional meshes, Int. J. Numer. Anal. Model. 2 (1) (2005) 43–56.
[61] M. Křížek, P. Neittaanmäki, Bibliography on superconvergence, in: Finite Element Methods (Jyväskylä, 1997), in: Lecture Notes in Pure and Appl. Math., vol. 196, Dekker, New York, 1998, pp. 315–348.
[62] P. Lesaint, M. Zlámal, Superconvergence of the gradient of finite element solutions, RAIRO Anal. Numér. 13 (2) (1979) 139–166.
[63] A.H. Schatz, Pointwise error estimates, superconvergence and extrapolation, in: Finite Element Methods (Jyväskylä, 1997), in: Lecture Notes in Pure and Appl. Math., vol. 196, Dekker, New York, 1998, pp. 237–247.
[64] A.H. Schatz, I.H. Sloan, L.B. Wahlbin, Superconvergence in finite element methods and meshes that are locally symmetric with respect to a point, SIAM J. Numer. Anal. 33 (2) (1996) 505–521.
[65] V. Thomée, High order local approximations to derivatives in the finite element method, Math. Comp. 31 (139) (1977) 652–660.
[66] V. Thomée, Negative norm estimates and superconvergence in Galerkin methods for parabolic problems, Math. Comp. 34 (149) (1980) 93–113.
[67] Z. Zhang, Derivative superconvergent points in finite element solutions of Poisson's equation for the serendipity and intermediate families—a theoretical justification, Math. Comp. 67 (222) (1998) 541–552.
[68] Z. Zhang, Derivative superconvergent points in finite element solutions of harmonic functions—a theoretical justification, Math. Comp. 71 (240) (2002) 1421–1430. (electronic).
[69] I. Babuška, T. Strouboulis, The finite element method and its reliability, in: Numerical Mathematics and Scientific Computation, The Clarendon Press, Oxford University Press, New York, 2001.
[70] C.M. Chen, Structure Theory of Superconvergence of Finite Elements, Hunan Science and Technology Publishing House, Changsha, 2001, (in Chinese).
[71] C.M. Chen, Y.Q. Huang, High Accuracy Theory of Finite Element Methods, Hunan Science and Technology Publishing House, Changsha, 1995 (in Chinese).
[72] L.B. Wahlbin, Superconvergence in Galerkin finite element methods, in: Lecture Notes in Mathematics, vol. 1605, Springer-Verlag, Berlin, 1995.
[73] C.D. Zhu, Q. Lin, The Superconvergence Theory of the Finite Element Method, Hunan Science and Technology Publishing House, Changsha, 1989 (in Chinese).
[74] C. Anitescu, Y. Jia, Y.J. Zhang, T. Rabczuk, An isogeometric collocation method using superconvergent points, Comput. Methods Appl. Mech. Engrg. 284 (2015) 1073–1097.
[75] M. Ainsworth, A. Craig, A posteriori error estimators in the finite element method, Numer. Math. 60 (4) (1992) 429–463.
[76] Y. Bazilevs, L. Beirão da Veiga, J.A. Cottrell, T.J.R. Hughes, G. Sangalli, Isogeometric analysis: approximation, stability and error estimates for h-refined meshes, Math. Models Methods Appl. Sci. 16 (7) (2006) 1031–1090.
[77] I. Babuška, W.C. Rheinboldt, A posteriori error analysis of finite element solutions for one-dimensional problems, SIAM J. Numer. Anal. 18 (3) (1981) 565–589.
[78] J.T. Oden, H.J. Brauchli, On the calculation of consistent stress distributions in finite element approximations, Internat. J. Numer. Methods Engrg. 3 (1971) 317–325.
[79] E. Hinton, J.S. Campbell, Local and global smoothing of discontinuous finite element functions using a least squares method, Internat. J. Numer. Methods Engrg. 8 (1974) 461–480.
[80] T. Blacker, T. Belytschko, Superconvergent patch recovery with equilibrium and conjoint interpolant enhancements, Internat. J. Numer. Methods Eng. 37 (1994) 517–536.
[81] A.H. Schatz, L.B. Wahlbin, Interior maximum-norm estimates for finite element methods. II, Math. Comp. 64 (211) (1995) 907–928.
[82] L.L. Schumaker, Spline Functions: Basic Theory, Cambridge Mathematical Library, Cambridge University Press, Cambridge, 2007.
[83] K.M. Okstad, T. Kvamsdal, Object-oriented programming in field recovery and error estimation, Eng. Comput. 15 (1999) 90–104.
[84] S. Govindjee, J. Strain, T.J. Mitchell, R.L. Taylor, Convergence of an efficient local least-squares fitting method for bases with compact support, Comput. Methods Appl. Mech. Engrg. 213/216 (2012) 84–92.
[85] D.C. Thomas, M.A. Scott, J.A. Evans, K. Tew, E.J. Evans, Bézier projection: a unified approach for local projection and quadrature-free refinement and coarsening of NURBS and T-splines with particular application to isogeometric design and analysis, Comput. Methods Appl. Mech. Engrg. 284 (2015) 55–105.